Heinrich Heine
Universität
Düsseldorf

Dynamics of colloids in external potentials

Inaugural thesis presented to the Faculty of Mathematics and Natural Sciences
of Heinrich Heine University Düsseldorf
for the degree of Doctor of Natural Sciences

by

Yasamin Mohebi Satalsari

from Rasht, IRAN.

Düsseldorf, December, 2025

from the institute for Experimental Softmatter Group
at the Heinrich Heine University Düsseldorf

Published by permission of the
Faculty of Mathematics and Natural Sciences at
Heinrich Heine University Düsseldorf

Examiners:
1. Prof. Dr. Manuel A. Escobedo-Sanchez
2. Prof. Dr. Hartmut Löwen

Date of oral examination: 06.03.2026

Declaration of Originality

I hereby declare that the present thesis is my independent work and has been completed without unauthorized assistance. All sources and references used, including any ideas, text passages, or figures taken from published or unpublished works, have been cited and acknowledged. To my knowledge, this thesis has not been submitted elsewhere, in full or in part, for any academic qualification, unless otherwise stated.

I further confirm that this work complies with the "Principles for the Safeguarding of Good Scientific Practice" of Heinrich Heine University Düsseldorf. I acknowledge that this thesis may be subjected to plagiarism detection software and understand that any violation of academic integrity may result in disciplinary actions, including the revocation of my academic degree.

Düsseldorf,

Yasamin Mohebi Satalsari

Summary

Soft matter systems include materials composed of microscopic components, namely colloids, polymers, gels, foams, and liquid crystals, dispersed in a continuous medium that strongly responds to thermal fluctuations and external fields. Among these systems, colloidal samples have served as an ideal model due to their tunable interactions, optical accessibility, and relevance to both fundamental and applied research. When external energy landscapes are imposed, such as periodic light fields created by interfering laser beams, the motion of colloidal particles becomes highly structured, providing a platform for exploring complex transport phenomena.

In this thesis, we investigate the dynamics of colloidal particles confined to two dimensions and subjected to one-dimensional periodic light fields. By combining trajectory analysis, Brownian dynamics simulations, and analytical models, we systematically characterize particle motion in these confined environments. Furthermore, we examine how geometric factors, specifically the ratio of periodicity to particle diameter, influence the effective potential experienced by the particles.

In the non-equilibrium regime, we investigate the dynamics of colloids driven across the periodic potential by applying an externally imposed driving velocity via stage translation.

The combination of experimental data, simulation results, and theoretical predictions provides a comprehensive framework for understanding colloidal transport in optical potential environments.

Acknowledgements

First and foremost, I would like to express my sincere gratitude to Prof. Dr. Stefan U. Egelhaaf for giving me the opportunity to be part of his research group. Although my time working directly with him was brief, I learned a great deal from his insights, scientific rigor, and guidance.

I am deeply indebted to Prof. Manuel A. Escobedo-Sánchez, who generously supported me throughout my PhD. In Prof. Egelhaaf's absence, he acted as a mentor and advisor, offering invaluable guidance, encouragement, and scientific insight that significantly shaped my progress.

My thanks go as well to Dr. Angel B. Zuccolotto-Bernez, our postdoctoral researcher, for generously sharing his knowledge and for teaching me so much throughout the project.

I would like to thank Prof. Hartmut Löwen and Prof. Jürgen Horbach for their valuable support and insightful feedback during my PhD.

My heartfelt thanks go to Dr. Mahnoosh Madani, who always listened to me with genuine attention and supported me with kindness and friendship throughout this journey.

I am grateful to all the members of our research group, Patrick and Marcell for their assistance, insightful discussions, and the friendly and supportive environment they have provided throughout these years.

I would also like to thank our former group members, Alejandro, Debasish, and Marisa, whose contributions and presence during the earlier stages of my PhD were equally valuable and appreciated.

I am also grateful to Bianka, our group secretary, who was always kind and helpful, supporting me in both academic matters and practical issues beyond the university.

My deepest gratitude goes to my beloved parents. Their unconditional love, support, and countless sacrifices have been the foundation of everything I have achieved. I am also deeply thankful to my dear brother, whose presence and encouragement have meant so much to me throughout this journey.

Lastly, I would like to thank all my friends outside the university. Thank you for being my anchor when things felt overwhelming. Your constant encouragement, patience, and shared frustration meant more than you know. I truly appreciate all the laughter, distractions, and reminders that life exists beyond the lab.

زندگی تر شدن پی در پی است
زندگی آب تنی کردن در حوضچه ی «اکنون» است
گاهی با سختی، گاهی با شادی

Contents

Chapter 1

Introduction

Soft matter plays a significant role across everyday, technological, and biological contexts. Everyday examples include food products such as milk and chocolate, cosmetic creams, and household cleaning agents [1]. In technology, liquid crystals form the foundation of modern display screens [2], while in biology, the principles of soft matter underpin the behaviour of cells, proteins, and membranes [3].

Understanding the broad spectrum of behaviors observed in soft matter requires studying model systems and unraveling their fundamental physical structure and interactions. These systems include colloids, polymers, emulsions, foams, and liquid crystals. They are characterized by length scales ranging from nanometers to micrometers and interaction energies on the order of thermal energy k_BT [4], where k_B is the Boltzmann constant and T is the absolute temperature. As a result, soft matter systems are highly susceptible to thermal fluctuations and external forces, leading to a wide range of equilibrium and non-equilibrium behaviors.

In soft matter physics, colloidal samples are particularly well-suited as model systems. Colloidal particles typically range in size from a few nanometers to several micrometers and can be visualized and tracked using optical microscopy. Their interactions can be finely tuned by modifying the solvent, adjusting the particle surface chemistry, or applying external fields [5]. Furthermore, their Brownian motion provides an experimentally accessible analogue to molecular or atomic systems, enabling direct testing of theoretical models from statistical mechanics [6].

Among experimentally implemented fields, periodic optical potentials have proven to be powerful tools for probing colloidal dynamics in structured environments [7]. These potentials are created by the interference of coherent laser beams, forming well-defined energy landscapes with tunable amplitude and periodicity. Colloids in periodic light fields provide a powerful model system for studying particle interactions and self-organization under controlled and tunable conditions. By using laser beams to create optical potentials, colloidal particles can be trapped, manipulated, and assembled with high precision. This enables system-

atic investigations of fundamental processes such as phase transitions, transport in periodic potentials, and non-equilibrium dynamics. The non-invasive nature and real-time controllability of optical fields make them particularly valuable tools in soft matter physics, microrheology, and the development of reconfigurable materials.

In this thesis, we explore the behaviour of colloidal particles restricted to a two-dimensional plane and subjected to a one-dimensional periodic light field. The periodic light field is generated using a Kösters prism setup [8], which allows for adjustment of the amplitude and periodicity of the periodic light field. We combine particle tracking analysis, Brownian dynamics simulations, and analytical modeling to investigate the interplay between external potentials and particle dynamics. This thesis also builds on results from three research articles, each focusing on distinct aspects of colloidal dynamics: One paper focuses on using the intermediate scattering function to extract dynamic information [9]. In another, we analyzed first-passage and transition-path statistics under external driving based on path-wise observables [10]. The third study examines how particle concentration influences transport in a periodic light field [11]. These publications complement and extend the results presented in the following chapters.

To complement these studies, we calibrate the periodic light field by comparing experimental results with Brownian dynamics simulations, thereby enabling an accurate estimate of the potential amplitude (Sect. 3.8). We then explore the behavior of the driven system, highlighting the impact of external driving velocity on transport through the periodic potential. (Sect. 3.14). Altogether, this thesis presents a comprehensive view of colloidal motion in periodic light fields by bridging theoretical predictions with experimental observations, and it addresses the roles of external light fields, external driving velocity, and crowding in governing particle dynamics.

Chapter 2

Theoretical Background

2.1 Colloidal particles

Colloidal particles are widely used as model systems in soft matter physics due to their intermediate size, which allows for real-time, real-space observation and manipulation [12]. In particular, two-dimensional (2D) systems composed of relatively large colloidal particles, on the order of micrometers, offer a versatile platform for studying collective phenomena, including phase transitions, crystallization, and glassy dynamics[13]. When modeled as hard spheres, these particles interact solely through excluded volume effects, making them an ideal realization of purely entropic systems and enabling direct comparisons with statistical mechanical theories of hard-disk models [14].

A particularly rich area of investigation arises when 2D colloidal systems are exposed to externally imposed optical potentials[15, 16]. These structured fields can be experimentally realized using periodic light fields, which allow for precise control over the symmetry, amplitude, and spatial periodicity of the light field [17]. The interaction between particles and these fields establishes a structured energy potential that modulates their Brownian motion, influencing transport properties, time-dependent diffusivity, and spatial organization under non-equilibrium conditions [18].

The time evolution of particles under 2D confinement and/or external optical potentials can be effectively described by the overdamped Langevin equation, which accounts for the balance between stochastic thermal forces, viscous damping, and any deterministic external forces acting on the particles [19]. Alternatively, the same dynamics can be formulated in terms of the Fokker-Planck equation, which describes the evolution of the probability density function associated with particle positions over time [19]. Together, these frameworks provide a consistent and comprehensive description of both equilibrium and non-equilibrium behavior

in systems influenced by external fields.

Altogether, 2D colloidal systems under periodic optical potentials serve as well-controlled experimental models for investigating the interplay between thermal fluctuations and external fields. In the subsequent chapters, we focus on how these interactions shape the transport dynamics and lead to emergent non-equilibrium behaviors that can be quantitatively compared with theoretical frameworks.

2.2 Colloid–colloid and colloid–potential interactions

The interactions between colloidal particles are often modeled as hard-sphere repulsions. In this idealized representation, colloidal particles are treated as perfectly rigid, impenetrable spheres that experience an infinite repulsive force upon contact but no interaction at larger separations. This simplification captures the essential feature of excluded volume without invoking any long-range forces. The hard sphere interaction potential U_{HS} is defined as

$$U_{\mathrm{HS}}(r) = \begin{cases} \infty, & r \leq \sigma \\ 0, & r > \sigma \end{cases} \tag{2.1}$$

where σ denotes the diameter of a colloidal particle and r is the centre-to-centre distance between a pair of particles. This model enforces a strict no overlap condition and is widely used in theoretical and computational studies to understand the role of packing and entropic effects in dense suspensions. However, in many experimental and simulated systems, especially those involving soft or polymer coated colloids, the abruptness of the hard-sphere potential can present challenges. To address this, the *Weeks–Chandler–Andersen*(WCA) [20] potential is often employed as a more realistic alternative. It retains the key feature of steric repulsion while introducing a smooth and differentiable force profile that decays to zero beyond a finite range. The WCA potential is defined as:

$$U_{\mathrm{WCA}}(r) = \begin{cases} A\varepsilon \left[\left(\frac{\sigma}{r}\right)^{\gamma} - \left(\frac{\sigma}{r}\right)^{\gamma-1} \right] + \varepsilon, & r < \sigma B \\ 0, & r \geq \sigma B \end{cases} \tag{2.2}$$

where

$$A = \gamma \left(\frac{\gamma}{\gamma - 1}\right)^{\gamma-1}, \quad B = \left(\frac{\gamma}{\gamma - 1}\right). \tag{2.3}$$

In this expression, ε is the energy parameter that characterizes the strength of the repulsion between two particles. In this work, we used $\gamma = 50$ to ensure a

sufficiently sharp repulsion that closely resembles the behavior of hard disks and $\varepsilon = 0.6816\, k_B T$ [11].

In addition to inter-particle interactions, colloidal particles can be subjected to an externally imposed energy landscape. A periodic optical potential, generated by the interference of two coherent laser beams, introduces energy barriers that modulate particle dynamics. The result of interfering two coherent laser beams at an angle θ is the formation of a fringe pattern with a spatially modulated intensity profile. This interference pattern creates a periodic distribution of light intensity across space, described by [21, 17]:

$$I(x) = 2I_0 \left\{1 + \cos\left[2kx \sin(\theta/2)\right]\right\} e^{-2x^2 \cos^2(\theta/2)/R^2}, \tag{2.4}$$

where I_0 is the intensity of each beam, $k = 2\pi/L$ is the fringe wave vector, L is the periodicity of the potential, and x is the spatial coordinate perpendicular to the fringes. The cosine term produces the regular fringe structure, while the Gaussian envelope (exponential term) arises from the finite beam radius R and describes the gradual decrease of intensity away from the beam center. In this thesis, the Gaussian envelope varies less than 15% radeally across the field of view and is thus neglected in the analysis.

Building on the intensity distribution described above, the external potential experienced by colloidal particles in experiments involves additional complexities. These arise from factors such as the finite beam radius of the light field, the finite particle size, and the light-scattering properties of the particles, primarily determined by their refractive index contrast with the surrounding medium. In addition, the potential depends on the laser power $\mathrm{L_p}$ and on the wave vector. These factors are crucial for accurately describing the periodic potential experienced by the colloidal particles. The analytical expression used in this work is [17]:

$$U_{\mathrm{ext}}(x) = g\alpha \mathrm{L_p} \left(1 + 3\frac{j_1(ka)}{ka}\cos(kx)\right). \tag{2.5}$$

Here, g is a setup-dependent calibration factor, $\mathrm{L_p}$ is the laser power, $\alpha = \frac{a^3 n_S^2 (n^2-1)}{n^2+2}$ is the particle polarizability, and a is the particle radius. Additionally, the refractive index ratio $n = n_c/n_s$ accounts for the contrast between the colloid n_c and the solvent n_s. The function j_1 is the spherical Bessel function of the first kind (order one), which appears due to the spatial averaging of the cosine potential over the particle's finite size.

Although the actual external potential is more complex, the light field can be reasonably approximated by a spatially periodic optical potential, described as:

$$U_{\mathrm{ext}}(x) = V_0 \cos(kx) + V_{bg}, \tag{2.6}$$

where V_0 is the potential amplitude and $V_{bg} = g\alpha \mathrm{L_p}$ is a constant offset. Since V_{bg} is position independent, it does not enter the external force experienced by the particles. The amplitude V_0 can be expressed as [7, 18]

$$V_0 = 3g\alpha \mathrm{L_p} \frac{j_1(ka)}{ka}. \tag{2.7}$$

Here, we can clearly see the influence of the particle size and the periodicity of the optical field, expressed by the wave vector $k = 2\pi/L$, on the amplitude.

2.3 Colloidal particles dynamics

2.3.1 Brownian motion

The study of particle motion in colloidal systems originated with the experimental observations of Robert Brown in 1828, who reported the random movement of pollen grains suspended in water under a microscope [22]. Albert Einstein provided the theoretical explanation in 1905, deriving a quantitative relation between the mean squared displacement (MSD) and the diffusion coefficient, thereby linking Brownian motion to thermal fluctuations [23]. The first experimental calculation of MSD was carried out by Jean Perrin, who recorded colloidal particle trajectories and provided direct experimental confirmation of Einstein's theoretical predictions [24].

Shortly thereafter, Langevin (1908)[25] and Smoluchowski (1916)[26] developed complementary methodologies to characterize the motion of colloidal particles. We will discuss the Brownian motion framework and the Langevin approach in detail, covering the background, mathematics, and physical consequences.

To characterize the motion of colloidal particles, various observables are computed from experimentally obtained particle trajectories, typically acquired via video microscopy and analyzed using particle tracking algorithms. These observables are broadly categorized into two types: those analyzed directly in sample space, based on particle displacements, and those analyzed in reciprocal space using Fourier-based correlation functions, as commonly applied in scattering experiments. Each approach provides complementary insights into how thermal fluctuations impact particle dynamics. The following presents a description of the system's dynamics in sample space.

The displacement of a particle over a delay time τ is defined relative to a starting time t_0 as:

$$\Delta x(\tau; t_0) = x(t_0 + \tau) - x(t_0), \tag{2.8}$$

where $x(t)$ is the particle position at time t. This displacement arises from random collisions between solvent molecules and the particle, leading to a Brownian trajectory. The probability density function $P(x, \tau)$, which describes the probability

of finding a particle at a position x at a delay time τ, is governed by the diffusion equation[27]:

$$\frac{\partial P(x,\tau)}{\partial \tau} = D\frac{\partial^2 P(x,\tau)}{\partial x^2}, \tag{2.9}$$

where D is the diffusion coefficient. For a particle starting at $x = 0$, the solution to this equation is a Gaussian distribution:

$$P(x,\tau) = \frac{1}{\sqrt{4\pi D\tau}} \exp\left(-\frac{x^2}{4D\tau}\right). \tag{2.10}$$

This solution shows that the distribution of particle positions spreads over time. The width of the distribution is characterized by MSD, which reflects how far particles move, on average, over time. The MSD is a key measure of Brownian motion, quantifying the average distance a particle moves over a delay time. It is defined as

$$\langle \Delta x^2(\tau) \rangle = \langle [x(t_0 + \tau) - x(t_0)]^2 \rangle. \tag{2.11}$$

Einstein's analysis of Brownian motion for dilute systems, demonstrated that the MSD is directly proportional to time and the diffusion coefficient [28]:

$$\langle \Delta x^2(\tau) \rangle = 2dD\tau. \tag{2.12}$$

where d is the number of spatial dimensions (e.g., $d = 2$ for 2D motion) and D is the diffusion coefficient. This linear relationship is a fundamental feature of diffusive processes, setting Brownian motion apart from other types of motion. For instance, in ballistic motion, MSD scales as τ^2, corresponding to motion with a constant velocity, whereas in Brownian motion, the MSD increases linearly with time as a result of random thermal fluctuations.

2.3.2 Colloids in two-dimensional geometries

Colloidal particles in 2D geometries, where motion is effectively restricted to a plane, exhibit diffusion dynamics that differ substantially from those in three-dimensional systems. Such systems are common in experiments where particles move in thin fluid layers or between closely spaced surfaces, conditions that enhance hydrodynamic interactions with nearby boundaries. These effects often play a dominant role in determining the effective diffusion coefficient. In the absence of boundaries, the diffusion of a spherical particle in a viscous fluid, here called the bulk diffusion coefficient D_b, is well described by the Stokes–Einstein–Sutherland relation [23, 29, 30]:

$$D_b = \frac{k_B T}{\xi} = \frac{k_B T}{6\pi\eta a}, \tag{2.13}$$

where k_B is the Boltzmann constant, T the absolute temperature, η the dynamic viscosity of the fluid, and a the particle radius. The term $6\pi\eta a$ corresponds to the Stokes friction coefficient, ξ. D_b assumes that the particle is in an unbounded medium. However, in experimental systems, especially in two-dimensional geometries such as particles confined between two glass surfaces (Fig. 2.1), hydrodynamic interactions with the nearby walls significantly reduce the particle's mobility. As a result, the measured diffusion coefficient is reduced compared to D_b [31, 32, 33].

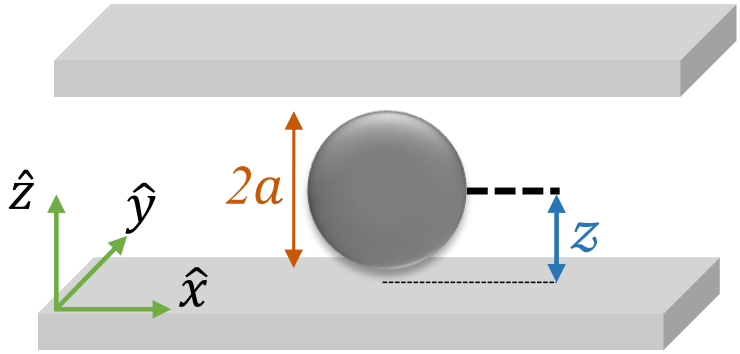

Figure 2.1: Schematic of a colloidal particle of diameter $2a$ restricted between two parallel walls, with its vertical position close to the bottom wall ($z \approx a$). The motion is restricted to the xy-plane and influenced by near-wall hydrodynamic effects.

To characterize how particle dynamics evolve over time, the time-dependent diffusivity is introduced as:

$$D(\tau) = \frac{1}{2}\frac{d}{d\tau}\langle \Delta x^2(\tau)\rangle. \tag{2.14}$$

In a dilute 2D system without external forces, referred to as free diffusion, $D(\tau)$ remains constant for all delay times. In contrast, in systems under external forces, it varies with time, indicating different dynamical regimes.

The anomalous diffusion exponent, $\mu(\tau)$, characterizes the scaling of the MSD with time and is defined as [34]:

$$\mu(\tau) = \frac{d\log\langle \Delta x^2(\tau)\rangle}{d\log\tau}. \tag{2.15}$$

This quantity provides insight into the temporal evolution of MSD ($\langle \Delta x^2(\tau)\rangle \sim \tau^{\mu}$) and enables the distinction between different transport regimes. Normal diffusion corresponds to $\mu(\tau) = 1$, subdiffusion to $\mu(\tau) < 1$, and superdiffusion to $\mu(\tau) > 1$.

While MSD provides a basic measure of diffusion, it does not capture deviations from Gaussian behavior. A more detailed characterization comes from the fourth moment, from which the Non-Gaussian Parameter (NGP) is defined as[35]:

$$\alpha_2(\tau) = \frac{\langle [\Delta x(\tau)]^4 \rangle}{3\langle [\Delta x(\tau)]^2 \rangle} - 1. \tag{2.16}$$

For purely Gaussian diffusion, this parameter is zero, whereas positive values indicate anomalous diffusion.

These observables (MSD, $D(\tau)$, $\mu(\tau)$, and NGP) provide a consistent framework for describing the dynamics of particles, allowing us to link statistical measures of motion to the underlying physical processes and identify different transport regimes.

2.3.3 Langevin equation

We now extend our description to the case of colloidal particles in two dimensions subjected to an external field. The Langevin equation describes the trajectories of individual particles under the combined influence of random thermal forces and deterministic forces arising from external potentials [25]. In such a picture, the motion of a particle with a mass m, according to Newton's second law, is determined[19],

$$m\ddot{x}(\tau) = -\xi\dot{x}(\tau) - \frac{d}{dx}U_{\text{ext}}(x) + F_{\text{rand}}(\tau), \tag{2.17}$$

where the left-hand side represents the inertial term. ξ is the Stokes friction coefficient, $\frac{d}{dx}U_{\text{ext}}(x)$ represents the force due to an external potential. These forces can arise due to gravity, optical trapping, electric or magnetic fields, fluid flow, or interactions between particles. $F_{\text{rand}}(\tau)$ denotes the stochastic force exerted by the surrounding fluid molecules on the particle. According to the fluctuation–dissipation theorem, the statistical properties of $F_{\text{rand}}(\tau)$ are:

$$\langle F_{\text{rand}} \rangle = 0, \quad \langle F_{\text{rand}}(\tau) F_{\text{rand}}(\tau') \rangle = 2k_B T \xi \delta(\tau - \tau'), \tag{2.18}$$

where $\delta(\tau - \tau')$ is the Dirac delta function ensuring the independence of fluctuations at different delay times.

In experimental systems, colloidal particles are often subjected to external forces, which significantly modify their dynamics. In the presence of an external force, the motion of a Brownian particle is a combination of stochastic fluctuations and the effect of that force. The transition from inertial to overdamped motion is characterized by the ballistic time $\tau_{\text{ballistic}} = m/\xi$. For $\tau \gg m/\xi$, the inertial term $m\ddot{x}(\tau)$ in Eq.(2.17) becomes negligible, and viscous and stochastic forces dominate

the motion. In this regime, the Langevin equation simplifies to what is known as the overdamped Langevin equation[19]:

$$\dot{x}(\tau) = -\frac{1}{\xi}\frac{d}{dx}U_{\text{ext}}(x) + \frac{1}{\xi}F_{\text{rand}}(\tau). \tag{2.19}$$

In the absence of an external potential, but in the presence of constant velocity v_{driven}, the overdamped Langevin equation takes the form

$$\dot{x}(\tau) = v_{\text{driven}} + \frac{1}{\xi}F_{\text{rand}}(\tau). \tag{2.20}$$

that gives rise to a systematic displacement of the particles in the direction of v_{driven}. As a result, this driven motion adds a deterministic term to the MSD alongside the stochastic Brownian contribution:

$$\langle \Delta x^2(\tau) \rangle = 2D\tau + v_{\text{driven}}^2\tau^2. \tag{2.21}$$

Where D is the free diffusion coefficient. At short delay times, the motion is dominated by thermal fluctuations, and MSD follows the typical diffusive relation in Eq. 2.12 As the delay time increases, the deterministic contribution from the driven motion becomes dominant, and the motion gradually shifts from random diffusion to directed motion. In this regime, the MSD exhibits ballistic-like behavior.

$$\langle \Delta x^2(\tau) \rangle \approx v_{\text{driven}}^2\tau^2. \tag{2.22}$$

We now consider the case where colloidal particles are subjected to an external periodic potential. Such potentials can be generated, for instance, by optical lattices or standing-wave light fields, where interference between laser beams creates a periodic optical potential. To describe the motion of a Brownian particle in a periodic potential, we use the Langevin equation (Eq. 2.19), where the external potential takes the form $U_{\text{ext}}(x)$

$$U_{\text{ext}}(x) = V_0\cos(kx) + V_{bg}, \tag{2.23}$$

where V_0 is the potential amplitude, k is the wave vector, and is related to the periodicity of the potential $L = 2\pi/k$. The constant term $V_{bg} = g\alpha L_p$ represents an offset in the potential. The corresponding external force is:

$$F_{\text{ext}}(x) = -\frac{d}{dx}U_{\text{ext}}(x) = kV_0\sin(kx). \tag{2.24}$$

Substituting this external force into the overdamped Langevin (Eq.2.19) equation yields:

$$\dot{x}(\tau) = -\frac{kV_0}{\xi}\sin(kx) + \frac{1}{\xi}F_{\text{rand}}(\tau). \tag{2.25}$$

At this point, we have introduced the influence of external forces on Brownian motion. To further comprehend these dynamics, solving the Langevin equation is essential, utilizing both analytical and numerical approaches. In section 3.8, we focus on solving the Langevin equation for both a constant driving velocity and a periodic potential, and explore how these forces modify particle trajectories. Furthermore, we will address the experimental realization of the periodic potential, focusing on its implementation with an optical laser field. This will provide further insight into how external forces influence colloidal motion.

2.3.4 Langevin equation in reduced units

The Langevin equation can be reformulated in reduced units to simplify its mathematical treatment and enhance computational efficiency. Expressing the equation in reduced units form eliminates redundant physical constants and reduces the number of independent parameters, yielding a more universal representation of the system's behavior. We consider the particle diameter σ as the unit of length and define the dimensionless coordinate [36, 37]:

$$x^*(\tau) = \frac{x(\tau)}{\sigma}, \tag{2.26}$$

where (*) denotes the quantities expressed in reduced units. For Brownian motion, the MSD in reduced units can be expressed as

$$\langle \Delta x^{*2}(\tau) \rangle = \left\langle \left[\frac{x(t_0+\tau)}{\sigma} - \frac{x(t_0)}{\sigma} \right]^2 \right\rangle = \frac{1}{\sigma^2} \langle \Delta x^2(\tau) \rangle = 2\frac{D}{\sigma^2}\tau. \tag{2.27}$$

From which a characteristic diffusion time, referred to as the Brownian time (τ_B), is defined as:

$$\tau_B = \frac{\sigma^2}{D}. \tag{2.28}$$

The reduced time scale is defined in terms of the delay time as:

$$\tau^* = \frac{\tau}{\tau_B} = \frac{D\tau}{\sigma^2}. \tag{2.29}$$

By substituting the reduced variables x^*, τ^* in the overdamped Langevin equation, Eq.2.19, and using the relation $\xi = k_B T/D$ we get:

$$\frac{dx^*}{d\tau^*} = \frac{V_0}{k_B T}\sigma k \sin(k\sigma x^*) + F^*_{\text{rand}}(\tau^*). \tag{2.30}$$

The wave vector and potential amplitude can be expressed in reduced units as

$$k^* = k\sigma, \quad V_0^* = V_0/k_B T. \tag{2.31}$$

The dimensionless random force is defined as

$$F^*_{\text{rand}}(\tau^*) = \frac{\sigma}{k_B T} F_{\text{rand}}(\tau), \tag{2.32}$$

and satisfies the requirements

$$\langle F^*_{\text{rand}}(\tau^*) F^*_{\text{rand}}(\tau^{*'}) \rangle = 2\,\delta(\tau^* - \tau^{*'}). \tag{2.33}$$

Hence, the full overdamped Langevin equation in reduced units is

$$\frac{dx^*}{d\tau^*} = V_0^* k^* \sin(k^* x^*) + F^*_{\text{rand}}(\tau^*). \tag{2.34}$$

This reduced formulation of the overdamped Langevin equation emphasizes the key dimensionless parameters that govern the particle dynamics in a periodic potential, the reduced potential amplitude V_0^* and the reduced wave vector k^*. By eliminating explicit dependencies on system-specific quantities such as particle size, temperature, or viscosity, the rescaled equation provides a universal framework that is well-suited for analytical studies and numerical simulations.

2.3.5 Fokker-Planck Equation

The Fokker-Planck equation is a fundamental partial differential equation that describes the time evolution of the probability density function, $p(x, \tau)$, of the position or momentum of a colloidal particle under the influence of external forces [38, 19]. It is a continuity equation for the probability density, ensuring the conservation of probability. In the context of colloidal systems, it provides a robust framework for understanding the collective behavior and spatial distribution of particles [38, 19], while the overdamped Langevin equation (Sec. 2.3.3) describes the trajectories of individual particles influenced by random forces and external potentials. The Fokker–Planck equation is particularly useful for systems in the overdamped limit, where inertial effects are negligible, and it is equivalent to the Langevin description for equilibrium dynamics[38].

For a single Brownian particle at position x, subject to a potential $U_{\text{ext}}(x)$, and evaluated at delay time τ, the Fokker-Planck equation is given by[38]:

$$\partial_\tau p(x, \tau) = -\partial_x \left\{ \left[-D/k_B T \frac{dU_{\text{ext}}(x)}{dx} - D\partial_x \right] p(x, \tau) \right\}, \tag{2.35}$$

here, the terms have the following physical significance: $p(x, \tau)$ represents the probability density function of the particle's position at delay time τ. D is the free diffusion coefficient, directly related to temperature and viscosity by the Stokes-Einstein equation (Eq. 2.13). When the diffusivity is constant and the system

is considered stationary, the Fokker–Planck equation is also referred to as the Smoluchowski equation [38, 39]. $dU_{\text{ext}}(x)/dx$ is the force derived from the external potential $U_{\text{ext}}(x)$. Eq. 2.35 is a continuity equation for the probability density, ensuring the conservation of probability. The term $-D/k_BT\frac{dU_{\text{ext}}(x)}{dx}p(x,\tau)$ represents the drift current, which arises from the force exerted by the external potential on the particles. The second term, $-D\partial_x p(x,\tau)$, represents the diffusive current, driven by random thermal fluctuations. $\frac{dU_{\text{ext}}(x)}{dx}$ is the force derived from the external potential $U(x)$.

The Fokker-Planck equation is central to understanding how external potentials and thermal noise collectively shape the spatial distribution and dynamics of colloidal particles. By solving this equation, one can obtain the full statistical description of particle motion, including the steady-state probability distributions in both equilibrium and non-equilibrium steady-states. In this thesis, this equation serves as a theoretical basis for analyzing particle dynamics in periodic light fields. It complements the single-particle trajectories generated through numerical integration of the Langevin equation, offering a comprehensive picture of the system's behavior.

2.3.6 Reciprocal space

In addition to analyzing particle motion in sample space, an alternative and complementary approach is to study the system's dynamics in reciprocal space. These space observables provide insight into spatial correlations and density fluctuations by employing Fourier transforms of sample space quantities. A key quantity in reciprocal space analysis is the self-intermediate scattering function (self-ISF), which describes the time-dependent decay of density fluctuations at a given wave vector q. It is defined as

$$f(q,\tau) = \left\langle e^{iq\cdot(r(\tau)-r(0))} \right\rangle . \tag{2.36}$$

It is a key observable in the study of colloidal and soft matter systems, providing a direct measure of a single particle's motion in reciprocal space. In systems with a spatially periodic potential, the Self-ISF remains useful but does not fully capture the rich spatial structure and mode coupling induced by the periodic landscape. It is advantageous to consider a generalized ISF, which incorporates correlations between different reciprocal lattice modes. It is defined as

$$F_{\mu\nu}(q,\tau) = \left\langle e^{-i(q+Q_\mu)x(\tau)}\, e^{i(q+Q_\nu)x(0)} \right\rangle , \tag{2.37}$$

where q is a wave vector in the first Brillouin zone, and $Q_\mu = 2\pi\mu/L$ (and analogously Q_ν) are the reciprocal lattice vectors, with the mode indices $\mu, \nu \in \mathbb{Z}$. This generalized formulation extends self-ISF by resolving off-diagonal correlations in

reciprocal space ($F_{\mu\neq\nu}$). These off-diagonal components contain critical information about the interference between different periodic modes and are particularly sensitive to the structure of the potential and the particle's localization behavior. To gain further insight into the behavior of $F_{\mu\nu}(q,\tau)$, it is useful to consider its limiting cases at short and long times. For a periodic potential system, Eq. 2.37 in the short time limit reduces to [9]:

$$F_{\mu\nu}(q,\tau=0) = \langle \exp(-iQ_{\mu-\nu}x(0))\rangle \tag{2.38}$$

$$= (-1)^{\mu-\nu}\frac{I_{\mu-\nu}(V_0/k_BT)}{I_0(V_0/k_BT)}, \tag{2.39}$$

and in the long time limit for $q = 0$

$$F_{\mu\nu}(0,\tau\to\infty) = \frac{(-1)^{\nu+\mu}\mathrm{I}_\mu(V_0/k_BT)\mathrm{I}_\nu(V_0/k_BT)}{\mathrm{I}_0^2(V_0/k_BT)}, \tag{2.40}$$

where I_μ, I_ν represents the modified Bessel function of the first kind. In our analysis, we use both the short- and long-time limits of the generalized ISF to characterize key properties of the external potential. The long-time limit of the generalized ISF allows us to determine the amplitude of the periodic potential by comparing the asymptotic values with theoretical predictions, See [9] for further details. In contrast, the short-time limit reflects the spatial structure of the equilibrium distribution and is sensitive to the periodicity of the potential.

Chapter 3

Overview

3.1 Experimental system

This section first describes the preparation of the colloidal samples used in the experiments, including particle selection, concentration adjustment, and solvent conditions to ensure long term stability. Special consideration is given to selecting materials for the cell walls, spacers, and sealing of the sample cell, as well as defining the assembly procedures, since these factors play a crucial role in ensuring sample stability and experimental reproducibility. The system is then dynamically characterized in the absence of an external periodic optical potential by measuring its time-dependent diffusion.

3.1.1 Colloidal sample

For this study, polystyrene sulfate latex particles with diameters of 3 μm ($\sim$ 5% polydispersity, Invitrogen, Batch. No.1838504), 4 μm ($\sim$ 4% polydispersity, Batch. Molecular Probes, Batch. No.1259392), and 5 μm ($\sim$ 6% polydispersity, Invitrogen, Batch. No.853189) were dispersed in ultrapure water with a resistivity of 18.2 MΩcm (Purelabs Flex system, Elga).

Depending on the particle size under study, spacers with diameters of 4 μm, 5 μm, or 6 μm were employed, corresponding to particle sizes of 3 μm, 4 μm, and 5 μm, respectively. The spacers defined a well-controlled gap between the coverslips, creating a 2D geometry in which the particles could move freely in the plane while being confined vertically. This configuration maintained a stable spacing between the coverslips, preventing capillary forces from narrowing the gap and compressing the particles.

3.1.2 Colloidal sample cell

The sample cell was assembled on a microscope slide using a rectangular coverslip (24×50 mm, thickness No.1, VWR, product no. 631-0146) and a smaller square coverslip (22×22 mm, thickness No.1.5, VWR, product no. 631-0125). This configuration was chosen to ensure that both walls in contact with the colloidal sample were made of the same borosilicate glass, thereby reducing particle adhesion to the surfaces.

Before assembly, the cover slips were thoroughly cleaned using a 2% Hellmanex solution in ultrapure water and sonicated for 30 minutes. They were then rinsed and sonicated three times with ultrapure water to ensure complete removal of residual surfactants, with each step lasting 15 minutes. After rinsing, the coverslips were placed in an oven at 85 °C for 2 hours to promote quick and uniform drying.

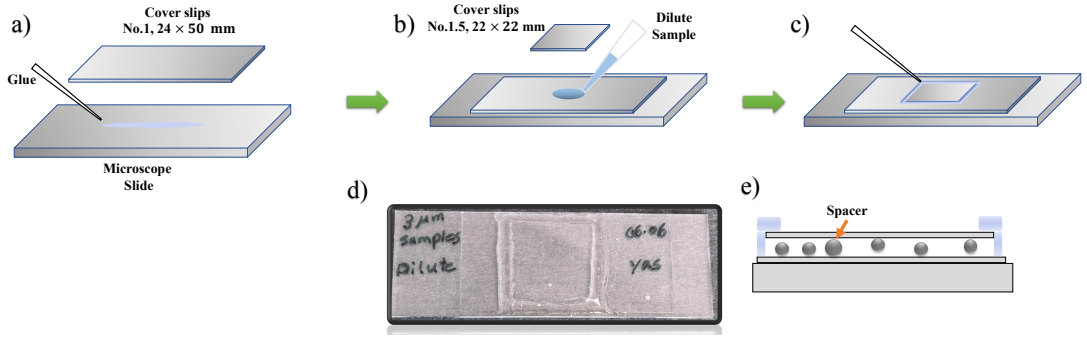

Figure 3.1: Step-by-step assembly of the sample cell used for 2D samples. a) A rectangular coverslip (No. 1) is attached to a microscope slide using Norland Optical Adhesive 61. b) A small droplet of the colloidal sample is deposited at the center using a pipette. A square coverslip is placed on top to enclose the sample. c) The edges are sealed with UV-curable adhesive. d) A photograph of the assembled sample cell, showing the sealed region containing the dilute sample. e) Schematic illustration of the cell interior.

After cleaning and drying, the sample cell assembly was performed. The rectangular coverslip was glued to a microscope slide using a UV-curing adhesive (NOA61, Norland Products) and then cured under a UV lamp for 1 minute to form the base of the sample cell (Fig.3.1a). After curing, 2.5μL of the colloidal sample was carefully placed at the center of the coverslip (Fig.3.1b). The smaller square coverslip was then placed on top, gently pressed to bring the two coverslips closer together, ensuring that the spacing corresponded to the height of the spacers without compressing the particles. This allowed the liquid to spread evenly and remain free of air bubbles (Fig.3.1b). The edges of the assembled cell were then sealed with a UV-curing adhesive cured under a UV lamp in three cycles of

3 minutes each. Between curing cycles, the adhesive layer was carefully checked to ensure the proper sealing of the cell, (Fig.3.1c). The final sample cell, with the glued region and enclosed volume, is shown in Fig.3.1d. Each cell was labeled with the particle size, dilution conditions, and preparation date for reference. A schematic representation of the sample cell interior is shown in Fig. 3.1e, where the colloidal particles are randomly distributed within the sample, and the gap between the two coverslips is determined by the size of the spacer particles. After assembly, the sample cell was left in the laboratory for 48 hours to equilibrate, allowing the solvent and particles to relax and establish a stable configuration with a uniform distribution and steady Brownian motion, free of aggregation or thermal drift. Following equilibration, the sample cell was mounted on the microscope, and regions with a uniform particle distribution were selected for measurements. All observations were carried out in regions where the particle area fraction was approximately 0.01, ensuring dilute conditions.

3.1.3 Sample characterization

Despite our efforts to prepare all samples under comparable restriction conditions, measurable variations were observed in time-dependent diffusivities $D(\tau)$, as shown in Fig. 3.2a. The short-time regime of $D(\tau)$ was used to extract the diffusion coefficients, whose distribution is displayed in Fig. 3.2b. The observed variation is primarily due to the manual assembly of the cells, where small differences in how much the upper coverslip was pressed down resulted in variations in sample height and, consequently, in particle mobility. The distribution shown in Fig. 3.2b reveals a coefficient of variation of approximately 12%, underscoring how variations in sample geometry can affect diffusivity.

Additionally, we observed that each sample gradually ages after approximately 10 days, as particles begin to stick to the walls. Since our analysis focuses on the dilute regime, reliable statistics can only be obtained when particle motion remains stable and consistent throughout the series of measurements. Therefore, to ensure data quality and reproducibility, we periodically replaced the samples during the series of measurements.

3.2 Experimental setup

This section describes the experimental setup used to create the periodic light field for studying the dynamics of colloidal particles in the periodic potential. The setup enables precise control over the fringe spacing and intensity of the periodic light field at the sample plane.

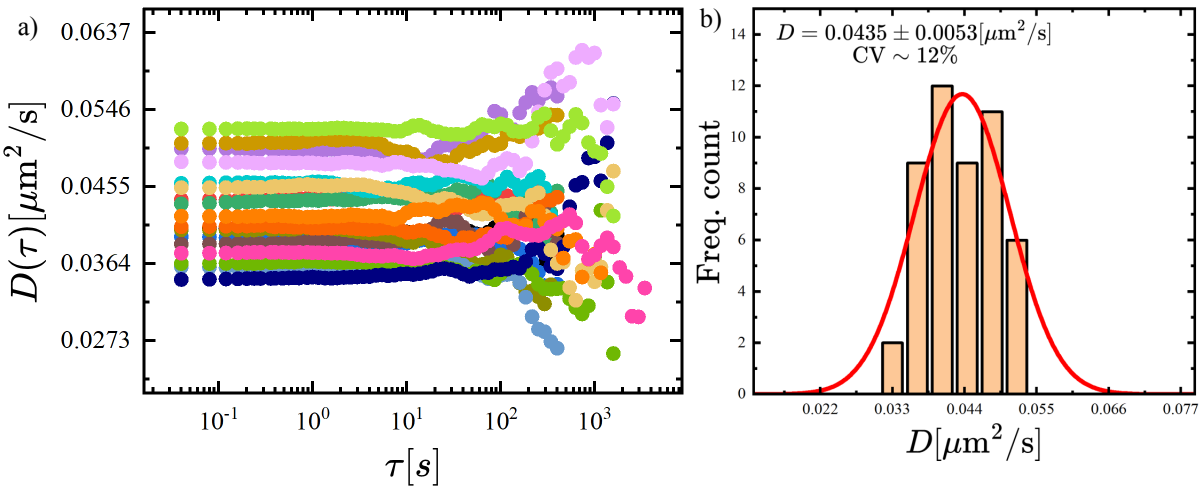

Figure 3.2: Time-dependent diffusivity $D(\tau)$ obtained from multiple 2D experimental samples using particles with 3 μm diameter and spacers of 4 μm diameter. Each dataset corresponds to a different sample prepared under similar confinement conditions. b) Distribution of the diffusion coefficients D extracted from these samples. The fitted Gaussian yields a mean value of $D = 0.0435 \pm 0.0053\,\mu m^2/s$ with a coefficient of variation of 12%. The observed spread primarily reflects the handmade nature of the samples, leading to small variations in the spacing between the confining coverslips.

The experimental setup combines a periodic light field generator and an imaging system (Microscope) as shown in Fig.3.3a. A 532 nm wavelength laser (Cobolt 05-01 Samba, 1.5 W) is expanded using two lenses (L1 and L2) acting as a beam expander. The expanded beam is then directed using two mirrors (M1 and M2) toward a Kösters prism (KP). In the KP prism, the beam is split into two parallel beams of equal intensity. These beams are then focused by lens L3 and reflected by a dichroic mirror (D1) onto the sample plane, where they interfere to generate a one-dimensional periodic light field. The periodicity of the light field is tuned by adjusting the KP prism, and its amplitude is controlled by varying the laser power.

The imaging system is based on an inverted Nikon Ti-E microscope equipped with a 20× objective (NA = 0.5, Nikon Plan Flour). Uniform illumination is provided by a blue LED (Thorlabs M455L4), and the particle motion is recorded with a CMOS camera (Mako U-130B), a sensor of 1280×1024 pixels, each pixel having a size of 4.8 μm. This corresponds to a pixel pitch of 0.24 μm/px. To eliminate any laser light contamination reaching the camera, a dichroic mirror (D2) directs the

transmited laser light into a beam dump (BD), and a notch filter (NF) provided additional suppression before the light reached the detector. This configuration allowed for high-precision measurements under well-controlled optical confinement. The resulting interference pattern with periodicity L and the corresponding cosine potential experienced by the particles are illustrated in Fig.3.3b.

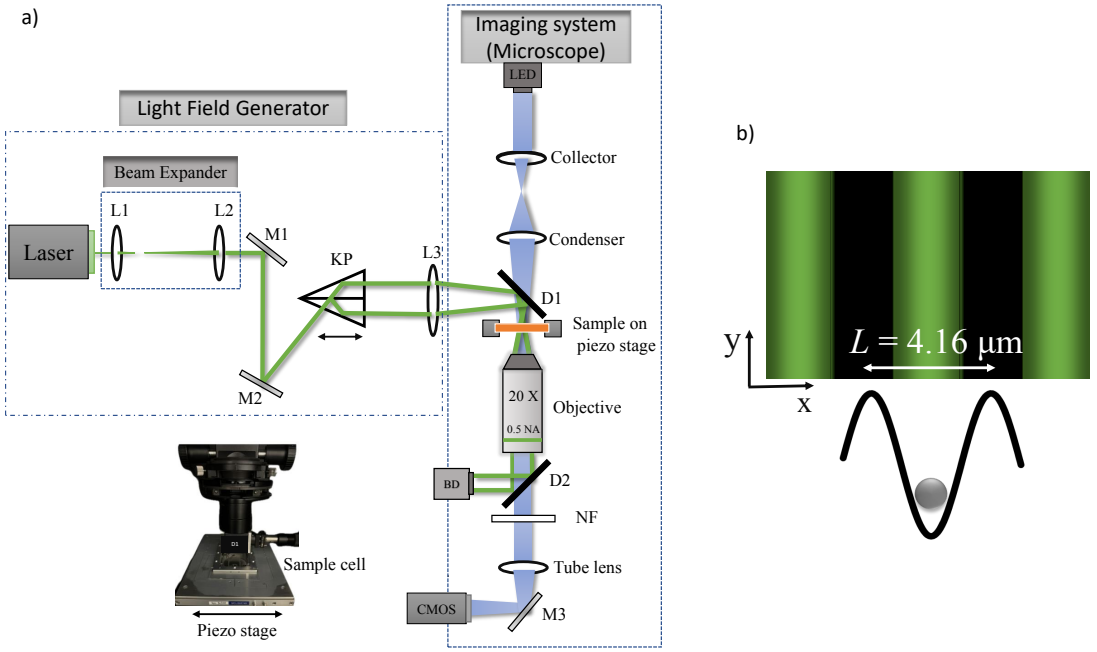

Figure 3.3: (a) In the light field generator, the laser beam is expanded (L1, L2), split (KP), and focused (L3) to form interference fringes at the sample plane. The imaging system features LED illumination, a 20× objective lens, and a CMOS camera for particle imaging. Dichroic mirrors (D1, D2), a notch filter (NF), and a beam dump (BD) ensure clean separation of imaging and trapping paths. (b) Schematic representation of the interference pattern with periodicity L and the corresponding cosine potential experienced by the colloidal particle.

3.3 Calibration methods of the optical potential

Accurate calibration of the periodic light field is essential for ensuring precise control over the potential landscape experienced by the colloidal particles. The modulation of the periodic light intensity translates directly into a spatially periodic potential, which must be characterized in terms of both amplitude and spatial periodicity.

For the calibration procedure, 3μm particles were used, when needed, in a 2D sample cell with a dilute sample corresponding to an area fraction of approximately 0.01, as described in Sec.3.1. The experimental data were recorded at 25 frames per second (fps) over a total of 180,000 frames (approximately 2 hours). For each laser power, approximately 400 to 1500 individual particle trajectories were collected from multiple measurement runs. At higher laser powers, around 20% of the particles were pushed out of the observation plane due to stronger optical forces, requiring measurements from multiple sample cells to obtain a sufficiently large dataset.

Three complementary methods are employed to calibrate the periodic potential: the light-field intensity profile method (Sec. 3.3.1), providing the periodicity L of the light field; the Boltzmann method (Sec. 3.3.2), yielding both the potential amplitude V_0 and the periodicity L from equilibrium particle distributions; and a dynamics-based approach consisting of two techniques, the long-time diffusion coefficient method (Sec. 3.3.3), determining both V_0 and L, and the intermediate scattering function (ISF), used to extract V_0.

The particle motion parallel to the fringes is purely Brownian and not affected by the external field. Therefore, we focus on the motion perpendicular to the fringes, where the influence of the periodic potential becomes apparent, and all observables in this thesis are calculated along the x-direction.

3.3.1 Light field intensity profile

The periodicity of the light field was determined by directly imaging the interference pattern. As shown in Fig. 3.4a, the intensity profile was calculated by averaging the intensity distribution along the fringes within the selected rectangular region indicated by the purple box. The intensity profile exhibits a sinusoidal modulation of gray values, corresponding to alternating bright and dark fringes. The spatial periodicity L was calculated by measuring the average distance between adjacent intensity maxima (or minima) and converting the distance from pixels to micrometers using the pixel size described in Sec. 3.1.

For the configuration shown in Fig. 3.4b, the periodicity was determined to be $L = (4.16 \pm 0.01)\mu$m, where the uncertainty represents the standard deviation. By adjusting the position of the Köster prism, this periodicity can be tuned, allowing for precise control of the optical lattice spacing. A key advantage of this method is that it provides real time feedback during the optical alignment process, enabling immediate adjustments to achieve the desired periodicity. However, this method measures the intensity distribution rather than the true potential amplitude acting on the particles. For this reason, additional methods are required to determine V_0.

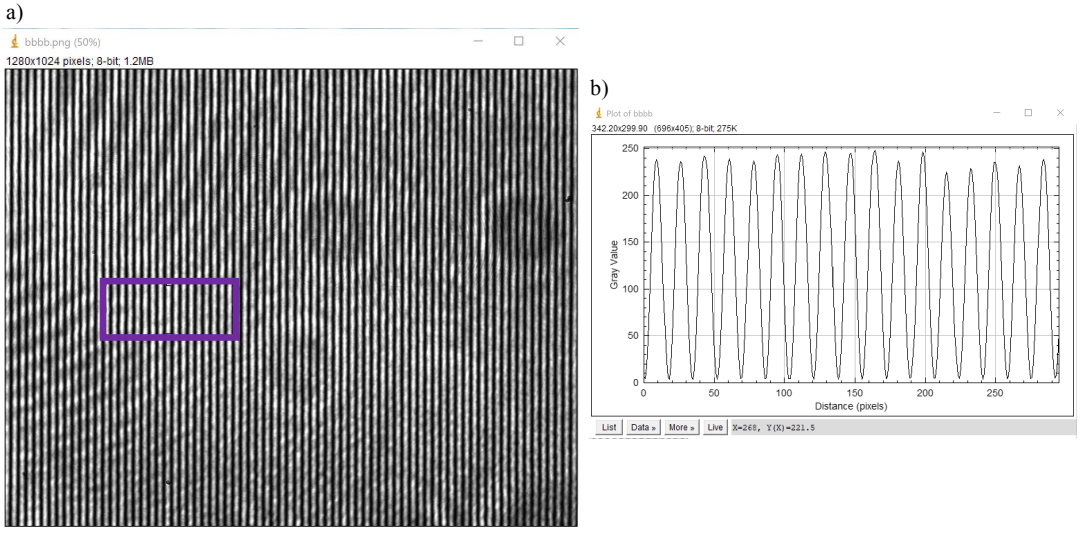

Figure 3.4: a) Microscopy image of the fringe pattern generated by the optical setup. The purple rectangle indicates the region selected for analysis. b) Intensity profile plot extracted along the selected region, showing a periodic modulation used to determine the periodicity L of the periodic light field.

3.3.2 Boltzmann

This method is based on the Boltzmann density distribution. It provides the periodicity and amplitude of the periodic light field by analyzing the equilibrium distribution of particle positions within the potential landscape. When colloidal particles are in equilibrium within a periodic potential, their positions are not uniformly distributed, instead, they follow a probability distribution that reflects the underlying energy landscape. More particles are found in low energy regions, while fewer occupy areas of higher potential energy. This equilibrium distribution is governed by the Boltzmann relation, which describes the connection between the local particle density and the potential energy at a given position[40]:

$$\langle \rho(x) \rangle = \rho_0 e^{-U_{\text{ext}}(x)/k_B T}, \tag{3.1}$$

where $\langle \rho(x) \rangle$ represents the average local particle density at position x, and ρ_0 is a normalization constant that depends on the total number of particles.

Taking the natural logarithm and the derivative of the Boltzmann distribution, Eq.3.1, we obtain:

$$\frac{d}{dx} \ln\langle \rho(x) \rangle = -\frac{1}{k_B T} \frac{dU_{\text{ext}}(x)}{dx}. \tag{3.2}$$

The advantage of taking the derivative of the logarithmic particle density is that it eliminates the normalization constant (ρ_0). For the periodic potential given in

Eq. 2.6, $U_{\text{ext}}(x) = V_0 \cos(kx) + V_{bg}$, and substituting this expression into Eq.3.2, we obtain the following

$$\frac{d}{dx} \ln\langle\rho(x)\rangle = \frac{V_0}{k_B T} k \sin(kx), \tag{3.3}$$

The Eq. 3.3 provides a practical method for extracting the potential amplitude V_0 and periodicity $L = 2\pi/k$.

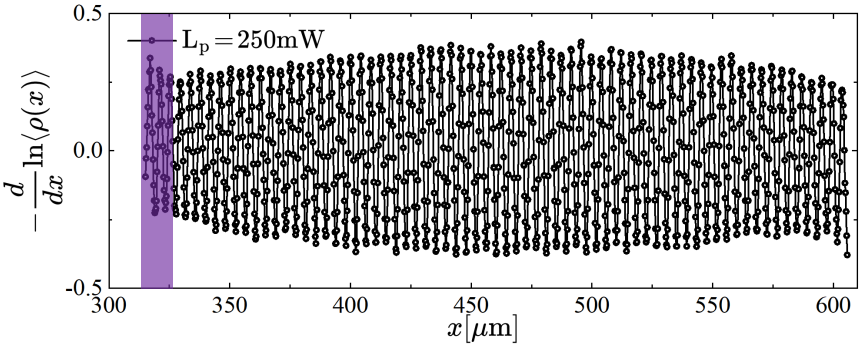

Figure 3.5: Derivative of the logarithmic particle density, for L_p=250mW. The purple region marks a representative window within the full field of view. This provides a direct estimation of the potential shape, amplitude, and periodicity.

Two complementary methods based on the Boltzmann method were employed to determine the periodic potential amplitude and periodicity: the Boltzmann method with fitting and the Boltzmann method with min and max.

In the Boltzmann method with fitting, the derivative of the logarithmic particle density is fitted to a sinusoidal function within windows spanning two periods of the potential, as indicated by the purple region in Fig. 3.5. This procedure was repeated across all windows in the field of view, and the results were averaged to obtain a reliable estimate of both the periodicity and the amplitude of the potential.

In the Boltzmann method with min and max, the amplitude was extracted directly without fitting. Within each window, the maximum and minimum values of the derivative were identified, and half of their difference was taken as the amplitude. Averaging over all windows then provides an alternative estimate of the potential amplitude.

In Fig. 3.6a, the periodicity L extracted from the Boltzmann with fitting method from each window is shown. The average periodicity was found to be $\langle L\rangle = (4.15 \pm 0.01)\,\mu$m, where the error represents the standard deviation across

all windows in the field of view. This result shows excellent agreement with the periodicity obtained from the light field intensity profile method (see Sec. 3.3.1) and the reliability of the Boltzmann distribution calibration method to extract the periodicity of the optical potential.

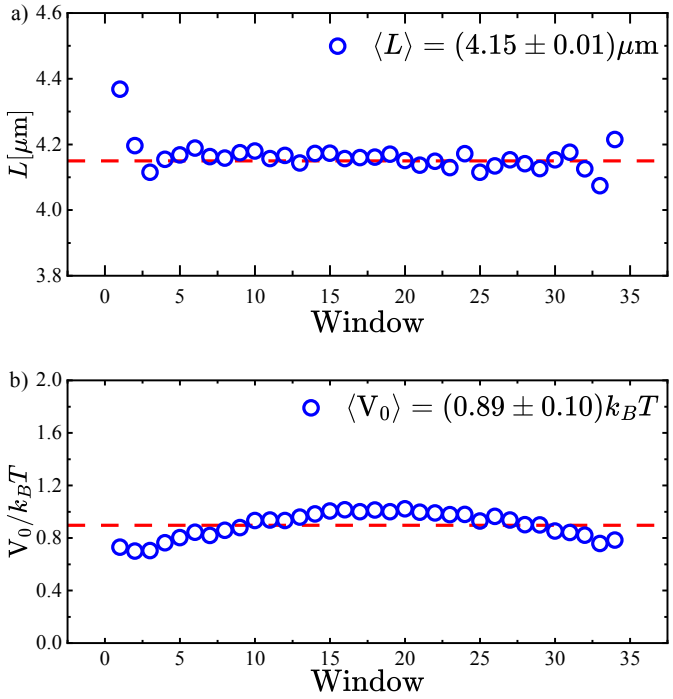

Figure 3.6: Example of Boltzmann analysis with fitting for L_p=250mW, performed over different windows along the field of view. a) Extracted periodicity L in each window, with an average value of $\langle L \rangle = (4.15 \pm 0.01)\,\mu$m. b) Corresponding potential amplitude V_0, showing a mean value of $\langle V_0 \rangle = (0.89 \pm 0.10)\,k_BT$. Red dashed lines indicate the respective average values.

From the same analysis, the corresponding potential amplitude V_0 for L_p=250mW, was obtained for all windows in the field of view, as shown in Fig. 3.6b. The average amplitude was determined to be $\langle V_0 \rangle = (0.89 \pm 0.10)\,k_BT$, where the error represents the standard deviation. This value quantifies the amplitude of the periodic potential experienced by the particles at this particular laser power. The results obtained using the min and max method have been previously shown [9], yielding a periodicity of $L = (4.15 \pm 0.01)\,\mu$m and a potential amplitude of $V_0 = (1.03 \pm 0.10)\,k_BT$ at this laser power.

The dimensionless amplitude of the potential, V_0/k_BT, obtained from the Boltzmann fitting methods and min and max over the accessible range of laser powers, are shown in Fig.3.8 as orange squares and blue circles, respectively. At

low laser powers, particles are weakly tramped and sample multiple minima. As a result, spatial heterogeneities of the optical landscape (e.g., beam envelope) are effectively averaged out, leading to smaller uncertainties and consistent V_0 values from both Boltzmann methods. At higher powers, deeper wells confine particles to fewer minima, so these heterogeneities no longer average out, the potential experience by the particles becomes more location dependent, which is reflected in broader error bars and an increased spread between the two determinations, even though the overall trend with power remains consistent.

3.3.3 Long-time diffusion coefficient

This section describes the calibration methods used to determine the potential amplitude from the normalized long-time diffusion coefficient of the particles. The normalized long-time diffusion coefficient method is one of the two dynamic analyses used in this thesis. The second method, based on the ISF, is presented in the next section. Unlike the Boltzmann method, which is based on equilibrium distributions, this approach infers the potential from the dynamical behavior of the particles. In this thesis, we study the particle dynamics perpendicular to the fringes (x-direction).

The first long-time diffusion coefficient method used here was introduced by Dalle-Ferrier et al. [41], and here referred to as the Egelhaaf method. They derived an analytical relationship between the normalized long-time diffusion coefficient and the potential amplitude.

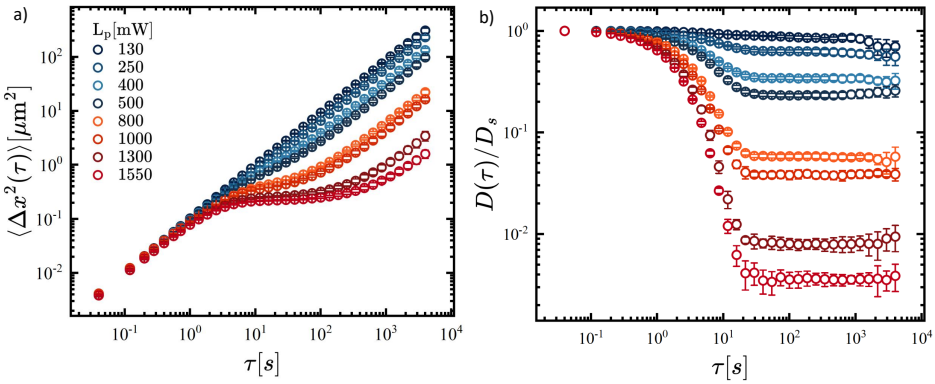

Figure 3.7: Time-dependent observables characterizing particle dynamics in a periodic potential at varying potential amplitude. a) mean squared displacement $\langle \Delta x^2(\tau) \rangle$, b) normalized time-dependent diffusivity $D(\tau)/D_s$ for different laser powers.

In this method, the potential amplitude V_0 is determined by extracting the normalized long-time diffusion coefficient D_L/D_s from the particle trajectories through the MSD and solving the expression [41]:

$$D_L/D_s = \pi \frac{2V_0}{k_B T} e^{-2V_0/k_B T}, \tag{3.4}$$

where D_L and D_s are the long- and short-time diffusion coefficients, respectively. The MSD, shown in Fig.3.7a, was calculated from the particle trajectories using Eq.2.11, the corresponding time-dependent diffusivity $D(\tau)$ was then obtained according to Eq.2.14 and subsequently normalized by the short-time diffusion coefficient D_s, as shown in Fig.3.7b. The normalized long-time diffusion coefficient D_L/D_s was determined from the plateau value of $D(\tau)/D_S$. The relationship between the normalized long-time diffusion coefficient, D_L/D_s, and the potential amplitude V_0 follows directly from Kramers' escape rate theory, which describes the rate at which particles hop between neighboring wells in a periodic potential. The escape rate depends exponentially on the barrier height:

$$\nu \sim e^{-2V_0/k_B T}. \tag{3.5}$$

It has been shown that this expression is valid in the large barrier limit, where [11]:

$$V_0/k_B T \leq 2. \tag{3.6}$$

This condition ensures that particles are predominantly confined within individual potential wells.

When the dimensionless potential amplitude $V_0/k_{\mathrm{B}}T \leq 2$, the energy barriers are comparable to the thermal energy and the assumptions of the Egelhaaf model start to break down, making the relation between D_L/D_S and V_0 less accurate. However, for higher potential amplitudes ($V_0/k_{\mathrm{B}}T > 2$), corresponding to intermediate and strong laser powers, the Egelhaaf approach provides consistent and reliable estimates of V_0, as shown in Fig. 3.8, where the results are represented by green triangles.

Another long-time diffusion coefficient method was introduced by Festa et al. [42], who provided a generalized framework for describing diffusion in periodic potentials. They derived an expression for the normalized long-time diffusion coefficient by analyzing the Smoluchowski equation, which describes Brownian motion in the overdamped limit, given by

$$D_L/D_s = \frac{1}{\left\langle e^{U_{\mathrm{ext}}(x)/k_B T} \right\rangle \left\langle e^{-U_{\mathrm{ext}}(x)/k_B T} \right\rangle}. \tag{3.7}$$

This equation accounts for the interplay between thermal fluctuations, friction, and the periodic potential, making it applicable even when the potential amplitude is

comparable to the thermal energy. Substituting $U_{\text{ext}}(x) = V_0 \cos(kx) + V_{bg}$ from Eq.2.6 into Eq.3.7 and evaluating the spatial average, $\langle \cdot \rangle$, over one period of the potential $L = 2\pi/k$, gives:

$$\left\langle e^{\pm U_{\text{ext}}(x)/k_B T} \right\rangle = \frac{1}{L} \int_0^L e^{\pm U_{\text{ext}}(x)/k_B T} \, dx = I_0\left(\frac{V_0}{k_B T}\right). \tag{3.8}$$

Here, I_0 is the modified Bessel function of the first kind. Now, substituting this average into Eq. 3.7 and using the property $I_0(-x) = I_0(x)$, they obtain the following:

$$D_L/D_s = \left[I_0\left(\frac{V_0}{k_B T}\right)\right]^{-2}, \tag{3.9}$$

known as the Festa relation, which establishes a direct connection between the normalized long-time diffusion coefficient D_L/D_s and the potential amplitude V_0. From this relation, the potential amplitude V_0 was determined based on the measured values of D_L/D_s, as presented by purple diamonds in Fig. 3.8.

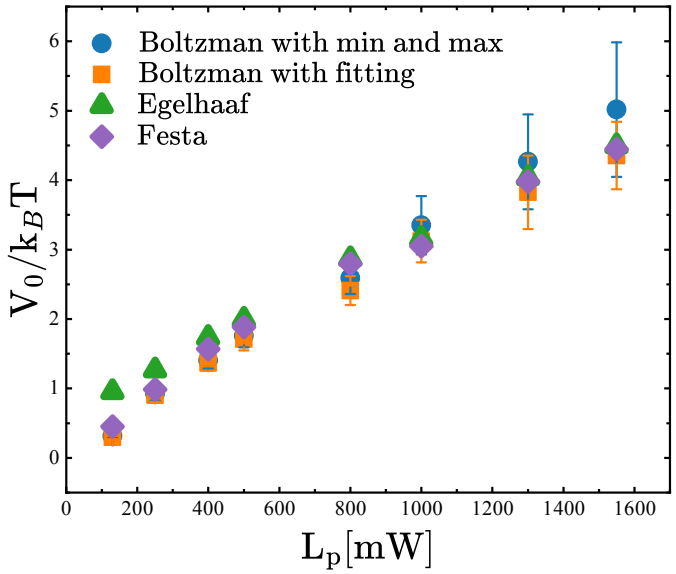

Figure 3.8: Comparison of the extracted dimensionless potential amplitude $V_0/k_B T$ as a function of laser power (L_p[mW]) using different analysis methods. Closed blue circles represent the min and max Boltzmann estimation, orange squares correspond to Boltzmann fitting, green triangles to the Egelhaaf method, and purple diamonds to the Festa method. Error bars indicate the standard deviations. All approaches show a consistent increase of V_0 with laser power.

3.3.4 Intermediate scattering function (ISF)

The second approach from dynamic analysis for extracting the potential amplitude is the ISF method, which provides a novel dynamic analysis framework in reciprocal space. This method is based on the generalized ISF, in particular on its behavior in the long-time limit for $q = 0$ (Eq. 2.40) for $\mu = \nu = 1$, i.e.,

$$F_{11}(q = 0, \tau \to \infty) = \frac{I_1^2(V_0/k_BT)}{I_0^2(V_0/k_BT)}. \tag{3.10}$$

Under these conditions, the generalized ISF represents the self-ISF evaluated at the characteristic wave number imposed on the system by the periodic potential, $Q_\mu = Q_\nu = 2\pi/L$, making the selection of μ and ν the natural choice to improve statistics to determine V_0.

As shown in Fig.3.9a, $F_{11}(q = 0, \tau \to \infty)$ presents a well-defined plateau which exhibits an opposite trend to $D(\tau)/D_s$, with higher plateaus as laser power increases. Increasing L_p leads to slower relaxation and higher long-time plateaus, indicating enhanced particle trapping within the periodic potential.

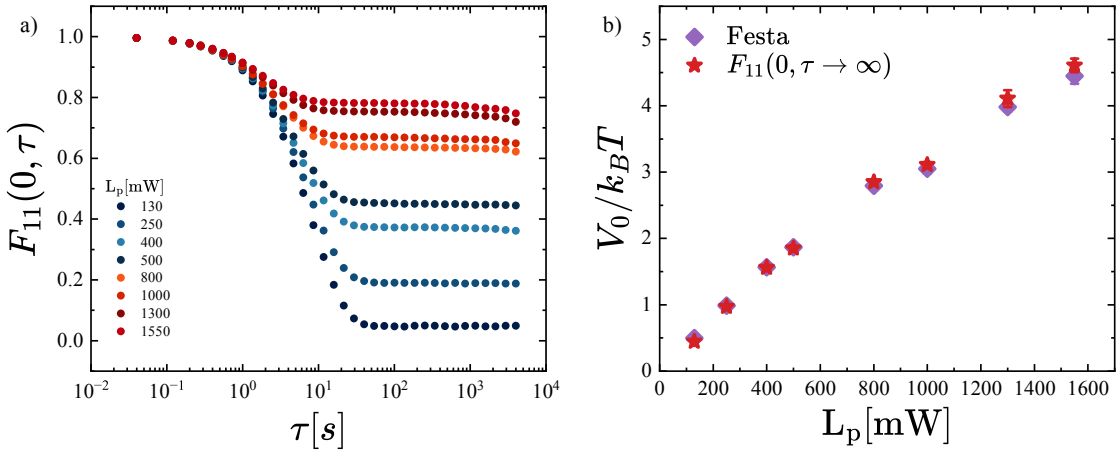

Figure 3.9: a) Generalized ISF for $q = 0$ and $\mu = \nu = 1$. Increasing L_p leads to slower relaxation and higher long-time plateaus, indicating enhanced particle trapping within the periodic potential. b) Estimated dimensionless potential amplitude V_0/k_BT as a function of L_p, extracted from the long-time limit of $F_{11}(0, \tau \to \infty)$ (red stars), and compared with independent values obtained from the Festa calibration method (purple diamonds). The agreement between the Festa approach and the ISF analysis confirms the reliability of the methods in determining the potential amplitude.

For clarity, in Fig. 3.9b, the extracted V_0 values from the ISF method are compared with those obtained using the Festa method (same shown in Fig.3.8).

Both methods yield the same results, validating the ISF method as a new approach to calibrate periodic potentials.

Each method offers advantages and limitations for calibrating the periodic light field. The light field intensity profile method provides a quick and real-time measurement of spatial periodicity; however, it does not measure the amplitude of potential experienced by the particles. The Boltzmann method enables the extraction of the potential amplitude from equilibrium distributions; nevertheless, it requires a large statistical dataset to achieve reliable results due to fluctuations in particle density. Egelhaaf's method, based on the relationship between the normalized long-time diffusion coefficient and the potential amplitude, provides an indirect yet effective means of calibration. It assumes the system remains in the high-barrier regime, where the periodic potential significantly hinders diffusion. At lower potential amplitudes, where thermal fluctuations allow particles to move more freely between wells, the method loses accuracy.

In contrast, the Festa method provides a comprehensive analytical framework that is independent of equilibrium measurements and remains applicable in both the high-barrier and low-barrier limits, making it suitable for a broader range of conditions. By directly linking the normalized long-time diffusion coefficient to the periodic potential amplitude, Festa avoids the statistical limitations of the Boltzmann approach and the regime constraints of Egelhaaf's method. Alongside Festa, the ISF approach provides a complementary, reciprocal space analysis that relies on particle correlations rather than long-time diffusion. Although the two methods are based on different dynamical observables, they yield consistent estimates of the potential amplitude. In this thesis, the Festa method is used to calibrate the light field, providing a robust, broadly applicable framework consistent with the results from the ISF approach.

3.4 Simulation

To capture the dynamical behavior of the system, Brownian dynamics simulations[1] were carried out for a dilute sample of hard disks particles chosen to reproduce the experimental area fraction of 0.01. The particle interactions followed the description provided in Section 2.2. The simulations contained 1024 particles confined within a two-dimensional rectangular domain with periodic boundary conditions applied along both the x- and y-directions.

The particle dynamics were simulated according to the reduced overdamped Langevin equation, Eq.2.34, with a time step of $d\tau^* = 2 \times 10^{-4}$. The dimensionless wave vector was set to $k^* = 1.388$, and the dimensionless potential amplitude

[1]The simulations were conducted by Dr. Manuel A. Escobedo-Sánchez. The author performed the analysis presented in this work.

V_0/k_BT was determined from the Festa method (Section 3.3.3). Each simulation was run in 1.0×10^6 steps to ensure steady-state conditions and collect statistically reliable particle trajectories.

The observables calculated from Eqs. 2.11, 2.14, 2.15, and 2.16 using the experimental trajectories are shown in Fig. 3.10, together with the corresponding results obtained from Brownian dynamics simulations for several laser powers. The trajectories obtained from the simulations were analyzed using the same procedure as for the experimental data to ensure a consistent comparison. The close cor-

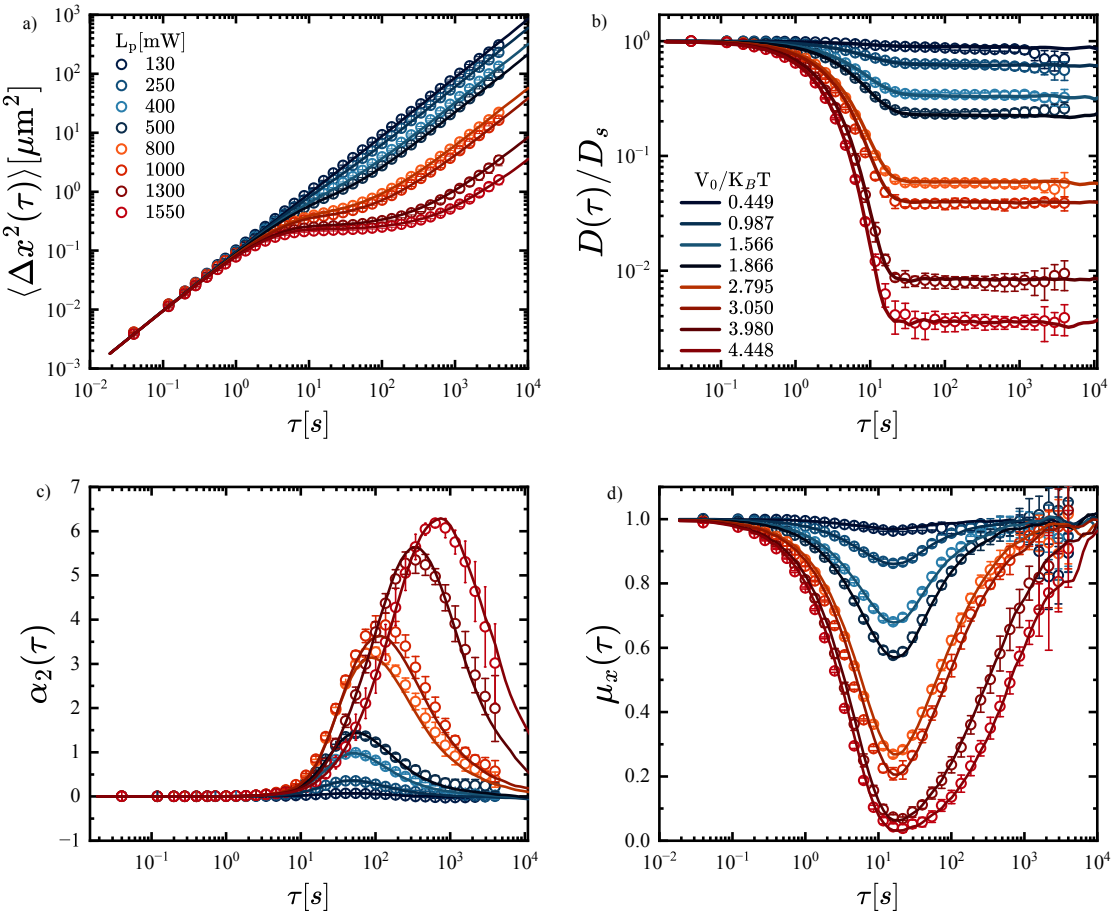

Figure 3.10: Experimental (symbols) and simulation (lines) results for time-dependent observables of particle dynamics in a periodic potential at different laser powers. a) Mean squared displacement $\langle \Delta x^2(\tau) \rangle$. b) Normalized time-dependent diffusivity $D(\tau)/D_s$. c) non-Gaussian parameter $\alpha_2(\tau)$, and d) anomalous diffusion exponent $\mu_x(\tau)$.

respondence between the experimental and simulated observables indicates that

the experiments were well calibrated and conducted under stable, controlled conditions. This consistency observed across different laser powers confirms that the potential amplitudes determined via the Festa approach accurately represent the imposed light field, ensuring that the extracted dynamical parameters can be reliably compared with theoretical predictions.

3.5 Influence of σ/L on the potential amplitude

In colloidal systems confined within periodic potentials, the ratio between the particle diameter (σ) and the periodicity of the external potential (L) plays a decisive role in the system's response, as reflected in the effective amplitude.

$$V_0 = 3g\alpha \mathrm{L_p} \frac{j_1(ka)}{ka}, \quad k = 2\pi/L. \tag{3.11}$$

Here, $\alpha = \frac{a^3 n_S^2 (n^2-1)}{n^2+2}$ is the polarizability of the particle and a its radius. The term $j_1(ka)/ka = J$ explicitly incorporates the dependence on the particle size relative to the potential periodicity, $ka = 2\pi a/L = \pi\sigma/L$. This geometric factor defines the degree of coupling between the particles and the applied potential, determining whether the modulation is perceived as a significant variation or, conversely, averaged over the spatial extent of the particles. When the diameter is much smaller than the periodicity, particles directly experience the periodic structure of the field, whereas, as the relative particle size increases, the effective interaction is attenuated due to the smoothing introduced by the finite particle extension. Analyzing this dependence provides insight into how the relative geometry governs both the effective strength of the potential and the resulting collective dynamics.

To systematically study this effect, we used two different periodicities, $L = 4.20\mu$m and $L = 4.86\mu$m, and three particle sizes, $\sigma = 3.0\mu$m, $\sigma = 4.1\mu$m, and $\sigma = 5.0\mu$m. This yields the r values reported in Table3.1.

σ [μm]	L [μm]	$r = \sigma/L$
3.0	4.20	0.71
4.1	4.20	0.98
5.0	4.20	1.19
3.0	4.86	0.61
4.1	4.86	0.84

Table 3.1: Combinations of particle diameter σ and periodicity L together with the resulting ratio $r = \sigma/L$

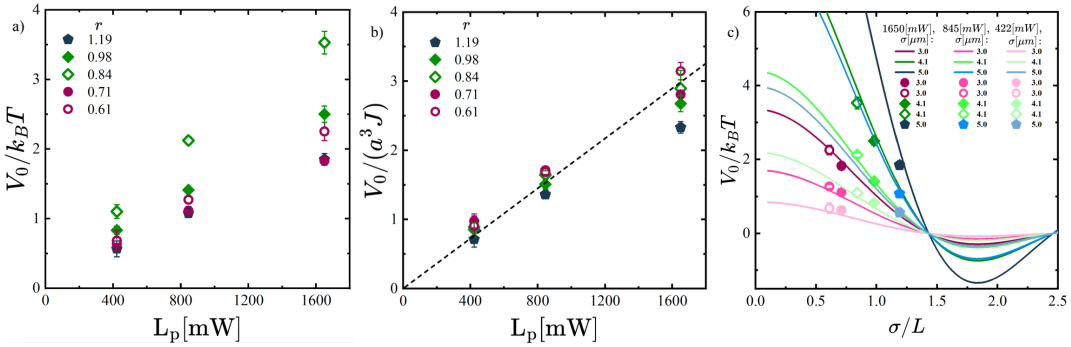

Figure 3.11: a) Potential amplitude V_0 as a function of laser power L_p for different values of the ratio σ/L, each symbol corresponds to a specific value of r, as indicated in the legend. b) Normalized potential amplitude $V_0/(a^3J)$ as a function of L_p. The dashed line represents a linear fit. c) Dimensionless potential amplitude V_0/k_BT as a function of the size ratio $r = \sigma/L$ for different laser powers L_p. The color scale, from dark to light, indicates decreasing laser power. Each solid line corresponds to a specific particle size σ and represents the theoretical prediction, using the same color as the experimental data points for direct comparison. Error bars indicate the standard deviation across multiple independent measurements.

Fig. 3.11a shows the extracted normalized potential amplitude V_0/k_BT as a function of the laser power for the five different ratios r. The amplitudes were obtained using the Festa method (see Sec.3.3.3). The results reveal a systematic influence of the ratio r on the effective amplitude of periodic potentials experienced by the particles. Among the different ratios, $r = 0.84$ ($\sigma = 4.1\mu$m, $L = 4.86\mu$m) yields the highest potential amplitude. For the same particle size ($\sigma = 4.1\mu$m), a smaller periodicity ($L = 4.20\,\mu$m, $r = 0.98$) results in a reduced amplitude. Similarly, keeping the periodicity fixed at $L = 4.86\mu$m but decreasing the particle size ($\sigma = 3.0\mu$m, $r = 0.61$) also leads to lower amplitudes. The largest ratio, $r = 1.19$, exhibits the weakest effective amplitude, as expected when the particle size is smaller than the periodicity. This general trend is consistent with the size and periodicity dependence described in Eq. (3.11) As discussed above, when the amplitudes are plotted as a function of laser power for different particle sizes and potential periodicities, the resulting curves exhibit a strong dependence on the ratio of particle diameter to lattice spacing. However, when the amplitude is normalized by the factor a^3J this explicit geometrical dependence is effectively removed. In such a representation, the data corresponding to different particle sizes and periodicities are expected to collapse onto a single curve, indicating that the underlying scaling is primarily governed by the laser power, as shown in Fig.3.11b. Any residual deviations from this collapse would then highlight

secondary contributions, such as optical absorption or experimental imperfections, rather than the intrinsic particle potential coupling. In Fig. 3.11c, we compare the theoretical prediction from Eq. 3.11 with the experimentally measured V_0/k_BT values obtained from the Festa approach for the different ratios r.

3.6 Driven colloidal dynamics in a periodic light field

Colloidal particles driven through a periodic light field represent a well-established model system for studying non-equilibrium dynamics. In this section, we investigate such a situation, focusing on the interplay between an external driving force, the optical potential, and thermal fluctuations. To achieve controlled motion, the entire sample cell was dragged through the light field using a piezo nanopositioner stage (Mad City Labs, Nano-BioS300). As a first step, the motion of colloidal particles was characterized in the absence of the light field to confirm the accuracy of the driven velocity. Four different velocities along the x-direction (perpendicular to the fringes) were programmed in the stage controller (V_s), and the corresponding particle trajectories were analyzed to compute the MSD and, from this, the normalized diffusivity $D(\tau)/D_s$ (Fig. 3.12a,b) was calculated using Eq2.14. The effective particle velocity v_{driven}, obtained using Eq. 2.21, exhibited a linear relationship with the programmed V_s (Fig. 3.12c), confirming that the imposed stage motion was faithfully transmitted to the particles.

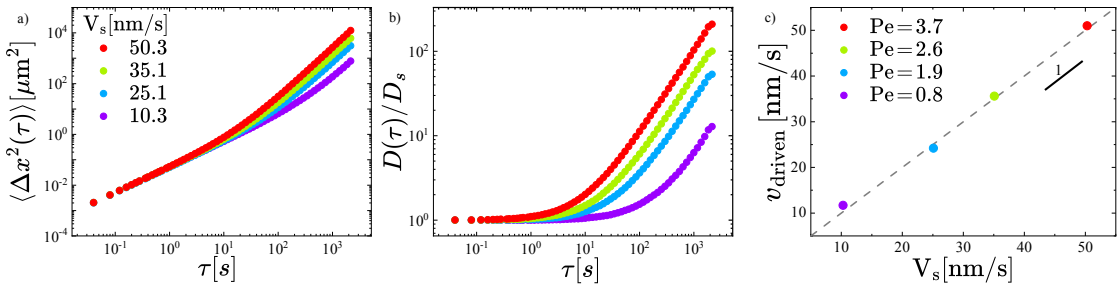

Figure 3.12: Calibration of the piezo stage. (a) MSD along the x-direction (perpendicular to the fringes) $\langle \Delta x^2(\tau) \rangle$ for different programmed stage velocities V_s. (b) Normalized time-dependent diffusivity $D(\tau)/D_s$, showing an upturn at long times due to driven velocity. (c) Comparison between the driven velocity v_{driven} extracted from the particles, inferred from the long-time behavior of $D(\tau)$, and the programmed stage velocity V_s. The dashed line with slope 1 confirms the consistency between the stage velocity and the driven velocity extracted from the particles.

With this baseline behavior characterized, we then conduct measurements in the presence of a periodic light field to investigate its effect on particle transport under constant driving velocity imposed by the piezo stage. To characterize the interplay between the imposed driving and diffusion motion, we define the dimensionless Péclet number (Pe) and defined as

$$\mathrm{Pe} = \frac{\mathrm{V_s}\sigma}{D_s}, \tag{3.12}$$

where $\mathrm{V_s}$ is the stage velocity, σ is the particle diameter, and D_s is the short-time diffusion coefficient. Since D_s exhibits variations between individual measurements (Sec.3.1.3), expressing the results in terms of Pe accounts these differences and allows for a consistent comparison under experimental conditions.

In the following, we use the Pe number as the key control parameter to define the initial state of the system. By varying the stage velocity, different values of Pe were realized.

The piezo stage moves the sample a defined distance in one direction (forward motion) and then returns it to its starting position (backward motion) at the same programmed velocity, repeating this cycle throughout the experiment. Each segment of the motion, either forward or backward, spans approximately 65,000 frames, recorded at 25 frames per second. During this motion, the sample experiences a periodic light field with an amplitude of about $1.4\,k_BT$ and the periodicity $L = 4.135\,\mu m$, chosen to be comparable to the thermal energy so that stochastic fluctuations remain significant relative to the periodic potential. All experiments were performed with 2D sample cells containing $3\,\mu$m dilute colloidal particles.

The effect of driving velocity was examined at two Péclet numbers, Pe = 1.5 and Pe = 4.0, corresponding to distinct stage velocities. Since the short-time diffusion coefficient D_s showed minor variations between measurements (see Sec.3.1.3), the stage velocity $\mathrm{V_s}$ was adjusted in each case to keep the Pe constant. The average stage velocities obtained from all measurements were $\mathrm{V_s} = (22.4 \pm 2.4)\,\mathrm{nm/s}$ and $\mathrm{V_s} = (53.5 \pm 1.7)\,\mathrm{nm/s}$ for the two conditions, respectively. These velocities were selected to cover the range from thermally dominated dynamics (Pe = 1.5) to a strongly driven regime (Pe = 4.0), allowing a systematic investigation of particle behavior under varying driving conditions.

To exclude the non-steady dynamics of the particles, which arise during the acceleration and deceleration phases of the piezo stage's motion, the particle trajectories were selected and analyzed only within the time interval where the stage velocity remained constant. The complete forward and backward image sequences were divided into eight overlapping time windows (listed in Table 3.2) to examine the temporal stability of the particle dynamics during the experiment. Each window defines a specific frame range representing the time interval used for trajec-

tory analysis. For each window, we computed the diffusivity along the x-direction, $D(\tau)$, normalized by the short-time diffusion coefficient D_s, as shown in Fig. 3.13.

Window	**Frame Range**
Window 1	1–15000
Window 2	7500–22500
Window 3	15000–30000
Window 4	22500–37500
Window 5	30000–45000
Window 6	37500–52500
Window 7	45000–60000
Window 8	52500–67500

Table 3.2: Window definitions based on frame ranges used for trajectory analysis.

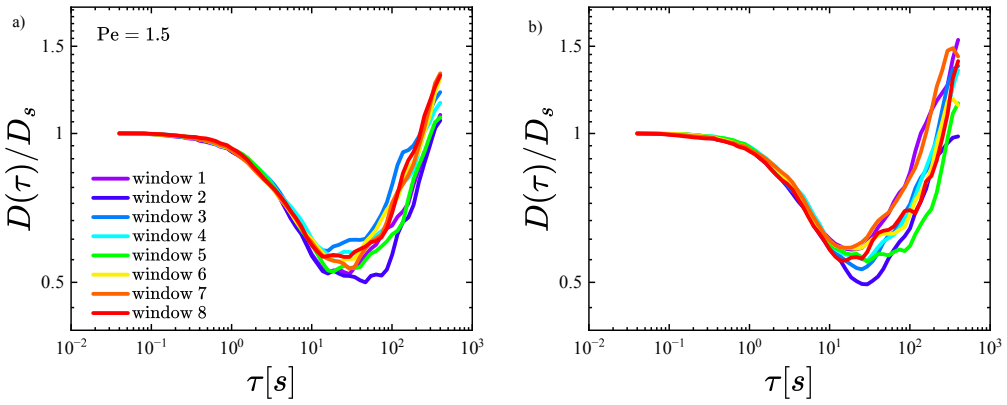

Figure 3.13: Window analysis for Pe = 1.5. a) Normalized time-dependent diffusivity $D(\tau)/D_s$ for forward motion, and b) for backward motion.

In the forward motion, windows 1 and 2 correspond to the initial acceleration phase, during which the stage velocity approaches its programmed value and the particle dynamics have not yet reached steady conditions. In the backward motion, windows 1 and 2 were also excluded because they capture the early stage of the reversed translation, when the system is again accelerating and has not yet reached steady motion. Additionally, window 8 corresponds to the deceleration phase. Therefore, for both forward and backward motion, only windows 3 to 7, corresponding to frames 15,000 to 60,000, were used for the steady-state analysis. Differences between windows 3 to 7 are attributed to measurement uncertainties, such as variations in the number of particles contributing to each window as the stage moves and different regions of the sample enter the field of view, as well as to minor nonuniformities in the light field across the observation area.

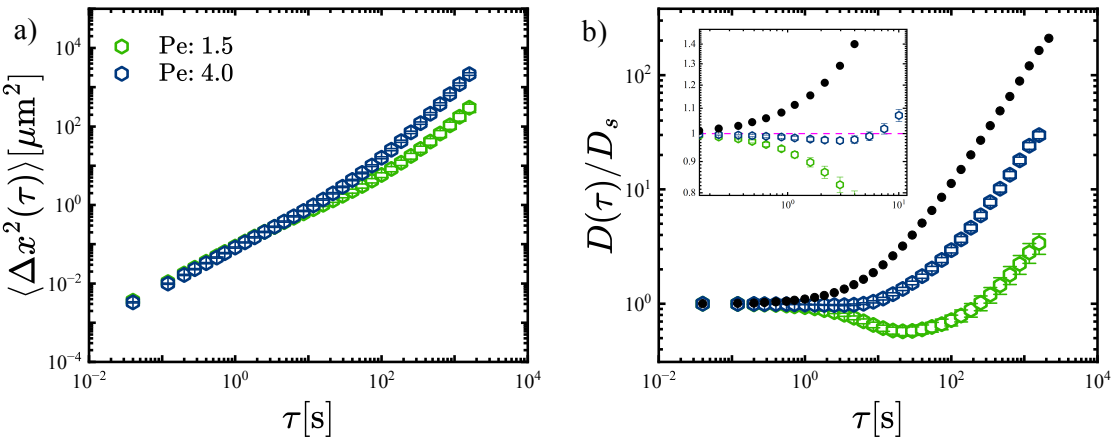

Figure 3.14: Comparison of dynamic observables for Pe = 1.5 and 4.0, corresponding to different driving velocities. a) Mean squared displacement $\langle \Delta x^2(\tau) \rangle$, b) normalized time-dependent diffusivity $D(\tau)/D_s$. The black symbols represent particles driven at the same stage velocity as Pe = 4 but in the absence of the periodic potential. The inset in panel b) highlights the short-time regime, where all curves overlap at $D(\tau)/D_s = 1$, showing that the motion is dominated by thermal fluctuations. At longer delay times, the influence of the light field becomes evident, as the diffusivity curves for Pe = 1.5 and Pe = 4.0 deviate from the reference obtained without the light field.

In Fig. 3.14, the dynamic observables of the colloidal particles are compared for two different Pe. At short delay times, all diffusivity curves coincide, meaning that thermal fluctuations dominate the motion and are not yet affected by the external drive or the periodic potential. At short delay time the normalized diffusivity converges to 1, indicating that thermal fluctuations dominate the dynamics of the particles which are not yet significantly influenced by the external driving or the periodic potential. This confirms that the motion is purely diffusive in this regime.

At intermediate delay times, a clear distinction emerges between the two driving velocities. For Pe = 1.5, the particle motion is strongly influenced by the periodic potential, as seen in the diffusivity plot by a pronounced minimum, indicating transient trapping of particles within the potential wells. In contrast, for Pe = 4, the higher stage velocity enables particles to overcome the potential barriers more frequently, leading to a shallower minimum and a faster transition toward the long-time diffusive regime. The continuous increase of the diffusivity at long delay times for both Pe numbers clearly reflects the driven character of the motion.

In conclusion, comparing different Pe numbers shows that the balance among thermal fluctuations, the periodic potential, and the external driving force governs

particle dynamics. Since the driving strength can be systematically tuned through Pe, this setup provides a well-controlled framework for studying non-equilibrium transport processes.

Chapter 4

Scientific Contributions

4.1 Intermediate scattering function of colloids in a periodic laser field

Journal: *Soft Matter*

Reference: Soft Matter, 2025,21, 4908-4924

Impact factor: 2.9

Authors: Regina Rusch, **Yasamin Mohebi Satalsari**, Angel B. Zuccolotto-Bernez, Manuel A. Escobedo-Sánchez, and Thomas Franosch

R R and **YMS** contributed equally to this work.

Author contributions:

MAES and TF conceived and administrated the project. YMS, ABZB, and MAES conducted the experimental work. RR and TF performed the analytic modeling. RR implemented the numerical analysis. YMS, MAES, and RR performed computer simulations, analyzed the experimental data, and contributed to data visualization. RR drafted the original manuscript, and all authors contributed to the manuscript.

Soft Matter

PAPER

View Article Online
View Journal

Cite this: DOI: 10.1039/d5sm00211g

Intermediate scattering function of colloids in a periodic laser field†

Regina Rusch, ‡[a] Yasamin Mohebi Satalsari, ‡[b] Angel B. Zuccolotto-Bernez,[b] Manuel A. Escobedo-Sánchez [b] and Thomas Franosch [a]

Received 28th February 2025,
Accepted 30th April 2025

DOI: 10.1039/d5sm00211g

rsc.li/soft-matter-journal

We investigate the dynamics of individual colloidal particles in a one-dimensional periodic potential using the intermediate scattering function (ISF) as a key observable. We elaborate a theoretical framework and derive formally exact analytical expressions for the ISF. We introduce and analyze a generalized ISF with two wave numbers to capture correlations in a periodic potential beyond the standard ISF. Relying on Bloch's theorem for periodic systems and, by solving the Smoluchowski equation for an overdamped Brownian particle in a cosine potential, we evaluate the ISF by numerically solving for the eigenfunctions and eigenvalues of the expression. We apply time-dependent perturbation theory to expand the ISF and extract low-order moments, including the mean-square displacement, the time-dependent diffusivity, and the non-Gaussian parameter. Our analytical results are validated through Brownian-dynamics simulations and experiments on 2D colloidal systems exposed to a light-induced periodic potential generated by two interacting laser beams.

1 Introduction

Colloidal particles suspended in fluids serve as a powerful model system in soft matter and biological physics. Their microscopic size makes them easy to manipulate, allowing researchers to explore fundamental physical principles in a controlled environment.[1–7] A major breakthrough in this field was the invention of optical tweezers by Ashkin *et al.*, which enabled the precise trapping and manipulation of individual particles using focused laser beams.[8–10] Building on this advancement, scientists have since developed laser interference patterns to create structured external potentials, offering a unique way to study how particles behave under spatially periodic forces. These optical potentials arise from the interaction between light and particles with a refractive index different from that of the surrounding medium, creating highly tunable energy landscapes.[11,12]

In order to understand how colloidal particles move within these periodic potentials, researchers have analyzed the probability distribution, the first-passage time, and low-order moments, such as the mean-square displacement, the long-time diffusivity, and the non-Gaussian parameter.[4,6,13,14] Although these observables provide valuable information, most theoretical studies have focused only on diffusion coefficients in the short- and long-time limits.[15–17] More recent work has expanded on these studies by analytically exploring tilted washboard potentials,[18,19] comparing theoretical predictions with experimental results,[20] and investigating memory effects in such systems.[21,22] These low-order moments are useful for identifying deviations from free Brownian motion, revealing effects such as trapping and non-Gaussianity.[23,24] However, they offer only a limited perspective of the system dynamics, as they do not capture the full spatial-temporal evolution of particle motion. To achieve a more complete description, it is necessary to adopt a framework that incorporates both spatial and temporal correlations.

One such framework emerges naturally in Markovian systems, where the future state depends only on the present and not on the past. In these systems, all relevant dynamical information is contained in the propagator, which describes the probability of a particle transitioning between states over a given time interval. Although the propagator provides a full statistical description of particle motion, it is often challenging to access experimentally. A more practical and experimentally accessible alternative is the intermediate scattering function (ISF), which encodes both spatial and temporal correlations in particle motion. Unlike traditional low-order moments, the ISF offers a more comprehensive characterization of the system and can be directly measured using techniques such as dynamic light scattering,[25,26] differential dynamic microscopy,[27] and single-particle tracking.[28]

[a] Institut für Theoretische Physik, Universität Innsbruck, Technikerstraße 21-A, 6020 Innsbruck, Austria. E-mail: thomas.franosch@uibk.ac.at
[b] Condensed Matter Physics Laboratory, Heinrich Heine University, Universitätsstraße 1, 40225 Düsseldorf, Germany. E-mail: escobedo@hhu.de

† We dedicate this work to the memory of our friend, mentor, and colleague Stefan U. Egelhaaf, with sincere gratitude for his contributions and dedication to the field of soft matter.

‡ R. R. and Y. S. contributed equally to this work.

Furthermore, upon a small-wave-vector expansion of the ISF the low-order moments are recovered. Analytical derivations of the ISF have been achieved for various systems, including anisotropic active Brownian particles,[23,29] Brownian circle swimmers in gravitational fields,[30–32] anisotropically diffusing colloidal dimers,[33] and run-and-tumble agents.[34,35] Notably, experimental validations have been conducted for colloidal dimers and active colloids.

In this work, we extend the traditional ISF by introducing a generalized version that incorporates two wave numbers, allowing us to investigate the correlations in periodic systems in reciprocal space. The central question we address is twofold. First, we develop a theoretical framework to gain analytic insight into the dynamics of colloidal particles in general periodic potentials. Second, we compare our predictions with experimental results, exploring a spatio-temporal regime that has not yet been fully investigated.

To develop the theoretical framework, we solve the Smoluchowski equation for a single, overdamped Brownian particle in a cosine potential. Reformulating the problem as a Hermitian Schrödinger equation allows expressing the solutions in terms of eigenvalues and eigenfunctions.[36] Taking advantage of the systems periodicity, we apply Bloch's theorem, which provides a systematic way to expand the ISF using time-dependent perturbation theory and extract key dynamical moments. These methods are based on previous work[31,32,37] and have been successfully applied to bistable periodic potentials.[38,39] To validate our theoretical predictions, we compared our theoretical framework with Brownian dynamics simulations.

Experimentally, we track individual colloidal particles confined between two walls in a two-dimensional configuration, subjected to a periodic potential created by the interference of two laser beams. By systematically varying the laser power, we control the potential amplitude and record particle trajectories under different conditions. The generalized ISF, along with its associated moments, is then extracted from these experimental data and directly compared with our theoretical predictions, enabling a precise evaluation of the Brownian motion description in periodic optical fields. By integrating theoretical modeling, experimental measurements, and computational simulations, this work aims to provide a comprehensive understanding of colloidal motion in structured environments. Our approach bridges the gap between fundamental stochastic dynamics and experimentally accessible observables, offering new insights into the interplay between Brownian motion and periodic potentials.

This work is organized as follows. In Section 2 the experimental materials and methods are described. In Section 3, we introduce the analytical model, and derive the theoretical framework and observables. Readers more interested in the results rather than the theoretical derivation may skip this section and jump directly to Section 4, where we present our findings, compare experimental results with theoretical predictions, and discuss their implications. Finally, we summarize our findings, concluding with an outlook on future research directions in this field in Section 5.

2 Material and methods

This section describes the employed numerical methods and the used experimental setup to study colloidal dynamics in periodic potentials. We describe the processes of preparing two-dimensional colloidal samples and explain our custom-built optical setup that generates periodic laser fields. Also, the experimental protocol, including data acquisition parameters and particle tracking methodology, is described. Our experimental design allows us to systematically investigate the behavior of colloidal particles under varying potential strengths while maintaining high spatial and temporal resolution, which is essential for a rigorous comparison with the theoretical framework presented in Section 3.

2.1 Numerical methods

To complement our analytical and experimental approach, we conducted Brownian-dynamics simulations of single particles in a one-dimensional cosine potential. We implemented the Euler–Maruyama method[40] for numerically solving the differential equation of motion. For efficient sampling of observables, we used the extended order-n algorithm of Frenkel and Smit, which enables equidistant sampling on a logarithmic time scale.[41–43]

To numerically solve the equation of motion, as it will be explained in detail in the theory Section 3, we employed a spectral method. Specifically, we expanded the equation in its Fourier basis to obtain its operator form. Numerically, we truncated the expansions to form a finite-dimensional matrix eigenvalue problem. We used the scipy.linalg.eig function from the SciPy library[44] to compute the eigenvalues and eigenvectors of the resulting matrix. The convergence of our results was verified by systematically increasing the truncation order until the eigenvalues stabilized to the desired precision.

2.2 Sample preparation

The experiments were performed with two-dimensional (2D) colloidal systems to ensure controlled particle motion mainly in the horizontal plane. We prepared a dilute suspension of monodisperse polystyrene sulfate latex particles (radius 1.5 μm, 4% polydispersity, Thermo Fisher Scientific, batch number 1660463) in ultra-pure water (resistivity 18.2 MΩ cm, Purelabs Flex, Elga). To build the sample cells chamber, we first attached a rectangular coverslip (Thickness No. 1, 24 × 50 mm, VWR 631-0146) to a microscope slide using UV-curing adhesive (NOA61, Norland Products Inc.). We then carefully deposited 2.5 μL of the particle suspension at the center of this base coverslip. A smaller square coverslip (Thickness No. 1.5, 22 × 22 mm, VWR 631-0125) was gently placed on top to create a thin chamber. We sealed the edges with UV-curing adhesive to prevent evaporation during long observation periods. To ensure enough space between the coverslips, particles with a radius of 2 μm were added to the colloidal suspension to act as spacers. These spacers ensure a sufficient gap between coverslips that counteracts the pull of capillary forces, preventing the coverslips from coming close to each other and squeezing the main

particles. The resulting configuration reached an area fraction of 0.01. The completed cell was positioned on the microscope stage for observation.

2.3 Experimental setup

Our experimental setup consists of a laser field generator and an imaging system, as illustrated in Fig. 1. The laser field generator creates the periodic potential experienced by the colloidal particles. A 532 nm laser (Cobolt 05-01 Samba, 1.5 W) beam passes through a beam expander and is directed by mirrors (M1 and M2) to a Köster prism (KP). This prism splits the incoming beam into two parallel beams of equal intensity, which are then focused by lens L1 and directed by a dichroic mirror (D1) into the sample plane. At the sample plane, the beams interfere to generate the laser field inducing a periodic potential, with a periodicity of $L = (4.15 \pm 0.07)$ μm. By adjusting the position of the Köster prism, we can fine-tune this periodicity. Additionally, by controlling the laser power, we can precisely modulate the amplitude of the potential experienced by the particles. The relationship between the amplitude of the potential as a function of laser power (calibration) is presented in Appendix A.

The imaging system is an inverted bright-field microscope (Nikon Ti-E) with a 20× objective (Nikon Plan Flour, 0.5 NA). We illuminate the sample with a blue LED (Thorlabs M455L4) and capture images using a CMOS camera (Mako U-130B) at a resolution of 1280 × 1024 pixels, with a pixel pitch of 0.24 μm per px. To prevent laser light from reaching the camera sensor, we employed a second dichroic mirror (D2) that redirects the laser beams to a beam dump (BD), with any residual laser light being filtered out by a notch filter (NF). This optical arrangement allows us to simultaneously apply the periodic potential and observe particle dynamics with high precision.

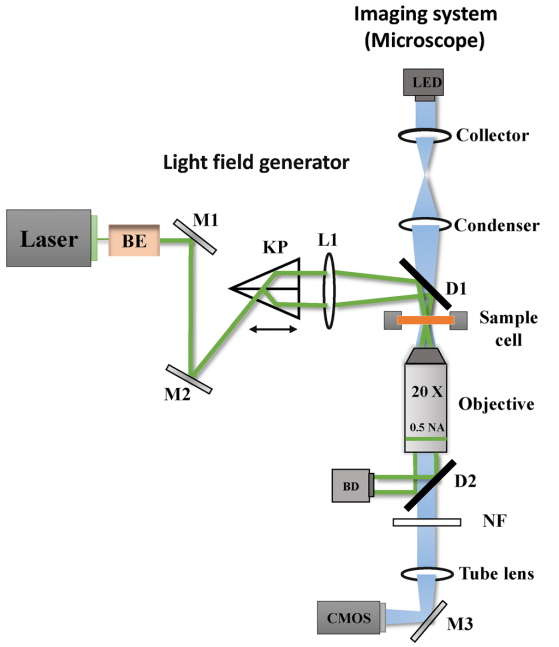

Fig. 1 Illustration of the experimental setup. The laser field generator utilizes a 532 nm laser beam to create a periodic light field through a Köster prism (KP). The two parallel beams from KP are focused on the sample plane using lens L1 and their interference creates the fringe pattern. The imaging system, consisting of a microscope with a 20× objective and a CMOS camera, captures the sample's particle trajectories.

2.4 Experimental realization

We conducted all experiments in a temperature-controlled laboratory environment maintained at 20 °C. Before measurements, samples were allowed to equilibrate for 48 hours to ensure thermal stability. For each experiment, we recorded 180 000 images over 2 hours, using a frame rate of 25 Hz and an exposure time of 1 ms. These parameters represent a balance between temporal resolution and the need to collect sufficient data for robust statistical analysis. We collected between 400 and 1500 individual particle trajectories for each laser power from several measurements. At the highest laser power, the pressure radiation pushed approximately 20% of particles out of the field of view, requiring us to sample multiple regions within each sample cell to obtain statistically meaningful datasets. To extract particle positions with high precision, we employed a custom MATLAB-based tracking algorithms adapted from the work of D. Blair and E. Dufresne[45] together with the Michalet algorithm,[46] achieving a localization uncertainty of approximately 3 nm. Trajectories are openly available in Zenodo at **https://doi.org/10.5281/zenodo.14931759**.

This exceptional spatial resolution is crucial for accurately capturing the subtle dynamics of particles within the periodic potential, particularly when comparing experimental results with theoretical predictions. The observables are computed for each measurement and averaged over all the measurements. Results in Section 4, represent the mean values and the error bars their standard deviation.

3 Theory and observables

In this section, we introduce the model and the theoretical framework. Further, we derive the generalized ISF and low-order moments. From the expansion of the ISF, we compute exact expressions of the mean-square displacement, diffusivity, and non-Gaussian parameter.

3.1 Model

We model the interaction of the colloid and the interfering laser beam by a one-dimensional periodic potential $U(x) = U(x + L)$ with period L. We assume a simple cosine potential

$$U(x) = U_1 \cos(Q_1 x), \tag{1}$$

where $Q_1 = 2\pi/L$ is the wave number associated with the period L. We introduce the dimensionless amplitude $u = U_1/k_B T$ where $k_B T$ is the thermal energy scale. The colloid is assumed to undergo Brownian motion in the presence of the spatially

periodic force $-\partial_x U(x)$. Then the equation of motion for its position $x(t)$ is provided by the Langevin equation

$$\dot{x}(t) = DQ_1 u \sin(Q_1 x(t)) + \eta(t). \tag{2}$$

Here, D denotes the short-time diffusion coefficient such that D/k_BT is the mobility as derived by the Einstein relation. The stochastic term $\eta(t)$ represents a centered Gaussian white noise with a delta-correlated variance $\langle \eta(t)\eta(t')\rangle = 2D\delta(t-t')$.

We identify three quantities which set the characteristic units of the system: The period L of the potential is the fundamental unit of length. The time a free particle needs to diffuse the distance of a period is L^2/D and will be used as a time unit. Energies are compared to the thermal energy k_BT. Therefore, the problem displays the dimensionless amplitude u as a single control parameter.

3.2 Smoluchowski equation

To make analytic progress, we rely on the Smoluchowski equation which is equivalent to the Langevin description in eqn (2) in the case of equilibrium dynamics. Here, the fundamental quantity is the propagator $\mathbb{P} := \mathbb{P}(x,t|x_0)$, defined as the conditional probability of finding the particle at position x at time t, given its initial position was x_0 at time zero. The initial condition is therefore provided by $\mathbb{P}(x,t=0|x_0) = \delta(x-x_0)$. By standard methods[36] one derives the Smoluchowski equation governing the time evolution of the propagator

$$\partial_t \mathbb{P} = -\partial_x[DQ_1 u \sin(Q_1 x)\mathbb{P}] + D\partial_x{}^2\mathbb{P} =: \Omega\mathbb{P}. \tag{3}$$

A stationary solution is provided by

$$p^{\mathrm{eq}}(x) = \frac{1}{Z_1}\exp[-U(x)/k_BT], \tag{4}$$

with a normalization factor Z_1. Since in the infinite system no stationary solution exists, we choose Z_1 as the normalizing factor for a unit cell

$$\int_0^L \mathrm{d}x p^{\mathrm{eq}}(x) = 1. \tag{5}$$

Explicitly

$$Z_1 = \int_0^L \mathrm{d}x \mathrm{e}^{-u\cos(Q_1 x)} = LI_0(u), \tag{6}$$

where $I_\nu(\cdot)$ denotes the modified Bessel function of the first kind to order ν.

We replace our infinite system with a finite system by dividing it into $N \in \mathbb{N}$ unit cells of length L and apply periodic boundary conditions. The limit $N \to \infty$ will be performed at the end of the calculations.

In order to find non-trivial solutions of eqn (3) we first perform a separation ansatz

$$\mathbb{P} = E(t)\psi(x), \tag{7}$$

and find the solution for the time-dependent part immediately as $E(t) = \mathrm{e}^{-\lambda t}$. For the position-dependent part, we have to solve an eigenvalue equation. As the Smoluchowski operator Ω is non-Hermitian, we distinguish between right and left eigenfunctions

$$\begin{aligned} \Omega\psi_\lambda^{\mathrm{R}}(x) &= -\lambda\psi_\lambda^{\mathrm{R}}(x), \\ \Omega^\dagger\psi_\lambda^{\mathrm{L}}(x) &= -\lambda^*\psi_\lambda^{\mathrm{L}}(x), \end{aligned} \tag{8}$$

and $\Omega^\dagger$ is the adjoint operator with respect to the scalar product

$$\langle\phi|\psi\rangle := \frac{1}{N}\int_0^{NL}\phi(x)^*\psi(x)\mathrm{d}x. \tag{9}$$

Left and right eigenfunctions to different eigenvalues are orthonormal, satisfying

$$\langle\psi_\lambda|\psi_{\lambda'}\rangle = \frac{1}{N}\int_0^{NL}\psi_\lambda^{\mathrm{L}}(x)^*\psi_{\lambda'}^{\mathrm{R}}(x)\mathrm{d}x = \delta_{\lambda\lambda'}. \tag{10}$$

Therefore, only the product of left and right eigenstates to identical eigenvalue is normalized. Furthermore, the eigenfunctions are complete, fulfilling the condition

$$\frac{1}{N}\sum_\lambda^\infty \psi_\lambda^{\mathrm{R}}(x)\psi_\lambda^{\mathrm{L}}(x_0)^* = \delta(x-x_0). \tag{11}$$

By comparing eqn (3) and (8) for the stationary state, we identify that the eigenfunction $\psi_0^{\mathrm{R}}(x)$ to eigenvalue zero has to be proportional to the equilibrium distribution $\psi_0^{\mathrm{R}}(x) \propto p^{\mathrm{eq}}(x)$. We choose

$$\psi_0^{\mathrm{R}}(x) = p^{\mathrm{eq}}(x), \quad \psi_0^{\mathrm{L}}(x)^* = 1, \tag{12}$$

which fulfills the normalization conditions eqn (5) and (10).

The formal solution of the Smoluchowski, eqn (3), can be written as $\mathbb{P} = \mathrm{e}^{\Omega t}\delta(x-x_0)$. We can insert the completeness relation, eqn (11), and apply the eigenvalue equation, eqn (8), and obtain

$$\mathbb{P}(x,t|x_0) = \frac{1}{N}\sum_\lambda^\infty \mathrm{e}^{-\lambda t}\psi_\lambda^{\mathrm{R}}(x)\psi_\lambda^{\mathrm{L}}(x_0)^*. \tag{13}$$

3.3 Schrödinger form

It is favorable to transform the Smoluchowski equation, eqn (3), into a Schrödinger-like equation using the 'gauge transform'[36]

$$\mathbb{P} = \mathrm{e}^{-U(x)/2k_BT}\mathbb{P}_0. \tag{14}$$

A straightforward calculation reveals that this yields in general to

$$\partial_t\mathbb{P}_0 = D\partial_x{}^2\mathbb{P}_0 - D\frac{[U'(x)]^2}{4(k_BT)^2}\mathbb{P}_0 + \frac{DU''(x)}{2k_BT}\mathbb{P}_0. \tag{15}$$

By specializing to the potential given in eqn (1), we find

$$\begin{aligned} \partial_t\mathbb{P}_0 &= \frac{D}{L^2}\left[2\pi^2 u\cos(Q_1x) - \pi^2u^2\sin^2(Q_1x)\right]\mathbb{P}_0 \\ &\quad + D\partial_x{}^2\mathbb{P}_0 =: \mathscr{L}_0\mathbb{P}_0. \end{aligned} \tag{16}$$

We note that the operator $\mathscr{L}_0$ is Hermitian with respect to the standard scalar product in eqn (9). Equivalently to the procedure of finding solutions of the Smoluchowski operator, to find the non-trivial solution of eqn (16) we perform again a separation ansatz

$$\mathbb{P}_0 = E(t)\Psi(x), \tag{17}$$

with $E(t) = e^{-\lambda t}$ and for the position-dependent part, we have to solve an eigenvalue equation

$$\mathscr{L}_0 \Psi_\lambda(x) = -\lambda \Psi_\lambda(x), \tag{18}$$

where λ represents the eigenvalue and $\Psi_\lambda(x)$ the eigenfunction. We note that the transformation of the eigenfunctions of the Schrödinger operator to the Smoluchowski operator eqn (8) is provided by

$$\psi^{\mathrm{R}}_\lambda(x) = \Psi_\lambda(x)\sqrt{p^{\mathrm{eq}}(x)}, \quad \psi^{\mathrm{L}}_\lambda(x) = \Psi_\lambda(x)\Big/\sqrt{p^{\mathrm{eq}}(x)}. \tag{19}$$

As $\mathscr{L}_0$ is an Hermitian operator, the eigenvalues are real and two eigenfunctions with different eigenvalue are orthonormal, equivalently to eqn (10). The eigenfunctions are complete, fulfilling the completeness relation, similarly to eqn (11). The eigenfunction to eigenvalue zero can be easily found using eqn (12) and (19)

$$\Psi_0(x) = \Psi_0(x)^* = \sqrt{p^{\mathrm{eq}}(x)}. \tag{20}$$

3.4 Bloch representation

For periodic systems we make use of the Bloch representation of the eigenfunctions in terms of the discrete wave vector $q \in (2\pi/NL)\mathbb{Z}$, with $-\pi/L < q \leq \pi/L$ and the discrete band index n. The wave vector can be restricted to the first Brillouin zone (BZ) because of the periodicity of the systems. The eigenfunctions are of the form

$$\Psi_{nq}(x) = e^{iqx} u_{nq}(x), \tag{21}$$

where the Bloch function $u_{nq}(x) = u_{nq}(x + L)$ is periodic, and the wave functions obtain a second index q, representing the wave number. The associated eigenvalue will be denoted by λ_{nq}. The orthonormality relation for the Bloch functions can be expressed as

$$\int_0^L \mathrm{d}x u_{nq}(x)^* u_{mq}(x) = \delta_{nm}, \tag{22}$$

see Apendix C for the detailed derivation. Also, the completeness relation still holds

$$\delta(x - x_0) = \sum_n u_{nq}(x) u_{nq}(x_0)^*, \tag{23}$$

where x and x_0 are within the same unit cell. Finally, we obtain the probability density using eqn (13) and transforming the eigenfunction of the Smoluchowski operator to the eigenfunctions of the Schrödinger operator with eqn (19). Lastly, inserting the Bloch form of the eigenfunctions we find the probability density

$$\begin{aligned}\mathbb{P}(x, t|x_0) &= \frac{1}{N}\sqrt{\frac{p^{\mathrm{eq}}(x)}{p^{\mathrm{eq}}(x_0)}} \sum_{q\in\mathrm{BZ}} \sum_n e^{-\lambda_{nq} t} \Psi_{nq}(x) \Psi_{nq}(x_0)^* \\ &= \sqrt{\frac{p^{\mathrm{eq}}(x)}{p^{\mathrm{eq}}(x_0)}} \int_{\mathrm{BZ}} \frac{L \mathrm{d}q}{2\pi} \sum_n e^{-\lambda_{nq} t} e^{iq(x-x_0)} u_{nq}(x) u_{nq}(x_0)^*,\end{aligned} \tag{24}$$

where in the last step the thermodynamic limit $N \to \infty$ was performed and therefore, the sum over the wave numbers can be replaced by an integral over the Brillouin zone (BZ).

3.5 Dirac notation

To make further progress, we introduce the compact Dirac notation where we rely on the isomorphism between the periodic square-integrable functions $u_{nq}(x) \in L^2[0,L]$ and the abstract kets $|u_{nq}\rangle$ in a separable Hilbert space $\mathscr{H}$. We introduce the generalized position basis $|x\rangle$, such that $u_{nq}(x) = \langle x|u_{nq}\rangle$. In particular, the set of associated eigenstates is orthonormal

$$\langle u_{nq}|u_{mq}\rangle = \int_0^L \mathrm{d}x \langle u_{nq}|x\rangle\langle x|u_{mq}\rangle = \delta_{nm}, \tag{25}$$

and complete

$$\sum_n |u_{nq}\rangle\langle u_{nq}| = 1, \tag{26}$$

for a given wave number q. From the completeness relation in real space

$$\delta(x - x_0) = \sum_n \sum_{q\in\mathrm{BZ}} \langle x|u_{nq}\rangle\langle u_{nq}|x_0\rangle, \tag{27}$$

we infer $\langle x|x_0\rangle = \delta(x_0 - x)$. From eqn (25) the (over-) completeness relation for the basis states $|x\rangle$ follows

$$\int_0^L \mathrm{d}x |x\rangle\langle x| = 1. \tag{28}$$

For the actual computation of the eigenfunctions we use the Fourier modes as orthonormal basis $\{|\nu\rangle: \nu \in \mathbb{Z}\}$ in $\mathscr{H}$ with real-space representation $\langle x|\nu\rangle = \exp(iQ_\nu x)/\sqrt{L}$. It is favorable to express the Bloch functions $u_{nq}(x)$ in terms of their Fourier decomposition, and we express our eigenmodes in Dirac notation

$$u_{nq}(x) = \langle x|u_{nq}\rangle = \sum_{\nu\in\mathbb{Z}} \langle x|\nu\rangle\langle\nu|u_{nq}\rangle, \tag{29}$$

where the corresponding Fourier coefficients are provided by the integral

$$\langle\nu|u_{nq}\rangle = \int_0^L \frac{\mathrm{d}x}{\sqrt{L}} e^{-iQ_\nu x} u_{nq}(x). \tag{30}$$

This is possible because all Bloch functions are lattice periodic.

3.6 Intermediate scattering function: definition and properties

We aim to analyze the characteristic function of the random displacements $\Delta x(t) := x(t) - x(0)$, which corresponds to the self-ISF and provides full spatio-temporal resolution of the particle dynamics. Making use of the periodicity of the system, we introduce the Bravais lattice, defined as $\Lambda := \{nL: n \in \mathbb{Z}\}$. The reciprocal lattice is similarly defined as $\Lambda^\star := \{Q_\mu = (2\pi\mu/L): \mu \in \mathbb{Z}\}$. Any wave vector k can be uniquely decomposed as $k = q + Q_\mu$, where $q \in$ BZ lies within the first Brillouin zone (BZ)

and $Q_\mu \in \Lambda^*$ is a reciprocal lattice vector. We define the generalized ISF

$$F_{\mu\nu}(q,t) := \langle e^{-i(q+Q_\mu)x(t)} e^{i(q+Q_\nu)x(0)} \rangle, \tag{31}$$

with the mode indices $\mu,\nu \in \mathbb{Z}$. In the following we refer to this quantity as the ISF. The brackets $\langle \cdots \rangle$ indicate an ensemble average. The conventional ISF to wave number $q + Q_\mu$ then corresponds to $F(q + Q_\mu,t) := F_{\mu\mu}(q,t)$ and probes diagonal correlations in reciprocal space. The off-diagonal elements $F_{\mu\nu}(q,t)$, $\mu \neq \nu$, encode Umklapp-processes where wave vectors differ by a reciprocal lattice vector $Q_\nu - Q_\mu$. These Umklapp-processes enter by scattering from the periodic modulation, while they are absent in the homogeneous case. Thus, $F_{\mu\nu}(q,t)$ corresponds to a matrix-valued correlation function: for a set of complex numbers $b_\mu(q) \in \mathbb{C}$ the weighted sum

$$\langle b(q,t)^* b(q,0) \rangle = \sum_{\mu,\nu\in\mathbb{Z}} b_\mu(q)^* F_{\mu\nu}(q,t) b_\nu(q), \tag{32}$$

forms an autocorrelation function, with $b(q,t) = \sum_\mu b_\mu(q) e^{i(q-Q_\mu)x(t)}$. In particular, autocorrelation functions display non-negative spectra.[47] Notably, the diagonal elements, $F_{\mu\mu}(q,t)$, are autocorrelation functions. For the case of purely relaxational dynamics, for example, Smoluchowski dynamics, autocorrelation functions are completely monotone, *i.e.*, all time derivatives exist and satisfy the inequality $(-1)^m \partial_t^m \langle b(q,t)^* b(q,0) \rangle \geq 0$ for $m \in \mathbb{N}_0$ and $t > 0$,[48] ensuring monotonically decaying, non-oscillatory behavior. In contrast, the individual off-diagonal elements, $\mu \neq \nu$, can exhibit non-monotonic behavior, including local minima or maxima.

Further, we note that the wave number q is identical in both exponentials and that the diagonal elements, $F_{\mu\mu}(q,t)$, correspond to the conventional ISF evaluated at wave vector $q + Q_\mu$. In translationally invariant systems only the diagonal elements are non-vanishing, since shifting the trajectory of a particle by an arbitrary displacement leads to an equally likely trajectory. For our case, the discrete symmetry is reflected in the sense that a common shift $x(t) \mapsto x(t) + R$ for all times by a lattice vector $R \in \Lambda$ leaves the ISF invariant. The brackets $\langle \cdots \rangle$ indicate an ensemble average.

Using the conditional probability density, the ISF of eqn (31) can be expressed as

$$\begin{aligned} F_{\mu\nu}(q,t) &= \int_0^{NL} \mathrm{d}x \int_0^L \mathrm{d}x_0 e^{-i(q+Q_\mu)x} e^{i(q+Q_\nu)x_0} \\ &\quad \times \mathbb{P}(x,t|x_0) p^{\mathrm{eq}}(x_0). \end{aligned} \tag{33}$$

Here, we used that without restriction, the initial position of the particle can be chosen to be in a definite cell and is sampled from the equilibrium distribution for this single cell.

Reversely, we can compute the probability density by the backward Fourier transform

$$\mathbb{P}(x,t|x_0) p^{\mathrm{eq}}(x_0) = \frac{1}{L^2 N} \sum_{\mu,\nu\in\mathbb{Z}} \sum_{q\in\mathrm{BZ}} F_{\mu\nu}(q,t) e^{i(q+Q_\mu)x} e^{-i(q+Q_\nu)x_0}. \tag{34}$$

see Appendix D for the derivation. The previous relation also reveals that the conventional ISF is not sufficient to reconstruct the full probability density unless the system is fully translationally invariant.

The explicit form of eqn (33) in terms of the Bloch functions is obtained by inserting eqn (24) and simplifies to express the stationary solution in terms of the eigenfunctions of the Schrödinger operator, using eqn (25). After some algebra and rearranging the terms, we find the final expression

$$\begin{aligned} F_{\mu\nu}(q,t) &= \sum_n e^{-\lambda_{nq} t} \left[\int_0^L \mathrm{d}x e^{-iQ_\mu x} u_{nq}(x) u_{00}(x)^* \right] \\ &\quad \times \left[\int_0^L \mathrm{d}x_0 e^{-iQ_\nu x_0} u_{nq}(x_0) u_{00}(x_0)^* \right]^*, \end{aligned} \tag{35}$$

see Appendix D for more details.

To determine the functions $u_{nq}(x)$ we introduce the operator $\mathscr{L}_q$ for which the eigenvalue equation

$$\mathscr{L}_q u_{nq}(x) = -\lambda_{nq} u_{nq}(x), \tag{36}$$

holds. Straightforward substitution leads to

$$\mathscr{L}_q := \frac{D\pi^2}{L^2} \left[2u \cos(Q_1 x) - u^2 \sin^2(Q_1 x) \right] + D\partial_x^2 + 2iqD\partial_x - Dq^2, \tag{37}$$

which can be abbreviated as $\mathscr{L}_q = \mathscr{L}_0 + \delta\mathscr{L}_q$. Here, the operator $\mathscr{L}_0$ (first three terms) encodes the interaction of the diffusive particle with the potential and the q-dependent operator $\delta\mathscr{L}_q$ (last two terms) contains a drift or advection-like term, linear in the wave number, and a diffusion-like term proportional to q^2.

The matrix representation of the operator, is given by

$$\begin{aligned} \langle \mu | \mathscr{L}_0 | \nu \rangle &= \int_0^L \frac{\mathrm{d}x}{L} e^{-iQ_\mu x} \mathscr{L}_0 e^{iQ_\nu x} \\ &= \frac{D\pi^2}{L^2} \Big[u \big(\delta_{\mu,\nu+1} + \delta_{\mu,\nu-1} \big) \\ &\quad + \frac{u^2}{4} \big(\delta_{\mu,\nu+2} - 2\delta_{\mu,\nu} + \delta_{\mu,\nu-2} \big) - 4\mu^2 \delta_{\mu,\nu} \Big], \end{aligned} \tag{38}$$

and

$$\langle \mu | \delta\mathscr{L}_q | \nu \rangle = (-4\pi q D\nu/L - Dq^2) \delta_{\mu,\nu}. \tag{39}$$

The matrix $\mathscr{L}_0$ is a Hermitian matrix and pentadiagonal in the Fourier basis, *i.e.*, it has non-zero elements only on the main diagonal and the two diagonals above and below it. The q-dependent matrix is diagonal in the Fourier basis. The eigenvalue problem $\mathscr{L}_q |u_{nq}\rangle = -\lambda_{nq} |u_{nq}\rangle$ is computed numerically by diagonalizing the (truncated) Hermitian matrix

$$\sum_{\nu\in\mathbb{Z}} \langle \mu | \mathscr{L}_q | \nu \rangle \langle \nu | u_{nq} \rangle = -\lambda_{nq} \langle \mu | u_{nq} \rangle. \tag{40}$$

The time evolution of the ISF is encoded in the eigenvalues and eigenfunctions of the operator $\mathscr{L}_q$. The eigenvalues λ_{nq} form continuous bands as the number of cells goes to infinity, $N \to \infty$, see Fig. 2. All eigenvalues are non-negative, and the only zero eigenvalue is in the center of the Brillouin zone at the

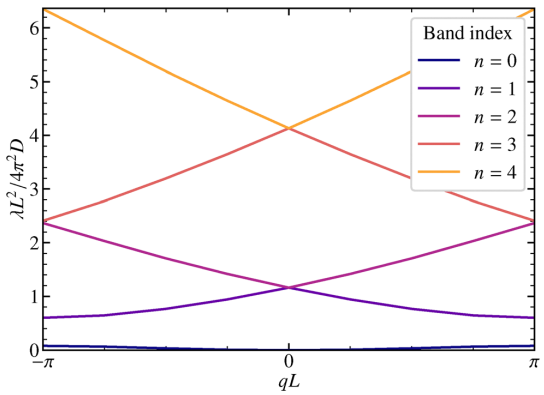

Fig. 2 Eigenvalues λ_{nq} of the operator $\mathscr{L}_q$ for $U_1 = 1.0k_BT$ are shown, for the five lowest bands in the first Brillouin zone.

lowest band. Only the lowest bands are significantly affected by the potential $U(x)$. For $\lambda \gtrsim \pi^2 Du/L^2$ the bands correspond to a particle freely diffusing without underlying potential modulation. Albeit the bands come very close at the edges of the Brillouin zone, we checked numerically that they do not touch. For symmetric potentials the avoided crossing theorem does not apply and in principle bands can cross. For the simple cosine potential, one can actually show that all eigenvalues for $q = 0$ except for $\lambda_{00} = 0$ are twofold degenerate, see Appendix C.

Finally, the ISF in eqn (35) can be conveniently expressed in a spectral representation using the Fourier basis

$$F_{\mu\nu}(q,t) = \sum_n \mathrm{e}^{-\lambda_{nq}t} \sum_{\sigma,\tau\in\mathbb{Z}} \langle u_{00}|\sigma\rangle\langle\sigma+\mu|u_{nq}\rangle\langle u_{nq}|\tau+\nu\rangle\langle\tau|u_{00}\rangle, \tag{41}$$

see Appendix D for the derivation. The previous relation reveals that $\sum_{\mu,\nu} b_\mu(q)^* F_{\mu\nu}(q,t) b_\nu(q)$ is completely monotone.

Of particular interest is the conventional ISF with wave vector in the first Brillouin zone, $F(q,t) := F_{00}(q,t)$, which simplifies upon exploiting the completeness of the Fourier basis

$$F(q,t) = \sum_n \mathrm{e}^{-\lambda_{nq}t}\langle u_{00}|u_{nq}\rangle\langle u_{nq}|u_{00}\rangle = \langle u_{00}|\mathrm{e}^{\mathscr{L}_q t}|u_{00}\rangle. \tag{42}$$

Since all eigenvalues are strictly larger than zero, except for $\lambda_{00} = 0$ in the lowest band and in the center of the Brillouin zone, $F(q,t)$ decays to zero for large time, $t \to 0$ for $q \neq 0$.

3.6.1 Symmetry relations. The symmetries of the generalized ISF are derived following the same arguments as in ref. 49. For equilibrium dynamics, time inversion symmetry holds and the ISF is even in time. Time-translation invariance then reveals the relations

$$F_{\mu\nu}(q,t) = F_{\mu\nu}(q,-t) = F_{\nu\mu}(q,t)^*. \tag{43}$$

For symmetric potentials $U(-x) = U(x)$, space-inversion symmetry implies

$$F_{\mu\nu}(q,t) = F_{\mu\nu}(q,t)^* = F_{-\mu,-\nu}(-q,t). \tag{44}$$

In particular, the ISF is a real quantity and symmetric upon interchanging its mode indices. At the edge of the Brillouin zone we have the additional relation

$$F_{\mu\nu}(\pi/L,t) = F_{\mu+1,\nu+1}(-\pi/L,t) = F_{-(\mu+1),-(\nu+1)}(\pi/L,t). \tag{45}$$

3.6.2 Short- and long-time limits. For the simple cosine potential, eqn (1), the short-time limit of the ISF can be calculated explicitly

$$F_{\mu\nu}(q,t=0) = \langle \exp(-iQ_{\mu-\nu}x(0))\rangle = \int_0^L \mathrm{e}^{-iQ_{\mu-\nu}x} p^{\mathrm{eq}}(x)\mathrm{d}x = (-1)^{\mu-\nu}\frac{I_{\mu-\nu}(u)}{I_0(u)}. \tag{46}$$

From eqn (35) and $u_{00}(x) = \sqrt{p^{\mathrm{eq}}(x)}$, one infers that for $q = 0$ the ISF displays a non-vanishing long-time limit

$$F_{\mu\nu}(0,t\to\infty) = \langle \mathrm{e}^{-iQ_\mu x(t)}\rangle\langle \mathrm{e}^{iQ_\nu x(0)}\rangle. \tag{47}$$

The factorization of the limit can be interpreted as the system being ergodic. For the simple cosine potential, eqn (1), the limit can be calculated explicitly

$$F_{\mu\nu}(0,t\to\infty) = \frac{(-1)^{\nu+\mu} I_\mu(u) I_\nu(u)}{I_0^2(u)} \tag{48}$$

An equivalent formal expression for the long-time limit follows from eqn (41)

$$F_{\mu\nu}(0,t\to\infty) = \left[\sum_{\sigma\in\mathbb{Z}}\langle u_{00}|\sigma\rangle\langle\sigma+\mu|u_{00}\rangle\right]\left[\sum_{\tau\in\mathbb{Z}}\langle u_{00}|\tau+\nu|u_{00}\rangle\langle\tau|u_{00}\rangle\right]. \tag{49}$$

Since $u_{00}(x) = \sqrt{p^{\mathrm{eq}}(x)}$ and employing the Jacobi–Anger expansion,[50] the Fourier coefficients $\langle\mu|u_{00}\rangle$ can be calculated explicitly

$$\langle\mu|u_{00}\rangle = \frac{(-1)^\mu I_\mu(u/2)}{\sqrt{I_0(u)}}. \tag{50}$$

With Neumann's addition theorem for modified Bessel functions[50] the sums in eqn (49) can be performed and we recover eqn (48). Note that eqn (46) and (48) represent static quantities that only depend on the potential amplitude.

3.7 Mean-squared displacement and non-Gaussian parameter

The goal of this subsection is to elaborate the low-order moments of the fluctuating variable $\Delta x(t)$. They can be derived from the conventional ISF, $F(q,t) = F_{00}(q,t)$, which is the characteristic function of the random displacements. As moments of odd order vanish by symmetry, we compute only the even moments. The lowest nontrivial is the time-dependent mean-squared displacement $\langle[\Delta x(t)]^2\rangle$. We also define the time-dependent diffusion coefficient *via* the derivative of the mean-squared

displacement (MSD)

$$D(t) := \frac{1}{2}\frac{\mathrm{d}\langle[\Delta x(t)]^2\rangle}{\mathrm{d}t}. \tag{51}$$

The long-time dynamics is diffusive, in particular, the long-time limit $D_\infty := D(t \to \infty) > 0$ is finite and defines the long-time diffusion constant. An analytic expression for arbitrary periodic potentials is known.[15,16,18,22,51] In particular, for the simple cosine potential it evaluates to

$$D_\infty = \frac{D}{I_0^2(u)} = 2\pi D e^{-2u}[u + O(1)] \quad \text{for } u \to \infty. \tag{52}$$

The exponential suppression of the diffusion constant reflects Kramers's rule for hopping over a potential barrier.[36] A convenient measure to discuss deviations from simple diffusion is the non-Gaussian parameter[47,52]

$$\alpha_2[\Delta x(t)] := \frac{\langle[\Delta x(t)]^4\rangle}{3\langle[\Delta x(t)]^2\rangle} - 1. \tag{53}$$

The derivation for extracting the moments from the ISF is similar to ref. 31 and 32 with only the essential steps presented here. The key idea is to apply perturbation theory for small wave numbers q and compare it to the Taylor series of the ISF, which yields the moments

$$F(q,t) = 1 - \frac{q^2}{2}\langle[\Delta x(t)]^2\rangle + \frac{q^4}{4!}\langle[\Delta x(t)]^4\rangle + \cdots, \tag{54}$$

where we already exploited that all odd-order moments vanish. The ISF, eqn (42), will be expanded in powers of q by $\mathscr{L}_q = \mathscr{L}_0 - Dq^2 + \delta\mathscr{L}_q^1$ with $\delta\mathscr{L}_q^1 = 2iqD\partial_x$. We rely on the Dyson representation

$$\mathrm{e}^{(\mathscr{L}_0+\delta\mathscr{L}_q^1)t} = \mathrm{e}^{\mathscr{L}_0 t} + \int_0^t \mathrm{d}s \mathrm{e}^{\mathscr{L}_0(t-s)}\delta\mathscr{L}_q^1 \mathrm{e}^{(\mathscr{L}_0+\delta\mathscr{L}_q^1)s}. \tag{55}$$

Replacing the time-evolution operator in the integral on the right-hand side iteratively generates the Born series, see ref. 32. The main simplification steps are to make use of the fact that $\mathrm{e}^{\mathscr{L}_0 t}|u_{n0}\rangle = |u_{n0}\rangle$ and also $\langle u_{n0}|\mathrm{e}^{\mathscr{L}_0 t} = \langle u_{n0}|$ and to insert complete basis sets, eqn (26), for $q = 0$. Occurring integrals can be formally evaluated and the terms are simplified to obtain the final result, which is similar to the result in ref. 32, but slightly changed for our operator and eigenvectors. We find the formal expression

$$\begin{aligned} F(q,t) &= \mathrm{e}^{-Dq^2 t}\left\langle u_{00}\middle|\mathrm{e}^{(\mathscr{L}_0+\delta\mathscr{L}_q^1)t}\middle|u_{00}\right\rangle \\ &= \mathrm{e}^{-Dq^2 t}\left[1 + \frac{q^2}{2}\tilde{F}_2(t) + \frac{q^4}{4!}\tilde{F}_4(t) + O(q^6)\right], \end{aligned} \tag{56}$$

with

$$\tilde{F}_2(t) = \frac{2}{q^2}\sum_n \frac{\mathrm{e}^{-\lambda_{n0}t} + \lambda_{n0}t - 1}{{\lambda_{n0}}^2}\left\langle u_{00}\middle|\delta\mathscr{L}_q^1\middle|u_{n0}\right\rangle\left\langle u_{n0}\middle|\delta\mathscr{L}_q^1\middle|u_{00}\right\rangle$$

and,

$$\begin{aligned} \tilde{F}_4(t) &= \frac{24}{q^4}\sum_n\sum_m\sum_p \left[\frac{\mathrm{e}^{-\lambda_{n0}t} + \lambda_{n0}t - 1}{{\lambda_{n0}}^2(\lambda_{n0}-\lambda_{m0})(\lambda_{n0}-\lambda_{p0})}\right. \\ &\quad + \frac{\mathrm{e}^{-\lambda_{m0}t} + \lambda_{m0}t - 1}{{\lambda_{m0}}^2(\lambda_{m0}-\lambda_{n0})(\lambda_{m0}-\lambda_{p0})} \\ &\quad \left. + \frac{\mathrm{e}^{-\lambda_{p0}t} + \lambda_{p0}t - 1}{{\lambda_{p0}}^2(\lambda_{p0}-\lambda_{m0})(\lambda_{p0}-\lambda_{n0})}\right] \\ &\quad \times \left\langle u_{00}\middle|\delta\mathscr{L}_q^1\middle|u_{n0}\right\rangle\left\langle u_{n0}\middle|\delta\mathscr{L}_q^1\middle|u_{m0}\right\rangle \\ &\quad \times \left\langle u_{m0}\middle|\delta\mathscr{L}_q^1\middle|u_{p0}\right\rangle\left\langle u_{p0}\middle|\delta\mathscr{L}_q^1\middle|u_{00}\right\rangle. \end{aligned} \tag{57}$$

Here, all sums over n, m, p include all bands and therefore formally the expression causes divisions by zero if a band index corresponds to the lowest band or two band indices correspond to the same band. In both cases the corresponding numerators also vanish. The appearance of the zero divisors can be avoided in the first place by handling these case separately before performing the integrals in the simplification steps. Here we follow a different route to keep the expressions simple by analytically continuing the expression for the case of zero numerators/denominators.

A further complication arises in the case of a simple cosine potential, since all eigenvalues λ_{n0} are, additionally, twofold degenerate, except for the ground state causing additional zero divisors. However, as in degenerate perturbation theory, one can choose basis states such that the matrix elements of $\delta\mathscr{L}_q^1$ coupling different states to the same eigenvalues vanish. Since $\mathscr{L}_q^1$ anticommutes with space inversion, only states of different parity couple, however, because u_{n0} are either even or odd, no zero divisors occur.

The low-order cumulants of the random variable $\Delta x(t)$ are generated upon expanding the logarithm of the ISF in powers of the wave number q

$$\ln F(q,t) = -\frac{q^2}{2}\langle[\Delta x(t)]^2 + \frac{q^4}{4!}\left\{\langle[\Delta x(t)]^4\rangle - 3\langle[\Delta x(t)]^2\rangle^2\right\} + O(q^6). \tag{58}$$

To order $O(q^2)$ we find the mean-square displacement as first nonvanishing cumulant

$$\begin{aligned} \langle[\Delta x(t)]^2\rangle &= 2Dt \\ &\quad - \frac{2}{q^2}\sum_{n\neq 0}\frac{\mathrm{e}^{-\lambda_{n0}t} + \lambda_{n0}t - 1}{{\lambda_{n0}}^2}\left\langle u_{00}\middle|\delta\mathscr{L}_q^1\middle|u_{n0}\right\rangle\left\langle u_{n0}\middle|\delta\mathscr{L}_q^1\middle|u_{00}\right\rangle, \end{aligned} \tag{59}$$

where no contributions from $n = 0$ as intermediate state arises since the transition matrix element vanishes

$$\left\langle u_{00}\middle|\delta\mathscr{L}_q^1\middle|u_{00}\right\rangle = 2iqD\int_0^L u_{00}(x)^*\partial_x u_{00}(x) = 0, \tag{60}$$

where the last equality follows by integration by parts and observing that $u_{00}(x)$ is real. The time-dependent diffusion coefficient, eqn (51), can be computed using the

time-derivative of eqn (59).

$$D(t) = D + \frac{1}{q^2}\sum_{n\neq 0}\frac{e^{-\lambda_{n0}t}-1}{\lambda_{n0}}\left\langle u_{00}\middle|\delta\mathscr{L}_q^1\middle|u_{n0}\right\rangle\left\langle u_{n0}\middle|\delta\mathscr{L}_q^1\middle|u_{00}\right\rangle. \quad (61)$$

For the fourth cumulant we need to collect terms of order $O(q^4)$ and we obtain

$$\langle[\Delta x(t)]^4\rangle - 3\langle[\Delta x(t)]^2\rangle^2 = \tilde{F}_4(t) - 3[\tilde{F}_2(t)]^2. \quad (62)$$

For completeness, let us argue explicitly that all odd powers in q in the expansion of $F(q,t)$, eqn (56), vanish. A term linear in q corresponding to a mean drift would involve the matrix element $\langle u_{00}|\delta\mathscr{L}_q^1|u_{00}\rangle$ which is shown to vanish in eqn (60). This vanishing of the mean drift is, of course, a general property in equilibrium. For any symmetric potential all odd moments vanish. The expansion of $F(q,t)$ in eqn (56) generates a chain $\langle u_{00}|\delta\mathscr{L}_q^1|u_{n0}\rangle\langle u_{n0}|\ldots|u_{p0}\rangle\langle u_{p0}|\delta\mathscr{L}_q^1|u_{00}\rangle$ in eqn (57) of products of matrix elements. By parity and the property of the operator $\delta\mathscr{L}_q^1$ a matrix element is non-vanishing only if the states are of different parity. Thus, for the chain to yield a non-vanishing contribution, the first intermediate state has to be odd, the second even, and so on. However, the last state is the ground state again which is even. Therefore, only even powers of q are generated.

4 Comparison of the theoretical framework with experimental and simulation results

In this section, we analyze the observables and compare the theoretical predictions with the experimental results. First, we examine the diagonal and off-diagonal elements of the ISF for various wave numbers and potential amplitudes. Next, we discuss the mean-square displacement (MSD), time-dependent diffusivity, and the non-Gaussian parameter for different potential amplitudes. To facilitate the comparison with the experimental results, we restore units; in particular, we use the amplitude of the modulation U_1, eqn (1), as a control parameter. The presented experimental results correspond to the mean of multiple measurements, with error bars indicating the standard deviation. Each measurement consisted of a sufficiently large number of recorded trajectories, from which the observable of interest was computed as an average. To enable comparison with theoretical predictions, we established the relationship between the potential amplitude U_1 and laser power (LP) (see Appendix A for details). Additionally, length and time scales were calibrated by determining the short-time diffusion coefficient D and the characteristic period L from the experimental data. We determined from the initial slope of the mean-square displacement an average short-time diffusion coefficient of $(0.050 \pm 0.002)\ \mu m^2\ s^{-1}$.

4.1 Diagonal ISF, $\mu = \nu$

The diagonal ISF is computed from our experimental data relying on the definition given in eqn (31) for $\mu = \nu$. We have checked that its imaginary part is in deed negligible reflecting the mirror symmetry of the potential. We compare the experimental results to the numerical ones relying on the spectral representation in eqn (41). Last, all results are corroborated by Brownian-dynamics simulations. The ISF is displayed in Fig. 3 for a range of different wave numbers $Q_\mu \in \Lambda^*$ and $q \in$ BZ for three distinct amplitudes U_1.

We first focus on the behavior for $q \neq 0$, where all ISF eventually relax to zero. For moderate potential amplitudes $U_1 \approx k_BT$, the potential is not high enough to significantly inhibit hopping between different potential valleys, yielding a single-step relaxation. For larger amplitudes, a two-step process occurs. The particle initially freely diffuses with short-time diffusion coefficient D until the potential forces become dominant. For $U_1 \gtrsim k_BT$ the motion occurs essentially at the bottom of the potential, which can be approximated by a harmonic well

$$U(x) \approx -U_1 + \frac{U_1 Q_1^2 (x - L/2)^2}{2}. \quad (63)$$

The particle then locally equilibrates on the time scale of the harmonic relaxation time, $\tau = (L^2/4\pi^2 D)(k_BT/U_1)$, and the ISF saturates at a plateau value, see Fig. 3. The ISF within the harmonic approximation can be calculated explicitly, see Appendix E. For large barriers, Fig. 3(c), the harmonic approximation quantitatively describes the relaxation to the plateau value for wave numbers resolving smaller length scale than a period L. The relaxation from the plateau occurs on a much larger time scale provided by Kramers' theory $\tau_K \propto \exp(2U_1/k_BT)$. Once the particle overcomes the barrier and reaches additional minima, the ISF eventually decays to zero. For small wave numbers and long times, the hydrodynamic regime is reached $F_{00}(q,t) = \exp(-D_\infty q^2 t)$. In this regime, the wave numbers only resolve the motion over many periods at time scales much larger than Kramers' escape time. Our analytical predictions as well as the simulation results within the Smoluchowski picture of a simple cosine potential show excellent agreement with the experimental results.

For the wave number in the center of the BZ, $q = 0$, the ISF does not decay to zero in the long-time limit $t \to \infty$, rather approaches a finite value, as computed in eqn (48). In Appendix A we used this feature to calibrate the laser power of the experiment to the theoretical k_BT value.

4.2 Off-diagonal ISF, $\mu \neq \nu$

For the off-diagonal ISF, $\mu \neq \nu$, we present results for different modes corresponding to $|\mu - \nu| = 1$ and $|\mu - \nu| = 2$. The results are shown for three different wave numbers q and the amplitude $U_1 = 0.99k_BT$, see Fig. 4. The general symmetries of the ISF for symmetric potentials are summarized in eqn (43) and (44).

For wave numbers at the edge of the BZ $q = \pi/L$ additional symmetries of the ISF, eqn (45), hold. For example, the curves for $(\mu, \nu) = (1, -1)$ and $(0, -2)$, or $(1,0)$ and $(-1, -2)$ are identical.

For $q = 0$ both the initial value and the long-time limit are non-zero. As soon as $q \neq 0$ the curves decay to zero for long

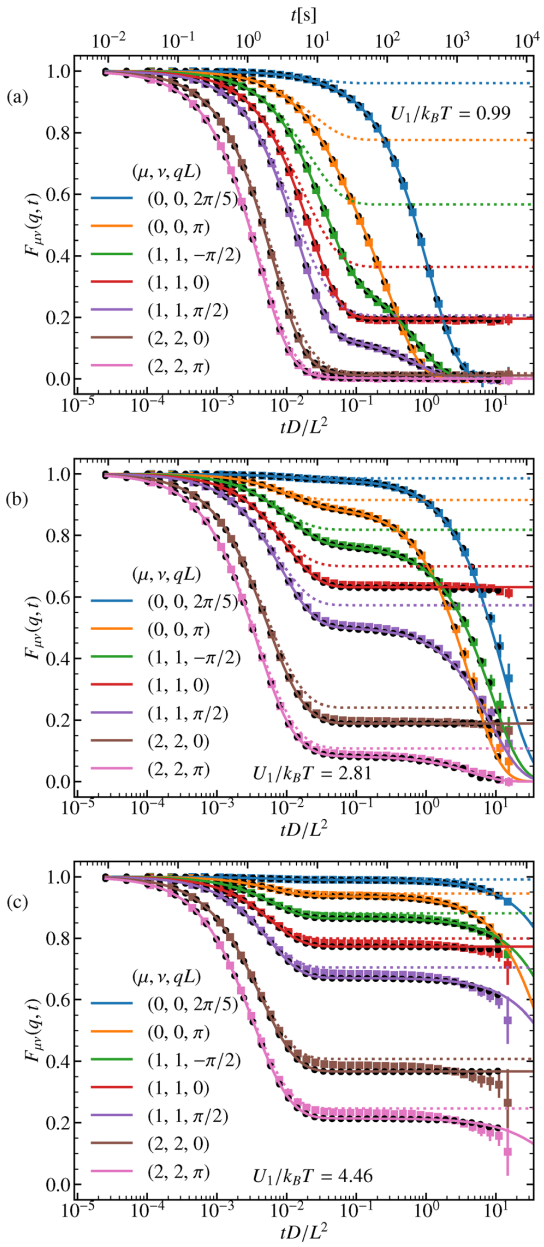

Fig. 3 Diagonal ISF for various mode indices $\mu = \nu$ and wave numbers q and three different amplitudes U_1, (a)–(c). Full colored lines correspond to the theory and colored squares to the experimental results. Black circles represent the simulation results. The dotted lines represent the harmonic approximation.

times. If $|\mu - \nu|$ is odd, the initial value is negative and for even differences the initial value of the ISF is positive, eqn (46). And also according to eqn (48) for odd (or even) values, the long-time limit is negative (or positive, respectively). In contrast to the diagonal elements of the ISF, we find no longer strictly monotone behavior but minima and maxima, see eqn (32).

Results from the experimental data of the off-diagonal ISF closely follow the shape of the analytical predictions and simulation results at long times. However, a clear deviation is observed at short and intermediate times, as shown in Fig. 4. We attribute these discrepancies to experimental factors not implemented in the theoretical model. We consider the primary factor to be the spatial inhomogeneities in the periodicity and amplitude of the light-induced potential across the field of view, which slightly deviates from the ideal cosine form assumed in the theoretical model. As a result, individual particles effectively experience slightly different periodicities and amplitudes across the field of view. A detailed characterization of the amplitude and periodicity in the field of view is shown in Appendix B. Additionally, confinement effects due to the two-dimensional nature of the system and inertial effects not considered in the theoretical framework are factors that might also contribute to these discrepancies. Despite these differences, experimental results for the indices μ and ν with equal $|\mu - \nu|$ collapse into a common intercept (short-time limit), capturing the expected phenomenology from the theoretical predictions given by eqn (46), though with a noticeable shift respect to theory.

Theoretically, each Fourier component of the ISF is defined in terms of a well-defined lattice wavenumber $2\pi/L$. However, in experiments, achieving this level of precision is challenging because of variations in how individual particles interact with the optical field. To allow a more accurate comparison between theory and experiment, a normalization procedure is applied, an approach that is further examined in Fig. 5.

Fig. 5 illustrates the normalized ISF, $F_{\mu\nu}(q,t)/F_{\mu\nu}(q,0)$, for different potential amplitudes U_1/k_BT, three different μ, ν combinations and, for all of them, $qL = \pi$. The choice of $qL = \pi$ is particularly insightful, as it balances, for the measurements time window, sensitivity to both free diffusion and potential-induced localization, providing a clear distinction between different transport regimes. As it can be seen in Fig. 5, after normalization, the agreement between experimental results, the theoretical framework and computer simulations is remarkable, confirming that the model effectively captures full description of the system.

The most striking feature in the off-diagonal elements is the emergence of a maximum at intermediate times, $\tau \ll t \ll \tau_K$ as seen in Fig. 5(b) and (c). For larger times, the curves decay to zero for $q \neq 0$. From the harmonic approximation we anticipate the development of a plateau, whose value can be determined from eqn (77). If $(Q_\mu + q)(Q_\nu + q) < 0$, the plateau corresponds to a maximum, which is nicely approached for large potential amplitudes, see Fig. 5(b) and (c). If $(Q_\mu + q)(Q_\nu + q) > 0$, the curves look similar to the diagonal elements of the ISF, where a simple plateau emerges, see Fig. 5(a). The slowing down of the relaxation towards the plateau or maximum as the potential amplitude grows, is captured as well by $\tau \propto 1/U_1$.

Finally, it is important to emphasize that, although experimental factors cause deviations at short and intermediate times, normalization effectively accounts for these variations,

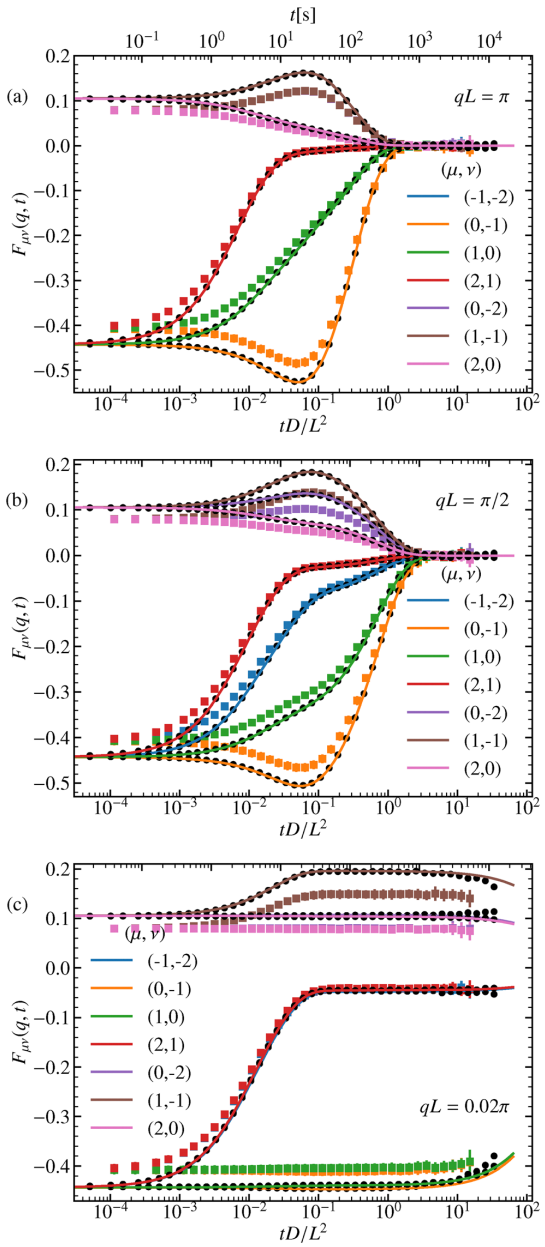

Fig. 4 Off-diagonal ISF for $\nu \neq \mu$ and $U_1 = 0.99 k_B T$ for different mode indices (μ, ν) and wave numbers q, (a)–(c). Full colored lines correspond to the theory and squares to the experimental results. Black circles represent the simulation results. In panel (a) at the edge of the Brillouin zone, $q = \pi/L$, for $(\mu, \nu) = (1, -1)$ and $(0, -2)$ coincide, as well as the ones for $(1, 0)$ and $(-1, -2)$. In panel (c) for wave numbers $q \to 0$ the curves of (μ, ν) and $(-\nu, -\mu)$ approach each other, where $\mu, \nu \in \mathbb{Z}$.

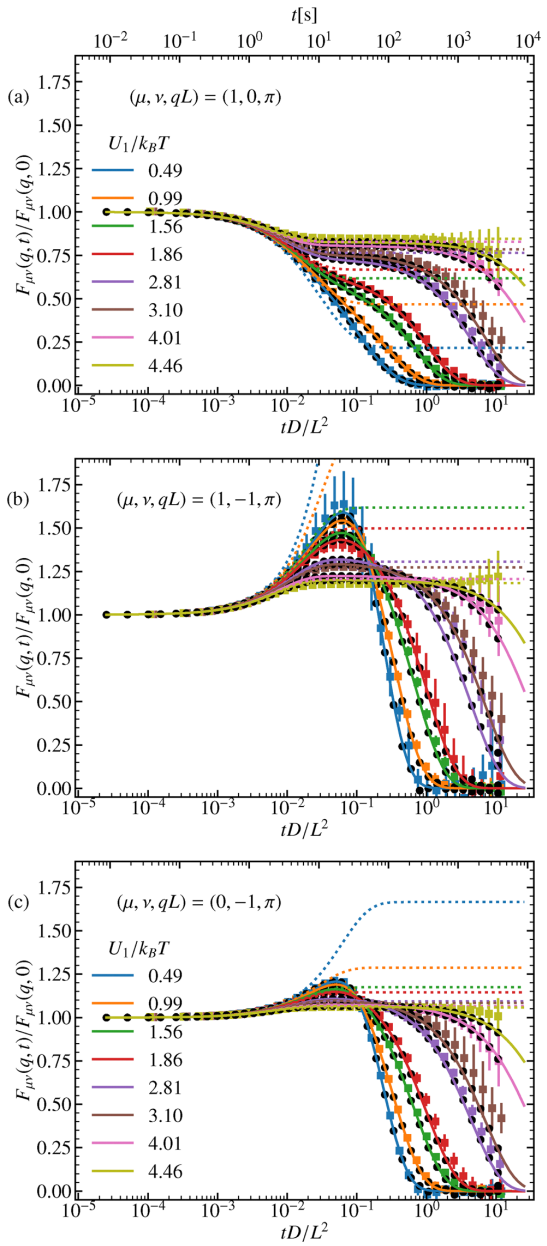

Fig. 5 Off-diagonal ISF for different amplitudes U_1 for wave number $q = \pi$ three different mode indices (μ, ν), (a)–(c). Full colored lines correspond to the theory and squares to the experimental results. Black circles represent the simulation results and dotted lines the harmonic approximation.

leading to excellent agreement between theory, simulations and experiments.

4.3 Low-order moments of $\Delta x(t)$: MSD, diffusivity and non-Gaussian parameter

The dynamics previously discussed in terms of the ISF, can also be found in the standard observables. Therefore, the discussion

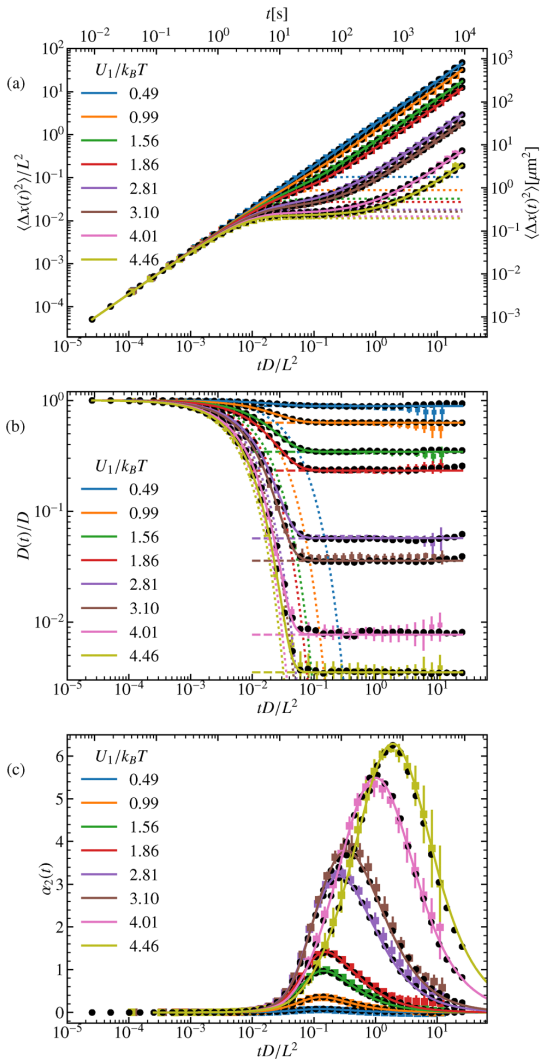

Fig. 6 (a) MSD, (b) time-dependent diffusion coefficient, and (c) non-Gaussian parameter for different potential amplitudes U_1. Full colored lines correspond to the theory and squares to the experimental results. Black circles represent the simulation results and dotted lines the harmonic approximation. The dashed lines in (b) display the theoretical long-term limit.

will be kept rather brief. The MSD, Fig. 6(a), is plotted for various amplitudes U_1 of the external potential. For short times, $t \ll (L^2/4\pi^2D)(k_BT/U_1)$, with $U_1 \gtrsim k_BT$ or for times $t \ll L^2/4\pi^2D$ for very low amplitudes, $U_1 \ll k_BT$, we observe the expected linear increase of the MSD, characteristic of free diffusion. For higher potential barriers, however, a plateau emerges around $t \approx (L^2/4\pi^2D)(k_BT/U_1)$, corresponding to the time scale at which the particle becomes temporarily trapped. At longer times, $\propto \exp(2U_1/k_BT)$, the particle eventually overcomes the barrier and resumes diffusion, with a reduced diffusion constant for higher amplitudes compared to lower ones. This behavior is further highlighted in the time-dependent diffusion coefficient, eqn (51). We find that the long-time diffusion coefficient decreases as U_1 increases, see Fig. 6(b). There we also report good agreement with the known values of the long-time diffusion coefficient. As expected, the harmonic approximation captures the behavior of the relaxation towards the plateau increasingly better for higher amplitudes.

Furthermore, we analyze the non-Gaussianity of the particle displacements using the parameter defined in eqn (53). As expected, for higher barriers, the particle dynamics become increasingly non-Gaussian, see Fig. 6(c). We observe that both very small and very large amplitudes pose challenges in experiments. For small amplitudes, it is difficult to distinguish the dynamics from those of a free particle, as the external potential has little effect. Conversely, for very large amplitudes, the low diffusivity makes it challenging to sample a sufficient number of particles that successfully hop over a barrier within the experimental observation time. However, the experimental results show excellent agreement with both simulations and analytical predictions.

5 Conclusion

In this work, we investigated the dynamics of dilute colloidal suspensions in the presence of a periodic potential. Our approach combined theoretical analysis, Brownian-dynamics simulations, and experimental measurements. By evaluating the spatio-temporal dynamics, we demonstrated that the behavior of a colloid in a periodic potential can be accurately described by analytical solutions of the Smoluchowski equation. This was achieved through the analysis of a generalized ISF, which captures how particle positions are correlated in a periodic system. Low-order moments were derived, with a focus on the MSD, time-dependent diffusion coefficient, and non-Gaussian parameter.

Based on the Smoluchowski equation reformulated in a Hermitian Schrödinger form, we found formal expressions in terms of a spectral-theoretical approach. The eigenfunctions were expressed in Bloch form, to make use of the periodic nature of the system. We found an analytic expression for the generalized ISF, $F_{\mu\nu}(q,t)$. By using the time-dependent perturbation theory and Taylor expansion of the ISF we computed lower-order moments. In our system, without memory effects, the ISF effectively captures the full dynamics of colloidal particles in periodic potentials, revealing both short- and long-time diffusive behavior and trapping at intermediate times.

We performed experiments on 2D dilute colloidal suspensions subjected to a periodic potential generated by two interfering laser beams. Using particle tracking, we obtained particle trajectories and averaged them to extract relevant observables. The laser power was calibrated to its corresponding amplitude value using two theoretical predictions (eqn (48) and (52)). From our experimental data, we extracted the observables of interest and compared them to our analytical solutions and Brownian-dynamics simulations. We compared the results for

various strengths of the amplitude of the potential and found excellent agreement between the theoretical description and experiments. The most sensitive observables were the off-diagonal elements of the generalized ISF, where slight differences in the experimental setup were amplified in the curves. It was crucial to ensure equivalent experimental conditions, minimizing variations in periodicity, potential amplitude, and confinement effects. To obtain good agreement with the analytical predictions, a normalization was necessary.

We have carried out a comprehensive test of the underlying fundamental dynamics of colloidal dynamics in a structured environment, combining theory, simulations, and experiments. By analyzing the generalized ISF, we identified new observables with distinct features, including a non-vanishing long-time limit. We provide a detailed theoretical framework and rationalize our findings through a harmonic approximation. Developing an explicit formula for the whole-time dependence of the ISF allowing for a comprehensive description of colloidal motion across all time scales. Furthermore, we introduced a new approach for calibrating the experiment using these observables, offering a reciprocal space alternative to conventional calibration methods. Comparing the results to a harmonic approximation, we confirm that the Brownian particle first diffuses freely, before it is temporarily trapped in the minima of the periodic cosine potential. For these times the dynamics are well approximated by a harmonic potential for large enough amplitudes, and only at longer times it hops over the potential barriers and once again exhibits diffusive behavior.

The analytical and experimental framework presented can be extended to more complex systems. Although this work focused on dilute suspensions, exploring more dense systems would allow us to study particle interactions and many-body effects. A possible other extension is the study of periodic lattices, where higher-dimensional effects and collective behavior become important. Investigating tilted washboard potentials could provide further insight into driven transport. Our framework is also applicable to a wide range of periodic systems beyond simple cosine potentials. Experimentally, the new observables could also be measured using differential dynamic microscopy.

Author contributions

MAES and TF conceived and administrated the project. YMS, ABZB, and MAES conducted the experimental work. RR and TF performed the analytic modeling. RR implemented the numerical analysis. YMS, MAES, and RR performed computer simulations, analyzed the experimental data, and contributed to data visualization. RR drafted the original manuscript, and all authors contributed to the manuscript.

Data availability

Data for this article, including all particle trajectories analyzed in the manuscript, are available at Zenodo **https://doi.org/10.5281/zenodo.14931759**.

Conflicts of interest

There are no conflicts to declare.

Appendices

A. Calibration

The precise determination of the periodic potential amplitude (U_1/k_BT) as a function of laser power is a fundamental step in experiments involving colloidal particles confined in optical potentials. In this work, we perform both the traditional diffusion-based calibration and a novel approach utilizing the generalized intermediate scattering function (ISF). The conventional approach to calibrating periodic potentials relies on measuring the normalized long-time diffusion coefficient (D_∞/D) as a function of laser power. As shown in the central panel of Fig. 6, the diffusivity of particles decreases as the potential amplitude increases, since energy barriers progressively hinder diffusive motion. For a simple cosine potential, $U(x) = U_1\cos(2\pi x/L)$, the analytical relationship between the normalized diffusion coefficient and the potential amplitude is given by eqn (52).

Our alternative calibration method utilizes the generalized ISF, specifically its asymptotic behavior, which explicitly depends on the potential amplitude. For a simple cosine potential and $q = 0$, the long-time limit of the generalized ISF is analytically described by eqn (48), where the dependence on the potential amplitude, U_1, is evident. Specifically, for $\mu = \nu = 1$, eqn (48) ($F_{11}(0,t)$) evaluates the characteristic wave number imposed on the system by the periodic potential, *i.e.*, $Q_\mu = Q_\nu = 2\pi/L$. In the top panel of Fig. 7 we plot $F_{11}(0,t)$, which exhibits an opposite trend to diffusivity, with higher plateaus as laser power increases. It is important to note that this approach utilizes equilibrium correlation properties instead of transport characteristics, providing complementary insights into the system.

The calibration is performed for both methods by extracting plateau values as a function of laser power and solving eqn (48) and (52) for the diffusivity and generalized ISF methods, respectively. The calibration results from both methods are presented in Fig. 7(b), showing the relationship between laser power and dimensionless potential amplitude U_1/k_BT. The remarkable agreement between these independent approaches validates both the theoretical framework and the experimental implementation, as seen in the central panel of Fig. 6 and 7(a). This strong consistency confirms the theoretical predictions and demonstrates the reliability of this method for calibration purposes.

B. Light-field spatial characterization

This appendix provides a detailed look at the spatial characteristics of the laser-induced periodic potential, as observed through the motion of particles across the experimental field of view. To determine the spatial periodicity, we follow a similar approach as described in ref. 53. However, for the estimation of the amplitude, we used a more direct estimation. Rather than fitting a sine wave to the derivative of the logarithmic particle density, we extracted

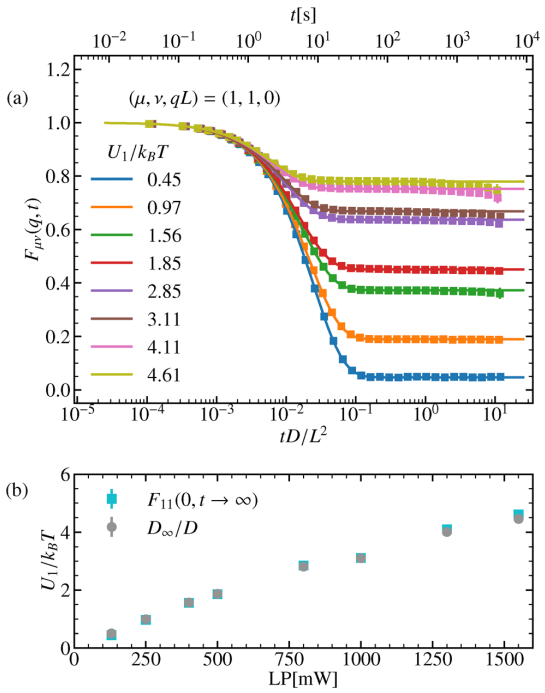

Fig. 7 Panel (a) shows the ISF for the wave numbers $(\mu, \nu, qL) = (1, 1, 0)$ and for different amplitudes U_1. The markers represent experimental results, while the solid lines correspond to analytical predictions, with the amplitudes calibrated to match the experimental data. Panel (b) compares two different calibration methods. One based on the long-time diffusivity D_∞ and the other on the long-time limit of the ISF, $F_{11}(0, t \to \infty)$. The laser powers (LP) used in the experiments, for which the calibration was performed, were 130 mW, 250 mW 400 mW, 500 mW, 800 mW, 1000 mW, 1300 mW, and 1550 mW.

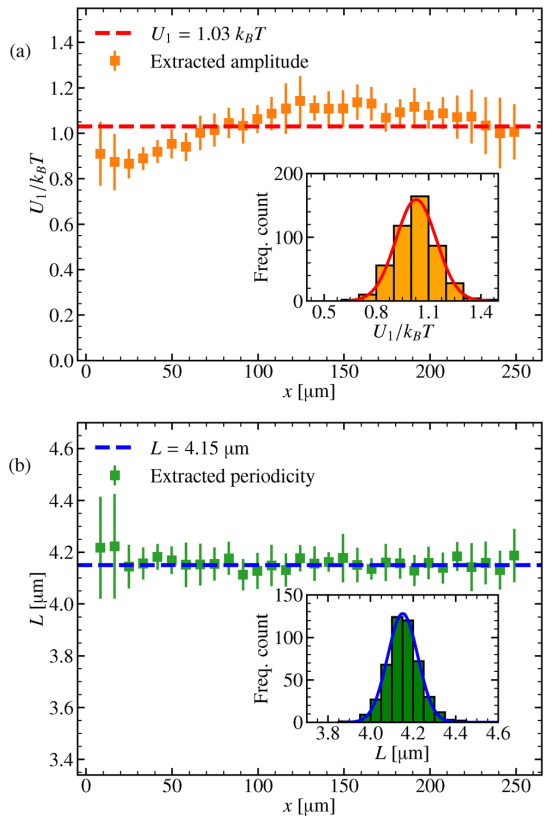

Fig. 8 Panel (a): The spatial variation of the extracted potential amplitude U_1 (orange squares) along the field of view, showing a mean value of $U_1 = 1.03 k_BT$ (red dashed line) with a standard deviation of 0.08 (orange error bar). Inset: Histogram of the extracted amplitude values fitted with a Gaussian distribution (red curve). Panel (b): The spatial variation of the extracted periodicity L (green squares), with a mean value of $L = 4.15$ μm (blue dashed line) with a standard deviation of 0.07 (green error bar). Inset: Histogram of the extracted periodicities fitted with a Gaussian distribution (blue curve).

the amplitude in each window by identifying its maximum and minimum values. The extracted amplitude of the periodic potential as a function of the position along the field of view is shown in Fig. 8(a). The amplitude displays a clear spatial dependence, which arises from the Gaussian envelope of the beam.[6,54,55] The mean amplitude was measured to $U_1 = (1.03 \pm 0.08)\ k_BT$, with a coefficient of variation (CV) of 7.76%. The inset histogram shows the distribution of the measured amplitude values. Fig. 8(b) shows the spatial periodicity of the laser field in the same region. In contrast to the amplitude, the periodicity remains remarkably consistent throughout the field of view, as it is unaffected by the Gaussian beam envelope. It maintains an average value of $L = (4.15 \pm 0.07)$ μm, with a very low CV of 1.68%. The inset histogram confirms this stability by showing a narrow, normally distributed spread of periodicities. The error bars in both figures represent variations between different experimental runs in the same spatial regions.

C. Properties of the Bloch functions

In this appendix, we repeat the argument that the Bloch function $u_{nq}(x)$ to the same wave vector q are orthonormal. Furthermore, we recall some properties of the Bloch functions, in particular, for the case of a symmetric potential.

Orthogonality of Bloch functions. The overlap of two wave function can be simplified using the periodic Bloch functions and splitting the integral in cells

$$\begin{aligned}\langle \Psi_{nq'} | \Psi_{mq} \rangle &= \frac{1}{N}\int_0^{NL} \mathrm{d}x e^{i(q-q')x} u_{nq'}(x)^* u_{mq}(x) \\ &= \frac{1}{N}\sum_{j=0}^{N-1}\int_{jL}^{(j+1)L} \mathrm{d}x e^{i(q-q')x} u_{nq'}(x)^* u_{mq}(x) \\ &= \frac{1}{N}\int_0^{L} \mathrm{d}x e^{i(q-q')x} u_{nq'}(x)^* u_{mq}(x) \sum_{j=0}^{N-1} e^{i(q-q')jL}.\end{aligned} \tag{64}$$

Since

$$\sum_{j=0}^{N-1} e^{i(q-q')jL} = \begin{cases} \dfrac{\exp(iN(q-q')L)-1}{\exp(i(q-q')L)-1} & \text{for } q \neq q' \\ N & \text{else} \end{cases} = N\delta_{qq'} \tag{65}$$

for the discrete wave vectors in the Brillouin zone and because the wave functions are orthonormal $\langle \Psi_{nq'} | \Psi_{mq} \rangle = \delta_{qq'}\delta_{nm}$, Bloch functions to the same wave vector are orthogonal

$$\int_0^L \mathrm{d}x u_{nq}(x)^* u_{mq}(x) = \delta_{nm}.$$

Symmetric band structure. The Hermitian operator $\mathscr{L}_0$ is real. We introduce the eigenfunction $\Psi_\lambda(x)$ to $\mathscr{L}_0\Psi_\lambda(x) = -\lambda\Psi_\lambda(x)$. Taking the complex conjugate of both sides reveals that $\Psi_\lambda(x)^*$ is again eigenfunction to the same eigenvalue. Bloch theorem states that eigenfunctions can be expressed as $\Psi_{nq}(x) = \exp(iqx)u_{nq}(x)$ with $u_{nq}(x)$ periodic. Hence, $u_{n,-q}(x)$ coincides with $u_{nq}(x)^*$ up to a phase factor. Without restriction, the phase factor can be chosen to be real. Therefore, the corresponding band structure is symmetric with respect to flipping the sign of the wave vector, $\lambda_{n,q} = \lambda_{n,-q}$. Furthermore, the eigenfunctions in the center of the Brillouin zone are real $u_{n0}(x) = u_{n0}(x)^*$.

Degeneracies for symmetric potentials. We define the parity operator $\mathbf{P}$ acting on functions $\mathbf{P}\Psi(x) = \Psi(-x)$. For a symmetric potential $\mathbf{P}U(x) = U(-x) = U(x)$ and the parity operator commutes with $\mathscr{L}_0$. Then, with $\Psi_\lambda(x)$ eigenfunction, we find $\lambda\mathbf{P}\Psi(x) = \mathbf{P}\mathscr{L}_0\Psi_\lambda(x) = \mathscr{L}_0\mathbf{P}\Psi_\lambda(x)$. Hence, $\mathbf{P}\Psi_\lambda(x) = \Psi_\lambda(-x)$ is again eigenfunction to the same eigenvalue. For the Bloch representation this implies $u_{nq}(-x) = \pm u_{n,-q}(x)$. In particular for $q = 0$ we find $u_{n0}(x)$ is either even or odd. As a consequence all matrix elements $\langle u_{m0}|\mathscr{L}_0|u_{n0}\rangle$ vanish if the eigenfunctions $u_{m0}(x)$, $u_{n0}(x)$ have different parity. In particular, the avoided crossing theorem does not apply, the eigenvalues at the center of the Brillouin zone can be twofold degenerate.

Peculiarity of the cosine potential. In general, band crossings at the center of the BZ are allowed for symmetric potentials since the avoided crossing theorem does not apply, but usually only some band crossings appear while other bands still avoid each other. The simple cosine potential is special in the sense that all eigenvalues to $q = 0$ are twofold degenerate except for the ground state $\lambda_{00} = 0$.

This property is somewhat hard to see in the representation of the time-evolution operator in the Schrödinger representation in the Fourier basis $\langle\mu|\mathscr{L}_0|\nu\rangle$. However, the property can be easily deduced, omitting the gauge transform in the first place, *i.e.* representing the dynamics in terms of the non-Hermitian matrix

$$\langle\mu|\Omega|\nu\rangle = -\frac{4\pi^2 D}{L^2}\Big[\mu^2\delta_{\mu\nu} + \frac{\mu}{2}\big(\delta_{\mu,\nu+1} - \delta_{\mu,\nu-1}\big)\Big]. \tag{66}$$

This matrix displays the symmetry $\langle -\mu|\Omega|-\nu\rangle = \langle\mu|\Omega|\nu\rangle^*$. The argument now follows the one of Appendix A of ref. 32. The matrix $\langle\mu|\Omega|\nu\rangle$ displays a zero row for $\mu = 0$ and splits into a part with entries for $\mu > 0$, $\nu \geq 0$ and an identical one for $\mu < 0$, $\nu \leq 0$.

The only entries preventing the matrix to split into blocks with positive/negative μ, ν are the matrix elements $\langle\pm1|\Omega|0\rangle$. However, as $\langle l_0| = \langle 0|$ is a left eigenvector to eigenvalue 0, all eigenvectors $|r_{n0}\rangle$ to non-zero eigenvalues have a zero entry in their Fourier representation by orthogonality of eigenvectors $0 = \langle l_{00}|r_{n0}\rangle = \langle 0|r_{n0}\rangle$. Therefore, the blocks with both μ,ν positive do not communicate with the blocks with both indices negative. In particular, one can choose eigenvectors with $\langle\mu|r_n\rangle = 0$ for $\mu \gtrless 0$ or symmetric and antisymmetric eigenfunctions to the twofold degenerate eigenvalue $\lambda_{n0} > 0$.

D. ISF and probability density

Starting with the general definition of the ISF, eqn (33), and inserting the expression for the probability density, eqn (24), we obtain

$$\begin{aligned} F_{\mu\nu}(q,t) &= \int_0^L \mathrm{d}x_0 \int_0^{NL} \mathrm{d}x e^{-i(q+Q_\mu)x} e^{i(q+Q_\nu)x_0} \sqrt{\frac{p^{\mathrm{eq}}(x)}{p^{\mathrm{eq}}(x_0)}} \\ &\quad \times \frac{1}{N}\sum_{q'\in \mathrm{BZ}}\sum_n e^{-\lambda_{nq'}t} e^{iq'(x-x_0)} u_{nq'}(x) u_{nq'}(x_0)^* p^{\mathrm{eq}}(x_0) \\ &= \int_0^L \mathrm{d}x_0 \int_0^{NL} \mathrm{d}x e^{-i(q+Q_\mu)x} e^{i(q+Q_\nu)x_0} \\ &\quad \times \frac{1}{N}\sum_{q'\in \mathrm{BZ}}\sum_n e^{-\lambda_{nq'}t} e^{iq'(x-x_0)} u_{nq'}(x) u_{00}(x)^* u_{nq'}(x_0)^* u_{00}(x_0) \\ &= \sum_n e^{-\lambda_{nq}t}\left[\int_0^L \mathrm{d}x e^{-iQ_\mu x} u_{nq}(x) u_{00}(x)^*\right] \\ &\quad \times \left[\int_0^L \mathrm{d}x_0 e^{-iQ_\nu x_0} u_{nq}(x_0) u_{00}(x_0)^*\right]^*. \end{aligned} \tag{67}$$

Here in the second equality we used that the Bloch function to wave vector zero at the lowest band is related to the equilibrium density $u_{00}(x) = \sqrt{p^{\mathrm{eq}}(x)}$. Furthermore, we observed that the integral vanishes for $q \neq q'$ due to the periodicity of the Bloch functions.

We can make further progress by using the Fourier modes as basis functions, eqn (29). By expanding the Bloch functions we obtain

$$\begin{aligned} \int_0^L \mathrm{d}x e^{-iQ_\mu x_0} u_{nq}(x) u_{00}(x)^* &= \int_0^L \mathrm{d}x e^{-iQ_\mu x} u_{nq}(x_0)\left[\sum_{\sigma\in\mathbb{Z}} \frac{e^{iQ_\sigma x}}{\sqrt{L}}\langle\sigma|u_{00}\rangle\right]^* \\ &= \sum_{\sigma\in\mathbb{Z}} \langle u_{00}|\sigma\rangle \int \frac{\mathrm{d}x}{\sqrt{L}} e^{-iQ_{\mu+\sigma}x} u_{nq}(x) = \sum_{\sigma\in\mathbb{Z}} \langle u_{00}|\sigma\rangle\langle\mu+\sigma|u_{nq}\rangle. \end{aligned} \tag{68}$$

Collecting terms, we find the expression for the ISF

$$F_{\mu\nu}(q,t) = \sum_n e^{-\lambda_{nq}t} \sum_{\sigma,\tau\in\mathbb{Z}} \langle u_{00}|\sigma\rangle\langle\mu+\sigma|u_{nq}\rangle\langle u_{nq}|\nu+\tau\rangle\langle\tau|u_{00}\rangle. \tag{69}$$

This relation is eqn (41) in the main text.

We also derive how the probability density can be obtained from the intermediate scattering function

$$\begin{aligned}
&\frac{1}{NL^2}\sum_{\mu\nu\in\mathbb{Z}}\sum_{q\in\mathrm{BZ}} F_{\mu\nu}(q,t)\mathrm{e}^{i\left(q+Q_\mu\right)x}\mathrm{e}^{-i(q+Q_\nu)x_0}\\
&=\frac{1}{NL^2}\sum_{\mu\nu\in\mathbb{Z}}\sum_{q\in\mathrm{BZ}}\left\langle \mathrm{e}^{-i\left(q+Q_\mu\right)[x(t)-x]}\mathrm{e}^{i(q+Q_\nu)[x(0)-x_0]}\right\rangle\\
&=\frac{1}{NL^2}\sum_{\mu\nu\in\mathbb{Z}}\sum_{q\in\mathrm{BZ}}\sum_{q'\in\mathrm{BZ}}\left\langle \mathrm{e}^{-i\left(q+Q_\mu\right)[x(t)-x]}\mathrm{e}^{i(q'+Q_\nu)[x(0)-x_0]}\right\rangle \qquad (70)\\
&=N\int\frac{\mathrm{d}q}{2\pi}\int\frac{\mathrm{d}q'}{2\pi}\left\langle \mathrm{e}^{-iq[x(t)-x]}\mathrm{e}^{iq'[x(0)-x_0]}\right\rangle\\
&=N\langle\delta[x-x(t)]\delta[x_0-x(0)]\rangle=p^{\mathrm{eq}}(x_0)\mathbb{P}(x,t|x_0).
\end{aligned}$$

This is eqn (34) of the main text.

E. Harmonic approximation

The harmonic approximation of the Langevin equation, eqn (2), is given by

$$\frac{\mathrm{d}}{\mathrm{d}t}\bar{x}(t)=-DuQ_1{}^2\bar{x}(t)+\eta(t), \qquad (71)$$

where the first term on the right-hand side is the restoring force, and the second term is the random force of the Brownian motion. The equation is expressed by the shifted position, $\bar{x} := x - L/2$, so that the potential minimum is at the center. The Smoluchowski equation to solve for the propagator $\mathbb{P} := \mathbb{P}(\bar{x}t|\bar{x}_0)$ is given by

$$\partial_t\mathbb{P}=\frac{\partial}{\partial\bar{x}}\left(DuQ_1{}^2\bar{x}\mathbb{P}\right)+D\frac{\partial^2}{\partial\bar{x}^2}\mathbb{P} \qquad (72)$$

with the harmonic-well relaxation time $\tau = 1/DuQ_1{}^2$. The solution is known as the Ornstein–Uhlenbeck process[36] and we find the propagator

$$\mathbb{P}(\bar{x}t|\bar{x}_0)=\frac{1}{\sqrt{2\pi V(t)}}\exp\left[-\frac{\left(\bar{x}-\bar{x}_0\mathrm{e}^{-t/\tau}\right)^2}{2V(t)}\right], \qquad (73)$$

with $V(t) = D\tau[1 - \exp(-2t/\tau)]$, and the stationary solution as the long-time limit of the propagator

$$p^{\mathrm{eq}}(\bar{x}_0)=\frac{1}{\sqrt{2\pi D\tau}}\mathrm{e}^{-\bar{x}_0{}^2/2D\tau}. \qquad (74)$$

We can readily compute the generalized ISF by using the definition of the main text, eqn (33), and by extending the integrals to infinity

$$\begin{aligned}
F_{\mu\nu}(q,t) &= \int_\infty^\infty\mathrm{d}\bar{x}\int_\infty^\infty\mathrm{d}\bar{x}_0\mathrm{e}^{-i\left(q+Q_\mu\right)(x+L/2)}\mathrm{e}^{i(q+Q_\nu)(x_0+L/2)}\\
&\quad\times\mathbb{P}(\bar{x},t|\bar{x}_0)p^{\mathrm{eq}}(\bar{x}_0).
\end{aligned} \qquad (75)$$

Solving the integrals then yields the ISF

$$\begin{aligned}
F_{\mu\nu}(q,t) &= \exp\Bigg[-\frac{D\tau}{2}\Big[\left(q+Q_\mu\right)^2-2\left(q+Q_\mu\right)(q+Q_\nu)\mathrm{e}^{-\frac{t}{\tau}}\\
&\quad+(q+Q_\nu)^2\Big]-\frac{iL}{2}\left(Q_\mu-Q_\nu\right)\Bigg].
\end{aligned} \qquad (76)$$

We further calculate the ratio

$$\frac{F_{\mu\nu}(q,t\to\infty)}{F_{\mu\nu}(q,t)}=\exp\left[-\frac{k_{\mathrm{B}}T}{U_1Q_1{}^2}\left(q+Q_\mu\right)(q+Q_\nu)\right]. \qquad (77)$$

We also readily find the MSD

$$\begin{aligned}
\left\langle\Delta x(t)^2\right\rangle &= \int_\infty^\infty\mathrm{d}\bar{x}\int_\infty^\infty\mathrm{d}\bar{x}_0(x-x_0)^2\times\mathbb{P}(\bar{x},t|\bar{x}_0)p^{\mathrm{eq}}(\bar{x}_0)\\
&=2D\tau\left(1-\mathrm{e}^{-t/\tau}\right),
\end{aligned} \qquad (78)$$

and time-dependent diffusion coefficient

$$D(t)=D\mathrm{e}^{-t/\tau}. \qquad (79)$$

Acknowledgements

We acknowledge the use of AI (ChatGPT, Grammarly, Language Tool, Perplexity) for its assistance with grammar checking, translations, and text enhancement. This research was funded in part by the Austrian Science Fund (FWF) 10.55776/I5257. For open access purposes, the author has applied a CC BY public copyright license to any author accepted manuscript version arising from this submission. MAES acknowledges funding by Deutsche Forschungsgemeinschaft (DFG) – Project number 459399860 for financial support.

References

1 W. Poon, P. Pusey and H. Lekkerkerker, *Phys. World*, 1996, **9**, 27.
2 F. Q. Potiguar and R. Dickman, *Phys. Rev. E:Stat., Nonlinear, Soft Matter Phys.*, 2007, **76**, 031103.
3 C. Bechinger and E. Frey, *Colloids on Patterned Substrates*, John Wiley and Sons, Ltd, 2007, ch. 3, pp. 87–158.
4 D. Pérez Guerrero, J. Arauz-Lara, E. Sarmiento and G. Guerrero-Garcia, *Front. Phys.*, 2021, **9**, 635269.
5 X.-G. Ma, P.-Y. Lai, B. J. Ackerson and P. Tong, *Soft Matter*, 2015, **11**, 1182–1196.
6 C. Dalle-Ferrier, M. Krüger, R. D. L. Hanes, S. Walta, M. C. Jenkins and S. U. Egelhaaf, *Soft Matter*, 2011, **7**, 2064–2075.
7 R. Castaneda-Priego, *Rev. Mex. Fis.*, 2021, **67**, 050101.
8 A. Ashkin, *Phys. Rev. Lett.*, 1970, **24**, 156.
9 A. Ashkin, *Science*, 1980, **210**, 1081–1088.
10 A. Ashkin, *Proc. Natl. Acad. Sci. U. S. A.*, 1997, **94**, 4853–4860.
11 A. Jonas and P. Zemanek, *Electrophoresis*, 2009, **29**, 4813–4851.

12 D. Gao, W. Ding, M. Nieto-Vesperinas, X. Ding, M. Rahman, T. Zhang, C. Lim and C.-W. Qiu, *Light: Sci. Appl.*, 2017, **6**, e17039.
13 M. C. Jenkins and S. U. Egelhaaf, *J. Phys.: Condens. Matter*, 2008, **20**, 404220.
14 R. Capellmann, A. Khisameeva, F. Platten and S. Egelhaaf, *J. Chem. Phys.*, 2018, **148**, 114903.
15 S. Lifson and J. L. Jackson, *J. Chem. Phys.*, 1962, **36**, 2410–2414.
16 R. Festa and E. G. d'Agliano, *Phys. A*, 1978, **90**, 229–244.
17 R. L. Stratonovich, *Topics in the theory of random noise*, 1967.
18 P. Reimann, C. Van den Broeck, H. Linke, P. Hänggi, J. M. Rubi and A. Pérez-Madrid, *Phys. Rev. E:Stat., Nonlinear, Soft Matter Phys.*, 2002, **65**, 031104.
19 P. Reimann, C. Van den Broeck, H. Linke, P. Hänggi, J. M. Rubi and A. Pérez-Madrid, *Phys. Rev. Lett.*, 2001, **87**, 010602.
20 M. Evstigneev, O. Zvyagolskaya, S. Bleil, R. Eichhorn, C. Bechinger and P. Reimann, *Phys. Rev. E: Stat., Nonlinear, Soft Matter Phys.*, 2008, **77**, 041107.
21 P. Fulde, L. Pietronero, W. R. Schneider and S. Strässler, *Phys. Rev. Lett.*, 1975, **35**, 1776–1779.
22 A. V. Straube and F. Höfling, *J. Phys. A: Math. Theor.*, 2024, **57**, 295003.
23 C. Kurzthaler, S. Leitmann and T. Franosch, *Sci. Rep.*, 2016, **6**, 36702.
24 H. Xu, X. Zheng and X. Shi, *Phys. Rev. Res.*, 2024, **6**, 023014.
25 B. J. Berne and R. Pecora, *Dynamic light scattering: with applications to chemistry, biology, and physics*, Courier Corporation, 2013.
26 J. K. Dhont, *An introduction to dynamics of colloids*, Elsevier, 1996.
27 R. Cerbino and V. Trappe, *Phys. Rev. Lett.*, 2008, **100**, 188102.
28 J. C. Crocker and D. G. Grier, *J. Colloid Interface Sci.*, 1996, **179**, 298–310.
29 C. Kurzthaler, C. Devailly, J. Arlt, T. Franosch, W. C. K. Poon, V. A. Martinez and A. T. Brown, *Phys. Rev. Lett.*, 2018, **121**, 078001.
30 C. Kurzthaler and T. Franosch, *Soft Matter*, 2017, **13**, 6396–6406.
31 O. Chepizhko and T. Franosch, *Phys. Rev. Lett.*, 2022, **129**, 228003.
32 R. Rusch, O. Chepizhko and T. Franosch, *Phys. Rev. E*, 2024, **110**, 054606.
33 D. B. Mayer, E. Sarmiento-Gómez, M. A. Escobedo-Sánchez, J. P. Segovia-Gutiérrez, C. Kurzthaler, S. U. Egelhaaf and T. Franosch, *Phys. Rev. E*, 2021, **104**, 014605.
34 L. Angelani, *Europhys. Lett.*, 2013, **102**, 20004.
35 C. Kurzthaler, Y. Zhao, N. Zhou, J. Schwarz-Linek, C. Devailly, J. Arlt, J.-D. Huang, W. C. K. Poon, T. Franosch, J. Tailleur and V. A. Martinez, *Phys. Rev. Lett.*, 2024, **132**, 038302.
36 H. Risken, *Fokker-Planck equation*, Springer, 1996.
37 A. Lapolla, D. Hartich and A. Godec, *Phys. Rev. Res.*, 2020, **2**, 043084.
38 A. Asaklil, M. M. Mazroui and Y. Boughaleb, *Phys. Condens. Matter*, 1999, **10**, 91–97.
39 A. Pattanayak, A. Shee, D. Chaudhuri and A. Chaudhuri, *New J. Phys.*, 2024, **26**, 083024.
40 G. Maruyama, *Rendiconti del Circolo Matematico di Palermo*, 1955, vol. 4, pp. 48–90.
41 D. Frenkel and B. Smit, *Understanding Molecular Simulation: From Algorithms to Applications*, Academic Press, San Diego, 2nd edn, 2002, vol. 2, pp. 2–5.
42 U. Siems, Dissertation, Universität Konstanz, Constance, 2017.
43 U. Siems and P. Nielaba, *J. Phys.: Conf. Ser.*, 2018, **1012**, 012011.
44 P. Virtanen, R. Gommers, T. E. Oliphant, M. Haberland, T. Reddy, D. Cournapeau, E. Burovski, P. Peterson, W. Weckesser and J. Bright, *et al.*, *Nat. Methods*, 2020, **17**, 261–272.
45 D. Blair and E. Dufresne, *The Matlab Particle Tracking Code Repository*, **https://site.physics.georgetown.edu/matlab/**, visited on 21/01/20.
46 X. Michalet, *Phys. Rev. E:Stat., Nonlinear, Soft Matter Phys.*, 2010, **82**, 041914.
47 J.-P. Hansen and I. R. McDonald, *Theory of simple liquids: with applications to soft matter*, Academic Press, 2013.
48 S. Lang, R. Schilling and T. Franosch, *J. Stat. Mech.: Theory Exp.*, 2013, **2013**, P12007.
49 S. Lang, R. Schilling, V. Krakoviack and T. Franosch, *Phys. Rev. E: Stat., Nonlinear, Soft Matter Phys.*, 2012, **86**, 021502.
50 *NIST Digital Library of Mathematical Functions*, **https://dlmf.nist.gov/**, Release 1.2.3 of 2024-12-15, **https://dlmf.nist.gov/**, ed. F. W. J. Olver, A. B. Olde Daalhuis, D. W. Lozier, B. I. Schneider, R. F. Boisvert, C. W. Clark, B. R. Miller, B. V. Saunders, H. S. Cohl and M. A. McClain.
51 J. Spiechowicz, I. G. Marchenko, P. Hänggi and J. Łuczka, *Entropy*, 2023, **25**(2), 318.
52 A. Rahman, *Phys. Rev.*, 1964, **136**, A405–A411.
53 C. Dieball, Y. Mohebi Satalsari, A. B. Zuccolotto-Bernez, S. U. Egelhaaf, M. A. Escobedo-Sánchez and A. Godec, *Soft Matter*, 2025, 2170–2181.
54 M. C. Jenkins and S. U. Egelhaaf, *J. Phys.: Condens. Matter*, 2008, **20**, 404220.
55 Q.-H. Wei, C. Bechinger, D. Rudhardt and P. Leiderer, *Phys. Rev. Lett.*, 1998, **81**, 2606–2609.

4.2 Precisely controlled colloids: a playground for path-wise non-equilibrium physics

Journal: *Soft Matter*

Reference: Soft Matter, 2025,21, 2170

Impact factor: 2.9

Authors: Cai Dieball, **Yasamin Mohebi Satalsari**, Angel B. Zuccolotto-Bernez, Stefan U. Egelhaaf, Manuel A. Escobedo-Sánchez, and Aljaž Godec.

Author contributions:

AG and SUE conceptualized the project, MAES and AG were responsible for the administration. SUE and AG provided the resources and acquired the funding for the experimental and theoretical work, respectively. CD and AG developed the theory. CD, YM, ABZB and MAES performed the investigations and validation. MAES and CD developed the software. ABZB and YM worked on the experimental setup. YM, CD and MAES worked on the methodology, data curation, and visualization. CD and AG wrote the original draft. CD, AG, ABZB, YM and MAES reviewed and edited the final version of the manuscript.

Soft Matter

PAPER

View Article Online
View Journal | View Issue

Cite this: *Soft Matter*, 2025, **21**, 2170

Precisely controlled colloids: a playground for path-wise non-equilibrium physics

Cai Dieball,[a] Yasamin Mohebi Satalsari,[b] Angel B. Zuccolotto-Bernez,[b] Stefan U. Egelhaaf,[b] Manuel A. Escobedo-Sánchez *[b] and Aljaž Godec *[a]

Received 9th October 2024,
Accepted 9th February 2025

DOI: 10.1039/d4sm01189a

rsc.li/soft-matter-journal

We investigate path-wise observables in experiments on driven colloids in a periodic light field to dissect selected intricate transport features, kinetics, and transition-path time statistics out of thermodynamic equilibrium. These observables directly reflect the properties of individual paths in contrast to the properties of an ensemble of particles, such as radial distribution functions or mean-squared displacements. In particular, we present two distinct albeit equivalent formulations of the underlying stochastic equation of motion, highlight their respective practical relevance, and show how to interchange between them. We discuss conceptually different notions of local velocities and interrogate one- and two-sided first-passage and transition-path time statistics in and out of equilibrium. Our results reiterate how path-wise observables may be employed to systematically assess the quality of experimental data and demonstrate that, given sufficient control and sampling, one may quantitatively verify subtle theoretical predictions.

1 Introduction

Colloidal particles, due to their high susceptibility to external fields, can be precisely manipulated using light,[1–12] electrical and magnetic fields,[1,13–15] or microfluidic devices.[16] This makes them an ideal platform to validate fundamental physical theories of soft matter with a high degree of accuracy. Over the years, substantial effort has been made in colloidal soft matter to explore various aspects of both stochastic dynamics[17–20] and stochastic thermodynamics.[21,22] In fact, colloidal systems have always served as a paradigm for stochastic thermodynamics,[21,22] which generalizes the notion of thermodynamic observables to individual stochastic paths. Many fundamental kinetic and thermodynamic properties have been discovered and verified using colloids, including the statistics of work performed on[23,24] and heat dissipated by[24] a driven colloid, detailed[25] and transient[26] fluctuation theorems, realizations of heat engines,[6,11,12] as well as first-passage[8,27,28] and transition-path time statistics,[29–33] to name a few. Notably, these are properties of individual stochastic paths, so-called functionals, which inherently provide much deeper insight into the underlying dynamics than their ensemble-average counterparts.[34–40]

Despite decades of intensive research leading to numerous significant discoveries, the potential of driven and controlled colloids to reveal fundamental physical laws remains far from exhausted. On the one hand, this may be because advances in abstract theory (*e.g.*, functional fluctuation relations,[39,41,42] speed limits,[43–46] thermodynamic uncertainty relations[45,47–56]) do not so easily proliferate to experiments or require excellent statistics. On the other hand, reciprocal-space-based techniques (*e.g.*, dynamic light scattering, neutron or X-ray scattering, differential dynamic microscopy and variants)[57–60] are only beginning to be considered in the theory of stochastic thermodynamics.[46]

To go beyond the state-of-the-art in particle-tracking analysis we focus on path-wise observables that directly reflect properties of entire individual paths rather than properties of the probability density of an ensemble of particles, such as radial distribution functions or mean-squared displacements. Path-wise refers to those functionals of particular realizations of trajectories that map entire trajectories $(X_\tau)_{0\le\tau\le t}$ or large parts of them to some $f[(X_\tau)_{0\le\tau\le t}]$, as opposed to observables depending only on the value at some fixed set of times, *e.g.*, $f(X_{\tau_1},X_{\tau_2})$. A particular class of insightful path-wise observables is first-passage time,[61,62] which is the stochastic time it takes for a trajectory to reach a prescribed target (position) for the first time, *e.g.*, $f[(X_\tau)_{0\le\tau\le t}] = \arg\min_{0\le\tau\le\infty}(X_\tau = a)$ for a target at a. For example, first-passage time statistics have been shown to provide a deeper understanding of the origin of sub-diffusion than mean-squared displacements.[63] Moreover, they can distinguish processes with equal transition probability densities,[64] unravel the number of intermediate states,[28] and reveal fractal dynamics of colloids.[8] Related, albeit quite different, path-wise observables are transition-path times defined as the stochastic duration of successful transitions, whereby "successful" reflects that the particle does

[a] *Mathematical bioPhysics Group, Max Planck Institute for Multidisciplinary Sciences, 37077 Göttingen, Germany. E-mail: agodec@mpinat.mpg.de*
[b] *Condensed Matter Physics Laboratory, Heinrich Heine University Düsseldorf, 40225, Düsseldorf, Germany. E-mail: escobedo@hhu.de*

not return to its original position before arriving at a predefined target point.[65–68] Under typical conditions, transition-path times obey a surprising symmetry,[65] and violations of this symmetry may be used to gain intriguing insights.[31]

The "inherent" sensitivity of the selected observables is such that they can be systematically used to assess and critically verify the quality of experimental data. In this study, we conduct precise experiments on colloids driven through a periodic light field to investigate fundamental and complex aspects of transport, along with first-passage and transition-path times in out-of-equilibrium conditions. Our results reiterate how given sufficient control and sampling even the most subtle theoretical predictions may be verified quantitatively, which will hopefully reinforce the motivation in the field of experimental soft matter to test and further increase the quality of experimental data.

1.1 Structure of the paper

In the first part, we present two different ways to write the underlying stochastic equation of motion on a trajectory-based level and show how to interchange between the two in theory and practice. We highlight the necessity of knowing both representations by connecting them to essential dynamic and thermodynamic properties. Based on these representations, we discuss conceptually different notions of local velocities, whose interrelations are *a priori* not obvious. Next, we investigate first-passage time statistics for barrier-crossing events and show how these are linked to the local mean velocity (using ref. 69). Finally, we verify (and slightly extend to periodic systems) the transition-path time symmetry predicted in ref. 65,68. All of the aforementioned aspects are confirmed and supported by experimental data on both equilibrium (passive) and driven experiments. We conclude with a perspective on further research directions and open questions.

2 Materials and methods

In this study, the applied potential is periodic in the x-direction and originates from the optical force resulting from the interaction of particles with a periodic light field with period $L = 4.135$ μm.

2.1 Sample preparation

We prepared a dilute colloidal dispersion containing polystyrene Sulfate latex particles of 1.5 μm radius with a polydispersity of 4% (Thermo Fisher Scientific, batch number 1660463). The particles were suspended in ultra-pure water with a resistivity of 18.2 MΩ cm (Purelabs Flex, Elga). The dispersion was confined to quasi-two-dimensional (2D) sample cells, which were assembled as follows: 2.3 μL of the dilute colloidal dispersion was placed on top of a 22 × 50 mm cover slip, then a 22 × 22 mm cover slip was carefully placed on top, and the slides were glued together using UV-curing glue (NOA61, Norland Products Inc.). We mounted the assembled cell on a microscope slide. To avoid the two glasses to get too close to each other (by capillary forces) and pinning the particles, we have used the polydispersity of the sample, *i.e.*, the larger sizes in the dispersion (particles of around 2 μm in radius), as spacers. All sample cells were left to reach equilibrium in a laboratory environment at 20 °C for two days. The area fraction was $\varphi_a \simeq 1\%$.

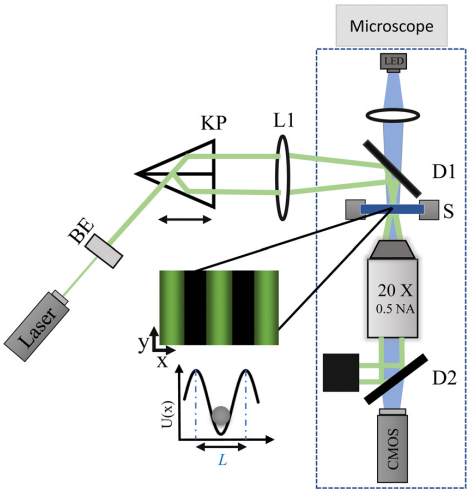

Fig. 1 Schematic representation of the experimental setup. A laser beam is expanded using a beam expander (BE) and directed to a Kösters prism (KP) to create two parallel beams. The laser beams are focused (using L1 and D1) in the sample plane to create the periodic light field. Dichroic mirrors D1 and D2 transmit the LED and reflect the laser wavelength. The sample cell is mounted on a piezo nanopositioner stage (S).

2.2 Experimental setup

In this study, the periodic light field is created by the interference of two laser beams.[70] A laser beam (Cobolt 05-01 Samba 1.5 W) of 532 nm wavelength, is expanded and then split into two parallel beams using a Köster prism. Using a lens and a dichroic mirror the beams are guided to interfere on the microscope sample plane, creating a fringe pattern. The period (L, dark-bright fringe) can be changed by moving the Kösters prism position. The laser beams are removed from the image path (with a dichroic mirror) and a CMOS camera (Mako U-130B) is used as sensor to record images. The sample cell sits on a piezo nanopositioner stage (Mad City Labs, Nano-BioS300), which is used to move the sample. A schematic representation of the experimental setup is shown in Fig. 1. For details on the extraction of the period L and amplitude of the potential, see Appedix A.

2.3 Optical microscopy and particle tracking

All experiments were performed with the colloidal particles under the effect of the periodic light field.

Equilibrium state (not driven). We used an inverted bright-field microscope (Nikon, Ti-E) with a 20× objective (Nikon, Plan Flour, 0.5NA) and a light-emitting diode (Thorlabs M455L4) as an illumination source. The images were recorded with a CMOS camera (Mako U-130B) at a resolution of 1280× 1024 pixels

utilizing the full field of view of the camera. The pixel pitch was 0.24 μm px^{-1}. The data acquisition was performed at 25 frames per second and an exposure time of 1 ms, with 90 000 images per measurement. This corresponds to a total measurement duration of 1 hour. We conducted several experiments that reached a total collection of 1224 trajectories. We used modified MATLAB-based particle tracking routines based on those of D. Blair and E. Dufresne[71] to accurately determine the position of the colloids. Additionally, by following the Michalet algorithm,[72] we estimated the localization uncertainty to be ±2 nm. For a direct comparison to the driven state experiments, we treated the 1224 trajectories as 2448 trajectories with a duration of 30 minutes each.

Driven state. We used a piezo nanopositioner stage to apply a driving force to the colloids by dragging the sample cell through the potential. The stage was programmed to move 139 μm in 65 500 steps, with a 40 ms pause between each step. Optimizing these values allowed us to drag the sample cell at a controlled velocity of $v_0 = (0.053 \pm 0.002)$ μm s^{-1}. We recorded images at 25 frames per second, each measurement containing 45 000 images, for a total measurement time of 30 minutes. In total, we acquired 1168 trajectories.

3 Overdamped Langevin dynamics in a periodic drift field

3.1 Equilibrium dynamics

The dynamics of colloidal particles are generically overdamped on the observed scales.[17] Thus, we consider the stochastic dynamics in one-dimensional space of a colloidal particle with position X_t connected to a thermal bath with temperature T, governed by the overdamped Langevin equation

$$\mathrm{d}X_t = -\frac{D}{k_\mathrm{B}T}\,\partial_x U(X_t)\mathrm{d}t + \sqrt{2D}\mathrm{d}W_t, \qquad (1)$$

where k_B denotes the Boltzmann constant, $D \propto T$ is the diffusion constant, $\mathrm{d}W_t$ is the increment of the fluctuating thermal force (Wiener process), and $U(x)$ is a potential, with units of energy. The force arising from the potential is $-\partial_x U(x)$ which results in the drift field $-D\partial_x U(x)/k_\mathrm{B}T$ (*i.e.*, the fluctuation–dissipation theorem yields the mobility $\mu \equiv D/k_\mathrm{B}T$). On the level of probability densities of particle positions, the dynamics in eqn (1) is described by the Fokker–Planck equation[73,74] $\partial_t p(x,t) = -\partial_x\{[-D\partial_x U(x)/k_\mathrm{B}T - D\partial_x]p(x,t)\}$. However, we mainly use eqn (1) to stay closer to the path-wise description.

As mentioned in Section 2, in this study, the potential $U(x)$ is periodic in the x-direction with a period L. An experimental trajectory is shown in Fig. 2. Note that the motion in the y-direction will only correspond to a free Brownian motion, as there is no force coming from $U(x)$ in this direction. The latter is illustrated in Fig. 2(a) where the effect of $U(x)$ constrains the movement in the x-direction, contrary to the y-direction where it is allowed to move freely.

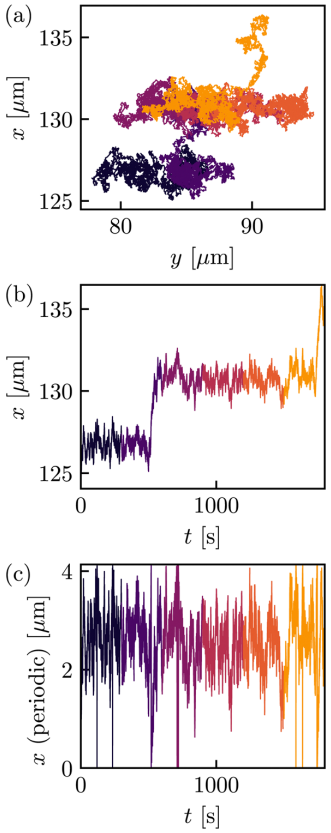

Fig. 2 Exemplary trajectory (a), and corresponding projection onto the x-axis (b) and (c) where time runs from dark to bright. (c) The period is always chosen as L = 4.135 μm. The dataset comprises 2448 such trajectories.

In Fig. 2(b) and (c), we therefore focus on X_t, where in (c) we show x_t which is defined as X_t projected onto a single period $[0,L)$, *i.e.*, $x_t \equiv X_t \bmod L$. Accordingly, for $U(x) = U(x+L)$ we may view eqn (1) as L-periodic dynamics for x_t, *i.e.*, $\mathrm{d}x_t = -D\partial_x U(x_t)\mathrm{d}t/k_\mathrm{B}T + \sqrt{2D}\mathrm{d}W_t$ with the definition $x_{t+\mathrm{d}t} \equiv (x_t + \mathrm{d}x_t) \bmod L$ ensuring that x_t remains confined to $[0,L)$.

If projected on $[0,L)$, the system settles into a Boltzmann equilibrium density $p_\mathrm{eq}(x) \propto \exp(-U(x)/k_\mathrm{B}T)$.[73]

More generally, not all systems settle into equilibrium steady states. For sufficiently confined systems and drifts without an explicit time dependence, a steady state is approached for $t \to \infty$. Similarly, for space-periodic dynamics treated as if they evolve in a single period, *i.e.*, projected onto a single period, a steady state is approached for long times, assuming no explicit time dependence in the drift and diffusion. However, here, a stationary current emerges if the system is driven out of equilibrium by a non-conservative drift; see below.

3.2 Driven dynamics

While equilibrium dynamics are interesting and important, they are relatively well understood. However, they do not apply

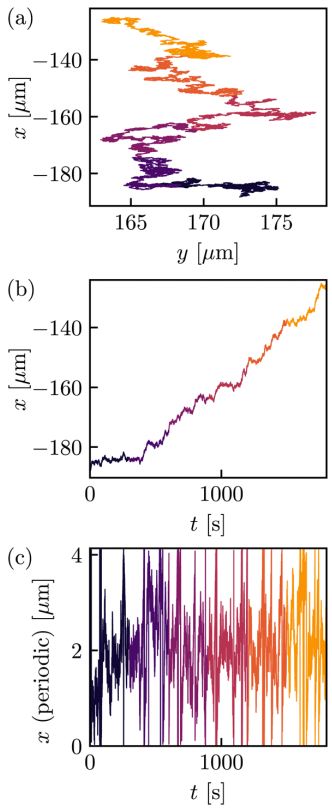

Fig. 3 Example of a trajectory that is driven by v_0, see eqn (2), (a), and corresponding projection onto the x-axis (b) and (c) where time runs from dark to bright. (c) The period is always chosen as L = 4.135 μm. The dataset comprises 1168 such trajectories.

to irreversible (*e.g.*, living) systems since these are inherently out of equilibrium, *e.g.*, driven by non-conservative flows (*i.e.*, shear) or ATP hydrolysis. Note that the theory presented here is not new but is simply presented in a comprehensive manner and in a potentially new logical order to stay close to the experiment. To address driven dynamics, we consider the simplest situation in which we add a constant bare velocity v_0 in the x-direction to the Langevin eqn (1), yielding

$$\mathrm{d}x_t = \left[-\frac{D}{k_\mathrm{B}T}\partial_x U(x_t) + v_0\right]\mathrm{d}t + \sqrt{2D}\mathrm{d}W_t. \qquad (2)$$

In the experiments, v_0 is introduced by dragging the sample cell with a constant velocity $-v_0$ along the periodic direction of $U(x)$ using the piezo nanopositioner stage. For a sample trajectory in this driven setting, see Fig. 3. Note that, as before, the motion in the x- and y-directions decouples and that the motion in the y-directions remains equilibrium Brownian motion only, see Fig. 3(a).

What can we say about the driven dynamics? First, the dynamics projected onto a single period, see Fig. 3(c), still settles into a steady state—a non-equilibrium steady state (NESS)—with density $p_\mathrm{s}(x)$, which, however, no longer has a Boltzmann form. Instead, the shape of $p_\mathrm{s}(x)$ is skewed in the direction of sign (v_0).

The first question that arises is, given eqn (2), what is $p_\mathrm{s}(x)$ for a given bare velocity $v_0 \neq 0$? The second question refers to the movement (*i.e.*, probability current) of the driven particle; see Fig. 3(b). This question is non-trivial, and compared to the bare velocity v_0, the particle is expected to slow down by the barriers of $U(x)$. Thus, one naturally wonders what theoretical velocity is implied by the equation of motion in eqn (2).

Both questions can be answered by rewriting eqn (2) into an alternative form

$$\mathrm{d}x_t = \left[D\partial_x \ln p_\mathrm{s}(x_t) + \frac{j_\mathrm{s}}{p_\mathrm{s}(x_t)}\right]\mathrm{d}t + \sqrt{2D}\mathrm{d}W_t. \qquad (3)$$

In the following subsection, we will show how to derive it. First, we will discuss the properties and usefulness of this rewriting. Here, j_s is the steady-state probability current and $\nu_\mathrm{s}(x) \equiv j_\mathrm{s}/p_\mathrm{s}(x)$ is the "local mean velocity".[22] The latter has to fulfill $\partial_x[\nu_\mathrm{s}(x)p_\mathrm{s}(x)] = 0$ to ensure that $p_\mathrm{s}(x)$ is indeed the steady state density, which is seen by requiring that $\partial_t p(x,t) = 0$ for $p(x,t) = p_\mathrm{s}(x)$, where $p(x,t)$ is the probability density goverend by the Fokker–Planck equation,[73,74]

$$\begin{aligned}\partial_t p(x,t) &= -\partial_x\{[-D\partial_x U(x)/k_\mathrm{B}T + v_0 - D\partial_x]p(x,t)\}\\ &= -\partial_x\{[D\partial_x \ln p(x,t) + \nu(x,t) - D\partial_x]p(x,t)\}\\ &= -\partial_x[\nu(x,t)p(x,t)]. \qquad (4)\end{aligned}$$

In one-dimensional space, this directly implies that there is a constant probability current j_s with $\nu_\mathrm{s}(x) = j_\mathrm{s}/p_\mathrm{s}(x)$. For equilibrium dynamics $v_0 = 0, j_\mathrm{s} = 0$, and thus both presentations eqn (2) and (3) agree, since for the equilibrium density $p_\mathrm{eq}(x)$ we have $\partial_x \ln p_\mathrm{eq}(x) = -\partial_x U(x)/k_\mathrm{B}T$. Thus, both can be seen as a direct extension of eqn (1).

Eqn (3) is particularly insightful when considering microscopic reversibility (*i.e.*, detailed balance) and its generalizations. Namely, if we let $G^{\nu_\mathrm{s}}(x,t|x_0)$ denote the two-point conditional probability density of x_t (which is the Green's function of the Fokker–Planck eqn (4), *i.e.*, $\partial_t G^{\nu_\mathrm{s}} = -\partial_x[-D\partial_x \ln p_\mathrm{s}(x) + \nu_\mathrm{s}(x)]G^{\nu_\mathrm{s}}$ with $G^{\nu_\mathrm{s}}(x,0|x_0) = \delta(x - x_0)$), then detailed balance corresponds to

$$G^0(x,t|x_0)p_\mathrm{s}(x_0) = G^0(x_0,t|x)p_\mathrm{s}(x). \qquad (5)$$

This indeed holds if and only if $\nu_\mathrm{s}(x) = 0$ (*i.e.*, $j_\mathrm{s} = 0$). In contrast, the generalization of eqn (5)–the so-called "dual reversal" symmetry-corresponds to[40]

$$G^{\nu_\mathrm{s}}(x,t|x_0)p_\mathrm{s}(x_0) = G^{-\nu_\mathrm{s}}(x_0,t|x)p_\mathrm{s}(x). \qquad (6)$$

Note that the dual reversal symmetry eqn (6) and symmetries of dynamical functionals of x_t (see ref. 40) are only applicable to the steady-state local mean velocity $\nu_\mathrm{s}(x)$ in eqn (3) but not to the bare velocity v_0 in eqn (2). On the other hand, the potential $U(x)$ that enters thermodynamic potentials only appears in the

first form (2). The main difference between the representations eqn (2) and (3) is that the additional term $\nu_s(x) = j_s/p_s(x)$ (unlike v_0) does not alter the steady-state density $p_s(x)$, irrespective of the value of the constant steady-state current j_s.

When discussing the velocity of the driven system, we must note that $\dot{x}_t$ does not exist in a mathematical sense for overdamped motion as in eqn (2) and (3) [technically $\mathrm{Prob}(|\dot{x}_t| < C) = 0$ for all $C < \infty$] and that there are, in fact, different notions of velocity. The bare velocity v_0 and the drift velocity $v_{\mathrm{drift}}(x)$ (where $\langle\cdot|x_\tau = x\rangle$ denotes the average conditioned on $x_\tau = x$ for any $\tau \in [0,t]$),

$$\frac{\langle \mathrm{d}x_\tau | x_\tau = x\rangle}{\mathrm{d}t} = v_{\mathrm{drift}}(x) \equiv D\partial_x \ln p_s(x) + \nu_s(x) = -\partial_x U(x)/k_B T + v_0, \tag{7}$$

are directly accessible from eqn (2). In contrast to v_0 and $v_{\mathrm{drift}}(x)$, the local mean velocity $\nu_s(x)$ and the mean velocity $\bar{\nu}$,

$$\bar{\nu} \equiv \frac{\langle \mathrm{d}x_\tau\rangle_s}{\mathrm{d}\tau} = \int_0^L \mathrm{d}x[D\partial_x \ln p_s(x) + \nu_s(x)]p_s(x) = \int_0^L \mathrm{d}x[D\partial_x p_s(x) + j_s] = Lj_s, \tag{8}$$

[where $\langle\cdot\rangle_s$ denotes the expectation over paths generated by eqn (2) evolving from $p_s(x_0)$], are obtained from the second form of the equation of motion (3). Note that for initial conditions other than $p_s(x_0)$, a mean velocity defined as $\langle \mathrm{d}x_\tau\rangle/\mathrm{d}\tau$ would not be constant in time but only relaxes towards the above $\bar{\nu}$ as $t \to \infty$. Moreover, note that for a periodic $U(x)$ (with known period L), the mean velocity is equivalently characterized by the following expressions (recall that X_τ is the full dynamics and $x_\tau \equiv X_\tau \bmod L$),

$$\bar{\nu} \equiv \frac{\langle \mathrm{d}x_\tau\rangle_s}{\mathrm{d}\tau} = \langle v_{\mathrm{drift}}(x_\tau)\rangle_s = \langle \nu_s(x_\tau)\rangle_s = Lj_s = \frac{\langle X_{t_2} - X_{t_1}\rangle_s}{t_2 - t_1} = \frac{L}{\langle \tau(x \to x + L)\rangle_s}, \tag{9}$$

for any times t_1, t_2 and for any x, and we used $\langle \partial_x \ln p_s(x_\tau)\rangle_s = \int_0^L \frac{\partial_x p_s(x)}{p_s(x)} p_s(x)\mathrm{d}x = p_s(L) - p_s(0) = 0$ to show $\langle v_{\mathrm{drift}}(x_\tau)\rangle_s = \langle \nu_s(x_\tau)\rangle_s$ as well as $\langle X_{t_2} - X_{t_1}\rangle_s = \left\langle \int_{\tau=t_1}^{\tau=t_2} 1 \circ \mathrm{d}X_\tau \right\rangle_s = \int_0^t \mathrm{d}\tau \int_0^L \mathrm{d}x 1 j_s = tLj_s$ (see, *e.g.*, ref. 40 for details). The term $\tau(x \to x + L)$ in eqn (9) denotes the first-passage time from x to $x + L$, *i.e.*, the (stochastic) time that a trajectory $(X_\tau)_{0\le\tau\le t}$ starting at position x takes to reach position $x + L$ for the first time, see also Fig. 7. The last equality in eqn (9) is shown in ref. 69 and will be revisited later in this work. Before we demonstrate and verify the different notions of velocities from the experimental data, we first need to find a way to swap between the representations, that is, from eqn (2) to eqn (3) and *vice versa*.

3.3 Swapping representations: From eqn (2) to eqn (3)

On a general note, we emphasize that determining eqn (3) analytically in a high-dimensional space is generally *not* feasible (*i.e.*, it requires solving the stationary Fokker–Planck equation $\partial_t p(x,t) = 0$; in practice, one would need to simulate long trajectories and estimate $p_s(x)$ as histograms). However, in the given one-dimensional scenario with constant bare velocity v_0 there is a way to obtain $p_s(x)$ and, consequently, eqn (3) from eqn (2), see ref. 73, which we follow here.

Define the auxiliary function $\psi(x)$ (here 0 is the left side of the periodic interval, and $x \in [0,L]$) as

$$\psi(x) \equiv \exp\left[\frac{1}{D}\int_0^x v_{\mathrm{drift}}(x')\mathrm{d}x'\right] = \exp\left[\frac{U(0) - U(x)}{k_B T} + \frac{v_0 x}{D}\right]. \tag{10}$$

The result for $p_s(x)$ is

$$p_s(x) = p_s(0)\psi(x)(1 - r(x)[1 - \psi(L)^{-1}]), \tag{11}$$

where we introduced

$$r(x) \equiv \frac{\int_0^x \psi(x')^{-1}\mathrm{d}x'}{\int_0^L \psi(x')^{-1}\mathrm{d}x'} \in [0,1] \quad \text{for } x \in [0,L], \qquad p_s(0) = \left[\int_0^L \psi(x)\left(1 - r(x)\left[1 - \frac{1}{\psi(L)}\right]\right)\mathrm{d}x\right]^{-1}. \tag{12}$$

As a consistency check, we note that for $v_0 = 0$ we should recover the Boltzmann distribution, and indeed we find

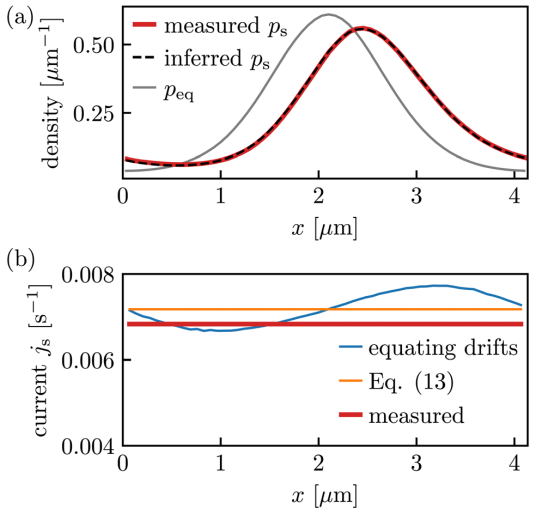

Fig. 4 (a) $p_s(x)$ in eqn (11) inferred from equilibrium (passive) experiments and using the value $v_0 = 0.053$ μm s^{-1} of the experimentally fixed velocity, where we deduced $U(x)/k_BT$ up to a constant offset from $\ln p_{eq}$, where p_{eq} was estimated as a histogram of the equilibrium dynamics with 60 bins in $[0,L)$ (setting a limited spatial resolution for the rest of the analysis). Note that for our experimental setting, U is technically known but involves a convolution with a Bessel function[75,76] and is prone to experimental inaccuracies. We thus prefer to infer U directly from the equilibrium data. The diffusion coefficient $D = 0.04$ μm^2 s^{-1} was fitted from $\mathrm{var}(\mathrm{d}x_\tau)/2\mathrm{d}\tau$ averaged over $[0,t]$ and over all trajectories, see eqn (14). The equilibrium density p_{eq} is only shown for comparison and we stress that it, as expected, does not agree with $p_s(x)$. (b) Probability current inferred from the equilibrium data using the value $v_0 = 0.053$ μm s^{-1} of the experimentally prescribed velocity as described in eqn (13) and below. The comparison to the measured value in the driven data, see eqn (15), shows slight deviations.

$\psi(x) = \exp([U(0) - U(x)]/k_BT)$ such that $\psi(L) = e^0 = 1$ and $p_s(x)/p_s(0) = \psi(x)$ provides it. Additionally, in Fig. 4(a), we also verify eqn (3) as its resulting p_s (dashed line) overlaps with the p_s measured from a histogram of the driven dynamics (red line) with experimental data.

To obtain the representation in eqn (3) in full, we are also required to fit the constant $j_s = \nu_s(x)p_s(x)$. This may be done either from

$$j_s = Dp_s(0)\frac{\psi(0)^{-1} - \psi(L)^{-1}}{\int_0^L \psi(x')^{-1}\mathrm{d}x'}, \tag{13}$$

or by equating $-D\partial_x U(x)/k_BT + v_0$ in eqn (2) with $D\partial_x \ln p_s(x) + \frac{j_s}{p_s(x)}$ in eqn (3). With p_s and j_s (eqn (11) and (13)) we can finally transform eqn (2) into eqn (3), as done for the experimental data in Fig. 4. We stress again that this transformation was only analytically feasible since we deal with a one-dimensional system and a constant bare velocity v_0. While the inferred density $p_s(x)$ in Fig. 4(a) fits the measurement very well, there are slight deviations between the current j_s in Fig. 4(b) inferred from the equilibrium measurements using the input value of v_0 (orange line) compared to the driven measurement (red line) or to inferring the current by equating the drifts in eqn (2) and (3) using the input v_0 and $p_{eq}(x)$ and $p_s(x)$ as in Fig. 4(a) (blue line in Fig. 4(b); note that the blue line should, in principle, be constant). We speculate that the deviations may be due to very slight imperfections in the periodicity L that become amplified since the field of view comprises many periods (about $60L$, see Fig. 10 in the appendix).

3.4 Swapping representations: from eqn (3) to eqn (2)

For completeness, we also consider the reversed mapping, where we measure the driven data and want to infer the underlying potential $U(x)$ and bare velocity v_0. Note that this is only possible if we know that the driving arises purely from a constant drift velocity v_0, and we can only infer $U(x)$ up to a constant. Knowing $U(x)$ is very relevant for stochastic thermodynamics (*i.e.*, for determining free energy, internal energy, and work, but not the heat and entropy production or the dynamics). In the present case, transforming in the reverse direction mainly serves as a consistency check.

As for $p_{eq}(x)$ in the equilibrium setting before, we estimate $p_s(x)$ from an ensemble of NESS trajectories as a histogram with 60 bins, and the diffusion coefficient D from the short-time fluctuations

$$D = \frac{1}{t}\int_0^t \mathrm{d}\tau \frac{\langle \mathrm{d}x_\tau^2\rangle_s}{2\mathrm{d}\tau} = \frac{1}{2t}\int_0^t \langle \mathrm{d}x_\tau^2\rangle_s. \tag{14}$$

It turns out (at least from our trajectories length) that the easiest and most reliable way to obtain j_s from NESS trajectories appears to be to use [see eqn (9)]

$$j_s = \frac{\langle X_t - X_0\rangle_s}{Lt}, \tag{15}$$

which together with $p_s(x)$ yields the form (3). To transform into eqn (2) we compute the bare velocity v_0 [comparing eqn (2) and (3); note that $U(x)$ is not yet known at this point, but it drops out upon integration] as

$$\begin{aligned} v_0 &= \frac{1}{L}\int_0^L \mathrm{d}x \left[D\partial_x \ln p_s(x) + \frac{j_s}{p_s(x)} - D\partial_x U(x)/k_BT\right] \\ &= \frac{1}{L}\int_0^L \mathrm{d}x \nu_s(x) = \frac{j_s}{L}\int_0^L \mathrm{d}x \frac{1}{p_s(x)}. \end{aligned} \tag{16}$$

Now, we can obtain the potential (up to an additive constant) from its derivative [obtained by equating drift terms in eqn (2) and (3)]

$$\partial_x U(x) = -\frac{k_BT}{D}\left[\frac{D\partial_x p_s(x) + j_s}{p_s(x)} - v_0\right]. \tag{17}$$

This way, one can transform back from eqn (3) to eqn (2). In practice, this allows us to check whether the driving v_0 introduced in the experiment is what we expected (*i.e.*, it serves as another consistency check in addition to Fig. 4). The potential $U(x)$ [we set the additive constant to zero, *i.e.*, we chose $\min U(x) = 0$] and v_0 computed this way are compared to the measured equilibrium (*i.e.*, $v_0 = 0$) and the results are shown in Fig. 5. As before, we observed slight deviations in velocity and current, probably connected to slightly washed-out barriers over the large field of view in the experiment (a tiny error in

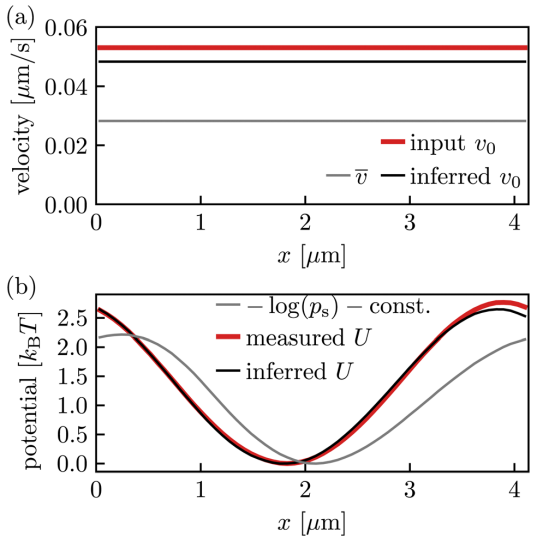

Fig. 5 (a) Inferred v_0 from driven experimental data compared to the desired input value v_0. Though there are some statistical deviations in the values for v_0 (related to Fig. 4(b)), both obtained values for v_0 are well distinguishable from the mean velocity $\bar{v}$ (grey line). (b) The potential $U(x)$ inferred from the driven data *via* eqn (17) (black line) matches the potential measured from the equilibrium data projected on one period $[0,L)$ using $U(x) = -\ln(p_{eq}(x)) - \text{const.}$ (red line) quite well. The barrier height (difference between minimum and maximum) is $2.76k_BT$ in the red line and $2.65k_BT$ in the black line, respectively. It deviates from $-\log(p_s)$ (grey line) since the driven data set does not obey a Boltzmann density [see eqn (2) and (3)].

the value of L can become relevant when projecting on $[0,L)$ *via* $x_\tau = X_t \bmod L$ since the range of X_τ comprises a range of about $60L$, see Fig. 10 in the Appendix. However, in general the consistency check gives excellent results.

4 Different notions of velocity

To provide more insight into the different notions of velocity in our system, we compute the bare velocity ν_0, the drift velocity $v_{\mathrm{drift}}(x)$ in eqn (7), and the mean velocity $\bar{v} = \langle X_t - X_0\rangle_s/t$ in eqn (9) from the measured trajectories of the driven system. The results are shown in Fig. 6.

As mentioned above, two constants constitute a notion of velocity: the bare velocity ν_0 and the mean velocity $\bar{v}$, see eqn (9). In addition, there are also local, x-dependent notions like the local mean velocity $\nu_s(x)$, as well as the drift velocity $v_{\mathrm{drift}}(x) = \langle \mathrm{d}x_t | x_t = x\rangle/\mathrm{d}t$, see eqn (7). In equilibrium, only the drift velocity $v_{\mathrm{drift}}(x)$ deviates from 0. The mean velocity $\bar{v}$ can be computed in different ways; see eqn (9), some of which are also equivalent from a practical/numerical point of view (depending on how we choose to infer j_s). Note that generally, $\nu_s(x) \neq \langle \nu_s(x_t)\rangle_s \neq v_{\mathrm{drift}}(x) \neq \langle v_{\mathrm{drift}}(x_t)\rangle_s$, that is, the different kinds of velocities indeed have a quite strikingly different meaning, which must be taken into account when characterizing and comparing transport properties.

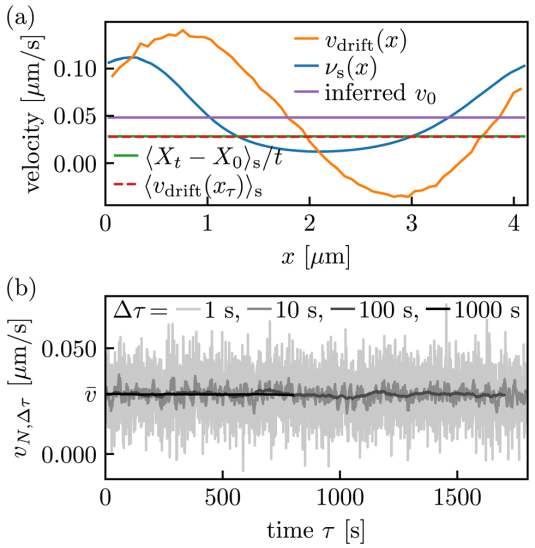

Fig. 6 (a) Different space-dependent and constant velocities in the NESS. See eqn (9) for different representations of the mean velocity $\bar{v}$. In equilibrium, only $\nu_{\mathrm{drift}}(x)$ deviates from zero. Quantities denoted by averages over x_τ are independent of τ in the steady state and are here, for practical reasons to improve statistics, averaged over all $\tau \in [0,t]$. (b) While $\bar{v} = \langle x_{\tau+\Delta\tau} - x_\tau\rangle_s/\Delta\tau$ for all τ and $\Delta\tau$, see eqn (9), the approximation $\bar{v}_{N,\Delta\tau}(\tau) = \frac{1}{N}\sum_{i=1}^{N}(x^i_{\tau+\Delta\tau} - x^i_\tau)/\Delta\tau$ of this quantity over the finite number of trajectories $N = 1168$ as a function of τ, as expected, exhibits large fluctuations for small $\Delta\tau$.

5 First-passage times

In this section, we evaluate the mean first-passage times, that is, the average time it takes for a particle to reach a certain point [see Fig. 7; in our case, the average time to cross the barrier in the potential $U(x)$] for the first time given some initial condition,[61] using experimental data. The first-passage time for barrier crossing is an insightful observable, important, for instance, in the study of chemical reactions kinetics.[77] Perhaps more important in the present context, first-passage observables are generally much more sensitive dynamics indicators than propagators, currents, or mean-squared particle displacement.[8,63,64] As such, they are particularly suitable for critically assessing whether inferred properties of the dynamics (*e.g.*, the parameters in the equations of motion) are appropriate. In particular, first-passage observables may distinguish between processes with identical transition probability densities,[64] and, in contrast to mean-squared particle displacements, provide insight into the microscopic origin of anomalous dispersion in complex media.[8,63]

Here we focus on two particular first-passage observables, namely the mean-first passage to transverse a distance equal to the period length L, $\langle \tau(x \to x + L)\rangle$ and the two-sided mean exit time from the interval $[x - L, x + L]$, $\langle \tau_E(x \pm L)\rangle$. Note that we do not consider periodic boundary conditions here, *i.e.*, we consider trajectories $(X_\tau)_{0\le\tau\le t}$ which evolve on the entire space and not only on $[0,L)$. The chosen first-passage observables have two advantages. First, for a periodic potential $U(x)$, they are independent of the initial position x,[69] making them very practical to infer from experimental data. Second, the mean of its

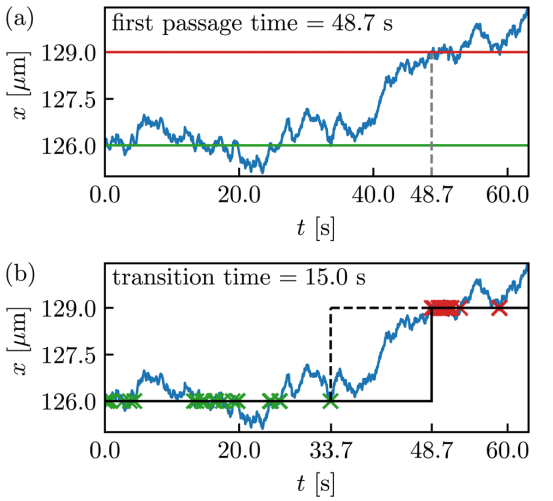

Fig. 7 Pictorial definition of the first-passage time (a) and transition time (b) to go from $x = 126$ μm to $x = 129$ μm. (a) For the trajectory starting at $x = 126$ μm at $t = 0$ s, the first time it reaches $x = 126$ μm is after 46.7 s which is the value of the first-passage time for this trajectory snippet. (b) A transition time from $x = A$ to $x = B$ (will be considered in Section 6; here $A = 126$ μm and $B = 129$ μm) is the time from hitting A for the last time before reaching B. In this example one transition $A \to B$ happens, which takes 15.0 s.

one-sided version, $\langle\tau(x \to x+L)\rangle_s$ is directly related to the mean velocity $\langle\tau(x \to x+L)\rangle_s = L/\bar{v}$, see eqn (9).

To recapitulate where the independence comes from, consider $\tau(0 \to L)$ and $\tau(x \to x+L)$ for some $x \in [0,L]$. Since we have one-dimensional trajectories, x is necessarily crossed in the transition $0 \to L$, and by the renewal theorem[78,79] (note that we are dealing with a time-homogeneous Markov process with continuous paths) we immediately have statistical equality on the level of τ for $\tau(0 \to L) = \tau(0 \to x) + \tau(x \to L)$. Moreover, by periodicity we obtain $\tau(0 \to x) + \tau(x \to L) = \tau(L \to x+L) + \tau(x \to L) = \tau(x \to L) + \tau(L \to x+L) = \tau(x \to x+L)$, therefore $\tau(x \to x+L)$ (and therefore $\langle\tau(x \to x+L)\rangle$) is independent of x, and similarly for $\tau_E(x \pm L)$. We will exploit this in the notation and drop the dependence on x, *i.e.*, $\langle\tau(x \to x+L)\rangle \to \langle\tau(L)\rangle$.

The x-invariance helps to check the data for short-time bias due to under-sampling (see Appendix of ref. 8). Namely, whenever we infer τ from finite trajectories, say of duration t, starting at an arbitrary point x_0, we estimate a conditional mean first-passage/exit time, $\langle\tau(L)|\tau(L)<t\rangle$,[8] *i.e.*,

$$\langle\tau(L)|\tau(L)<t\rangle \equiv \frac{\int_0^t \tau\mathscr{P}_L(\tau)\mathrm{d}\tau}{\int_0^t \mathscr{P}_L(\tau)\mathrm{d}\tau}, \tag{18}$$

where $\mathscr{P}_L(\tau)$ is the probability density of $\tau(L)$, and the same holds for the two-sided exit time $\langle\tau_E(L)|\tau_E(L)<t\rangle$. Obviously, $\lim_{t\to\infty}\langle\tau(L)|\tau(L)<t\rangle = \langle\tau(L)\rangle$. For a periodic $U(x)$ in the equilibrium setting $\nu_0 = 0$, $\langle\tau(L)\rangle$ unlike the exit time $\langle\tau_E(L)\rangle < \infty$ is infinite, $\langle\tau(L)\rangle = \infty$ since the particle can escape to $-\infty$ and thereby may *not* reach the target at any finite time. However, by the fundamental property of Brownian motion, in the equilibrium setting all trajectories eventually hit the target. Moreover, in the driven setting, we consider a bias towards the target, such that almost all trajectories reach the target in a finite time. Hence, we expect $\langle\tau(L)\rangle_s < \infty$[61] (this would, of course, not be the case of a particle biased away from the target).

Any substantial deviations between the conditional and unconditioned first-passage (and exit times, respectively) reflect that a significant fraction of trajectories did not yet cross the barrier to the right of the initial condition and that the estimated mean first-passage time is statistically unreliable. The manifestation of this short-time bias in the equilibrium and driven setting is demonstrated in Fig. 8, where we mimic the effect of a progressively larger measurement time t in the experiment by disregarding long-time data. We find substantial effects of a finite duration of trajectories. In the equilibrium case, both the mean first-passage and the exit time increase with the duration t of trajectories, while in the driven case, the mean first-passage time is progressively approaching the predicted value. Based on the Langevin dynamics in eqn (2) or (3), the one-sided mean first-passage time (blue line) is known to diverge as $t \to \infty$ in the equilibrium setting [see, *e.g.*, $\bar{v} \to 0$ in eqn (9)], while the two-sided version (orange line) must converge. In the non-equilibrium setting (green line), the mean first-passage time must converge, and we observe a quantitative agreement with the theoretical prediction $L/\bar{v}$ in eqn (9) (grey line), where the

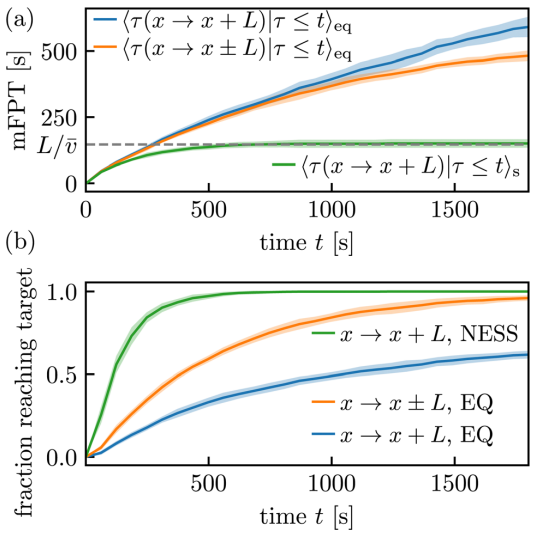

Fig. 8 (a) Conditional mean first-passage times (mFPT) and (b) fraction of trajectories where the barrier crossing event was realized conditioned on times until t (*i.e.*, we cut the data at time t to mimic shorter measurements). The green line approaches 148.8 s, which roughly agrees with the grey line at 146.4 s, confirming the last equality in eqn (9). Shaded regions show the sample standard deviation over the 11 (equilibrium "EQ") or 13 (NESS) data sets.

equality $\langle\tau(L)\rangle_s = L/\bar{v}$ is approached for large t. If the deviation of the green and grey dashed line in Fig. 8(a), does not (approximately) vanish. We could immediately infer that the measurement time is too short. Equivalently, the fraction of successful trajectories (see Fig. 8(b)) ought to converge to 1 for the exit from the interval and generally for the driven setting (and asymptotically approach 1 for the one-sided first-passage in the equilibrium setting) if we are to infer a reliable estimate for $\langle\tau(L)\rangle$. However, note that the additional test with the mean velocity $\bar{v}$ may still be meaningful even if the fraction is already one (*e.g.*, if one has a limited number of trajectories available or if one puts in the requirement of crossing the barrier as an additional condition).

Note that a short-time bias is, in fact, typical. Specifically, whenever not (almost) all observed trajectories reach the target, the estimated mean first-passage time (or its inverse, the rate) will suffer from this bias. This occurs because the first-passage and the exit time are controlled (essentially dominated) by the long-time behaviour of $\mathscr{P}(\tau)$.[61,80,81]

6 Symmetry of transition-path times

An essential and closely related, but fundamentally quite different, concept to first-passage times is transition-path times.[65–68,82] The transition-path time $\mathscr{T}(A \to B)$ from a point A to a point B in (here considered in one-dimensional space) is defined as the time span between the last time that a trajectory $(x_\tau)_{\tau \ge 0}$ hits A before hitting B for the first time, see Fig. 7(b). This observable is deeply related to the concept of mile-stoning

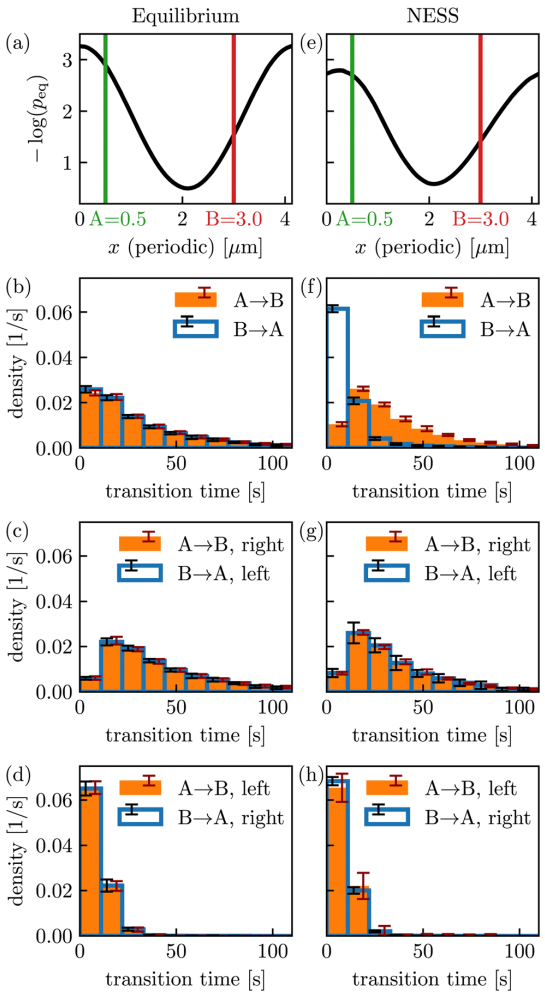

Fig. 9 (a) Periodic potential for the equilibrium data and chosen milestones A and B. (b) Probability of transition times for $A \to B$ and $B \to A$, respectively. Error bars show the sample standard deviation over the different data sets. (c) and (d) As in (b) but resolving for the direction of transitions. For both $A \to B$ and $B \to A$, about 70% of the transitions belong to panel (c) and 30% to panel (d). Since the histograms in (c) and (d) contribute to $A \to B$ and $B \to A$ with equal weights, the symmetry also holds in (b). (e)–(h) As in (a)–(d) but for the driven data. The black line in (e) is now only a *pseudo* potential. The symmetry of (g) and (h) does not imply symmetry in (f) since the weights of (g) and (h) are 96% and 4% for $A \to B$, and 12% and 88% for $B \to A$, respectively.

(see, *e.g.*, ref. 68,83–86) and Fig. 7(b), (where the crosses indicate hits of the milestones). The important difference to first-passage times $\tau(A \to B)$ is thus that the transition time $\mathscr{T}(A \to B)$ does not contain the dwell time around A (see, *e.g.*, ref. 68 for details). A practical difference for our analysis is that we had 0 or 1 samples per trajectory for the first-passage time (since we always started at $t = 0$) while a single trajectory may contain several transitions $A \to B$ and $B \to A$, see Fig. 7. Moreover, we again consider the periodicity in space for the transition times.

Transition-path times encode subtle and important information about violations of the Markov property[31,67,68] and are essential for consistent thermodynamics of non-Markovian processes.[31,68,85,86] A particularly subtle, and at first glance surprising, property of transition-path times is the forward–backward symmetry for reversible Markov dynamics discovered in ref. 65 (for extensions, see ref. 32,68,87,88). It states that for a Markov process obeying detailed balance, we have the equality in time-distribution of transition paths, $p(\mathscr{T}(A \to B)) = p(\mathscr{T}(B \to A))$. The surprising aspect is that if A is located in a potential minimum and B on a potential barrier, the duration of transition paths "uphill'" and "downhill" are statistically identical for any potential. Note that this symmetry does not hold for first-passage times (since the dwell times in A and B can be arbitrarily different).

The transition-path time symmetry has seemingly not yet been experimentally verified (although its violations in multidimensional non-equilibrium systems have already been observed experimentally[31] and by computer simulations[88]). Here we evaluate the transition times between two milestones (here points) A and B (see Fig. 9(a) and (e)) and evaluate frequency histograms of transition-path times as an estimator of their probability density for equilibrium (see Fig. 9(a)–(d)) and NESS dynamics (see Fig. 9(e)–(h)). Note that since the original transition-path time symmetry does not concern periodic systems, it only holds for transitions $A \to B$ and $B \to A$ either passing through the middle (around $x = 2$ μm) or passing through the periodic boundary ($x = 0$ μm), see overlap of blue and orange in Fig. 9(c) and (d), respectively. Note that the symmetry is equally expected to hold in one-dimensional NESS,[87] as confirmed in Fig. 9(g) and (h) (it only breaks down in multidimensional NESS, see ref. 31). Nevertheless, we see in Fig. 9(b) that the symmetry also holds for "mixed'" transitions between A and B, *i.e.*, if we consider all transitions indifferent to whether they do or do not make use of the periodic boundary. This is generally the case for periodic equilibrium dynamics (given 1d Markov) since orange and blue in Fig. 9(b) are a weighted average of orange and blue in Fig. 9(c) and (d) where both colours are weighted with the same proportions [different weights cannot occur in equilibrium since this would lead to a contraction as it implies directed motion ($j_s \neq 0$)]. The symmetry is violated for mixed transitions in Fig. 9(f), since the weighting of Fig. 9(g) and (h) to obtain Fig. 9(f) is *not* the same for orange and blue.

To summarize, Fig. 9 demonstrates the validity of the predicted transition-path time symmetry between two milestones (Fig. 9(c), (d), (g) and (h)). While the transition-path time symmetry does not apply to periodic NESS dynamics (Fig. 9(f)), it holds true (in addition to the "unmixed" transitions in Fig. 9(c), (d), (g) and (h)) for periodic equilibrium dynamics (Fig. 9(b)).

7 Conclusions

We interrogated path-wise properties of driven colloids in a periodic light field to experimentally demonstrate some highly intricate and insightful features of transport, kinetics, and

transition-path time statistics out of equilibrium. Our main goal was to emphasize how these observables can be systematically utilized to critically assess and verify the quality of the experimental data. We have reiterated that, with sufficient control and sampling, even subtle theoretical predictions can be rigorously tested and quantitatively validated. We hope this will motivate the experimental soft-matter community to undertake such tests and further enhance the quality of experimental data.

Beyond the previous analyses of first-passage observables in experimental data[8,28] we compared the mean particle velocity with the corresponding first-passage result[69] to check for short-time biases in non-equilibrium steady states. Despite the measurement time being long enough for trajectories to equilibrate within one period $[0,L)$, we illustrate that observables, such as the one-sided mean first-passage time in equilibrium, (have not yet converged, highlighting the intricate features of first-passage times and more generally, path-based observables). That is, small statistical fluctuations (*i.e.*, small error bars) do not necessarily imply a sufficient quality of data as exemplified by the short-time biases in Fig. 8. From a practical perspective, our results show that first-passage analysis can be used to systematically test experimental data for short-time biases.

Moreover, we verify and extend predicted symmetries for the more subtle transition-path times. By showing that the symmetry persists in effectively one-dimensional non-equilibrium systems, we underscore the usefulness of violations of the transition-path-time symmetry to infer simultaneously broken time-reversal symmetry and the presence of multiple transition pathways.[31,87]

We also highlighted two well-established but distinct, yet mathematically equivalent, formulations of the Langevin equation of motion for colloidal particles. Notably, the second formulation, while less commonly employed in experiments, provides a more thermodynamically expressive framework. We hope this will encourage further integration between soft-matter experiments and stochastic thermodynamics, particularly in advancing thermodynamic inference using speed limits and thermodynamic uncertainty relations.

Author contributions

AG and SUE conceptualized the project, MAES and AG were responsible for the administration. SUE and AG provided the resources and acquired the funding for the experimental and theoretical work, respectively. CD and AG developed the theory. CD, YM, ABZB and MAES performed the investigations and validation. MAES and CD developed the software. ABZB and YM worked on the experimental setup. YM, CD and MAES worked on the methodology, data curation, and visualization. CD and AG wrote the original draft. CD, AG, ABZB, YM and MAES reviewed and edited the final version of the manuscript.

Data availability

Data for this article, including all particle trajectories analyzed in the manuscript, are available at Zenodo at **https://doi.org/10.5281/zenodo.13908799**.

Conflicts of interest

There are no conflicts to declare.

Appendix

Details on the periodic potential

For the above analysis, we determined period L by comparing histograms for $x_\tau \equiv X_\tau \bmod L$ over the left and right half, respectively, of particles in the field of view. The chosen value correct value of L was optimized such that the two histograms optimally agree. While this does not rely on any assumptions about the exact shape of the potential (the shape was only later inferred from histograms; we only assumed that there is one barrier per period to remove ambiguity, since any L-periodic system is, *e.g.*, also $2L$-periodic), this procedure may generally only serve as a fine-tuning for the value for L. Therefore, we here also present an alternative, more systematic, approach to infer L using an approximation for the shape of $U(x)$. Moreover, while the theory and inference of $U(x)$ in the main part of the paper address general periodic potentials, the experimentally realized $U(x)$ is well approximated by a cosine. To elaborate on the discussion of the inference of $U(x)$, and to show the spatial variation that is not investigated in the paper (since it is lost after projecting onto one period; as done, *e.g.*, to arrive at Fig. 5(b)), in this Appendix we also show a complementary approach, where we assume a cosine-shape and infer the amplitude and its spatial variation. Following earlier experiments with comparable setups, we assume that the effective potential induced by the periodic light field can be well approximated by,[2,70] $U(x) = U_0\cos(kx) + U_{\mathrm{bg}}$, with $k = 2\pi/L$, U_0 the potential amplitude and U_{bg} a constant background contribution. The potential background U_{bg} becomes irrelevant as it is neglected by the derivative in eqn (1). Over the whole field of view, particle density profiles $\rho(x)$ for the equilibrium trajectories were analyzed to extract the periodicity and amplitude of an underlying potential *via* $\rho(x) \propto \exp[-U(x)/k_{\mathrm{B}}T]$. The natural logarithm of the density, $\ln(\rho(x))$, was evaluated, and its derivative, $\frac{\mathrm{d}}{\mathrm{d}x}\ln(\rho(x))$, to remove any background contributions. We used a sinusoidal function to fit the derivative for a window consisting of two periods and performed the same analysis for the entire dataset, covering 30 windows. Averaging the results across all windows we estimate the periodicity and potential amplitude of the light field. The insets in Fig. 10 show histograms of the periodicity and amplitude values, with the frequency count plotted *versus* the extracted periodicity and amplitude for all measurements. The red curve represents a Gaussian fit to the histogram. This allows for a statistical summary with the mean and standard deviation extracted from the fit, and in particular shows the spatial variation. The error bars in the plot represent the standard deviation of the extracted periodicity values within each window. The results of the inference of L in Fig. 10(a), based on approximating U as a cosine, are in excellent agreement with the value $L = 4.135$ μm chosen in the main part by matching histograms in different

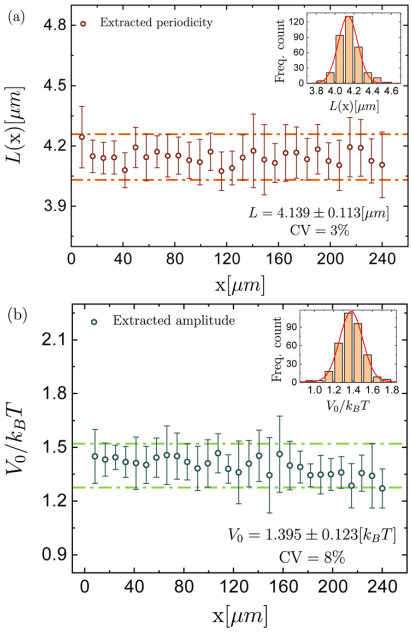

Fig. 10 (a) Extracted periodicity $L(x)$ as a function of position x with error bars representing the standard deviation of $L(x)$ within each window. The dashed lines indicate the average value of the periodicity (L = 4.139 μm) plus and minus one standard deviation (±0.113 μm). The inset shows the histogram of the $L(x)$ values across all windows, with a Gaussian fit illustrating the distribution. The coefficient of variation (CV) is 3%. (b) Extracted potential amplitude V_0/k_BT with error bars showing the standard deviation within each window. The dashed lines represent the average amplitude (V_0 = 1.395k_BT) plus and minus one standard deviation (±0.123k_BT). The inset displays the histogram of values across all windows, fitted with a Gaussian distribution. The coefficient of variation is 8%.

parts in the field of view without assuming the shape of $U(x)$. Moreover, the amplitude inferred in Fig. 10(b) match closely with the barrier heights of 2.76k_BT and 2.65k_BT in Fig. 5(b), keeping in mind that the barrier (difference of maximum and minimum) in the cosine potential is $2V_0$.

Acknowledgements

Financial support from the European Research Council (ERC) under the European Unions Horizon Europe research and innovation program (grant agreement no. 101086182 to AG) and from the Deutsche Forschungsgemeinschaft (DFG), project number 459399860 (to SUE and MAES), is gratefully acknowledged. This work is dedicated to the memory of our friend, mentor and colleague, Stefan U. Egelhaaf. Open Access funding provided by the Max Planck Society.

Notes and references

1 H. Löwen, *J. Phys.: Condens. Matter*, 2008, **20**, 404201.
2 F. Evers, R. D. L. Hanes, C. Zunke, R. F. Capellmann, J. Bewerunge, C. Dalle-Ferrier, M. C. Jenkins, I. Ladadwa, A. Heuer and R. Castañeda-Priego, *et al.*, *Eur. Phys. J.-Spec. Top.*, 2013, **222**, 2995.
3 G. Volpe, G. Volpe and S. Gigan, *Sci. Rep.*, 2014, **4**, 3936.
4 A. Ashkin, *Proc. Natl. Acad. Sci. U. S. A.*, 1997, **94**, 4853.
5 D. G. Grier, *Nature*, 2003, **424**, 810.
6 I. A. Martínez, É. Roldán, L. Dinis, D. Petrov, J. M. R. Parrondo and R. A. Rica, *Nat. Phys.*, 2015, **12**, 67.
7 A. Militaru, A. Lasanta, M. Frimmer, L. L. Bonilla, L. Novotny and R. A. Rica, *Phys. Rev. Lett.*, 2021, **127**, 130603.
8 C. Zunke, J. Bewerunge, F. Platten, S. U. Egelhaaf and A. Godec, *Sci. Adv.*, 2022, **8**, eabk0627.
9 S. A. M. Loos, S. Monter, F. Ginot and C. Bechinger, *Phys. Rev. X*, 2024, **14**, 021032.
10 M. Ibáñez, C. Dieball, A. Lasanta, A. Godec and R. A. Rica, *Nat. Phys.*, 2024, **20**, 135.
11 I. A. Martínez, E. Roldán, L. Dinis and R. A. Rica, *Soft Matter*, 2017, **13**, 22.
12 V. Blickle and C. Bechinger, *Nat. Phys.*, 2011, **8**, 143.
13 N. Osterman, I. Poberaj, J. Dobnikar, D. Frenkel, P. Ziherl and D. Babic, *Phys. Rev. Lett.*, 2009, **103**, 228301.
14 R. M. Erb, H. S. Son, B. Samanta, V. M. Rotello and B. B. Yellen, *Nature*, 2009, **457**, 999.
15 A. Yethiraj, *Soft Matter*, 2007, **3**, 1099.
16 A. Terray, J. Oakey and D. W. M. Marr, *Science*, 2002, **296**, 1841.
17 J. K. G. Dhont, *An introduction to dynamics of colloids*, Elsevier, 1996.
18 A. J. Banchio, J. Bergenholtz and G. Nägele, *Phys. Rev. Lett.*, 1999, **82**, 1792–1795.
19 H. Löwen, *Dynamical Density Functional Theory for Brownian Dynamics of Colloidal Particles*, Springer, Singapore, 2016, pp. 255–284.
20 R. Wittkowski and H. Löwen, *Mol. Phys.*, 2011, **109**, 2935–2943.
21 K. Sekimoto, *Stochastic Energetics*, Springer, Berlin Heidelberg, 2010.
22 U. Seifert, *Rep. Prog. Phys.*, 2012, **75**, 126001.
23 G. M. Wang, E. M. Sevick, E. Mittag, D. J. Searles and D. J. Evans, *Phys. Rev. Lett.*, 2002, **89**, 050601.
24 A. Imparato, L. Peliti, G. Pesce, G. Rusciano and A. Sasso, *Phys. Rev. E: Stat., Nonlinear, Soft Matter Phys.*, 2007, **76**, 050101.
25 G. M. Wang, J. C. Reid, D. M. Carberry, D. R. M. Williams, E. M. Sevick and D. J. Evans, *Phys. Rev. E: Stat., Nonlinear, Soft Matter Phys.*, 2005, **71**, 046142.
26 D. M. Carberry, J. C. Reid, G. M. Wang, E. M. Sevick, D. J. Searles and D. J. Evans, *Phys. Rev. Lett.*, 2004, **92**, 140601.
27 A. Magazzù, A. Callegari, J. P. Staforelli, A. Gambassi, S. Dietrich and G. Volpe, *Soft Matter*, 2019, **15**, 2152–2162.
28 A. L. Thorneywork, J. Gladrow, Y. Qing, M. Rico-Pasto, F. Ritort, H. Bayley, A. B. Kolomeisky and U. F. Keyser, *Sci. Adv.*, 2020, **6**, eaaz4642.
29 N. Zijlstra, D. Nettels, R. Satija, D. E. Makarov and B. Schuler, *Phys. Rev. Lett.*, 2020, **125**, 146001.

30 K. Neupane, D. B. Ritchie, H. Yu, D. A. N. Foster, F. Wang and M. T. Woodside, *Phys. Rev. Lett.*, 2012, **109**, 068102.
31 J. Gladrow, M. Ribezzi-Crivellari, F. Ritort and U. F. Keyser, *Nat. Commun.*, 2019, **10**, 55.
32 R. Satija, A. M. Berezhkovskii and D. E. Makarov, *Proc. Natl. Acad. Sci. U. S. A.*, 2020, **117**, 27116–27123.
33 F. Sturzenegger, F. Zosel, E. D. Holmstrom, K. J. Buholzer, D. E. Makarov, D. Nettels and B. Schuler, *Nat. Commun.*, 2018, **9**, 4708.
34 S. N. Majumdar and A. Comtet, *Phys. Rev. Lett.*, 2002, **89**, 060601.
35 G. Bel and E. Barkai, *Phys. Rev. Lett.*, 2005, **94**, 240602.
36 A. Rebenshtok and E. Barkai, *J. Stat. Phys.*, 2008, **133**, 565.
37 S. Sabhapandit, S. N. Majumdar and A. Comtet, *Phys. Rev. E: Stat., Nonlinear, Soft Matter Phys.*, 2006, **73**, 051102.
38 A. Lapolla, D. Hartich and A. Godec, *Phys. Rev. Res.*, 2020, **2**, 043084.
39 C. Dieball and A. Godec, *Phys. Rev. Lett.*, 2022, **129**, 140601.
40 C. Dieball and A. Godec, *Phys. Rev. Res.*, 2022, **4**, 033243.
41 M. Baiesi, C. Maes and B. Wynants, *Phys. Rev. Lett.*, 2009, **103**, 010602.
42 A. Dechant and S.-i Sasa, *Proc. Natl. Acad. Sci. U. S. A.*, 2020, **117**, 6430.
43 N. Shiraishi, K. Funo and K. Saito, *Phys. Rev. Lett.*, 2018, **121**, 070601.
44 V. T. Vo, T. Van Vu and Y. Hasegawa, *Phys. Rev. E*, 2020, **102**, 062132.
45 T. Van Vu and K. Saito, *Phys. Rev. X*, 2023, **13**, 011013.
46 C. Dieball and A. Godec, *Phys. Rev. Lett.*, 2024, **133**, 067101.
47 A. C. Barato and U. Seifert, *Phys. Rev. Lett.*, 2015, **114**, 158101.
48 J. M. Horowitz and T. R. Gingrich, *Nat. Phys.*, 2019, **16**, 15.
49 K. Macieszczak, K. Brandner and J. P. Garrahan, *Phys. Rev. Lett.*, 2018, **121**, 130601.
50 T. Koyuk and U. Seifert, *Phys. Rev. Lett.*, 2019, **122**, 230601.
51 T. Koyuk and U. Seifert, *Phys. Rev. Lett.*, 2020, **125**, 260604.
52 A. Dechant and S.-i Sasa, *Phys. Rev. X*, 2021, **11**, 041061.
53 G. Falasco and M. Esposito, *Phys. Rev. Lett.*, 2020, **125**, 120604.
54 R.-S. Fu and T. R. Gingrich, *Phys. Rev. E*, 2022, **106**, 024128.
55 T. Koyuk and U. Seifert, *Phys. Rev. Lett.*, 2022, **129**, 210603.
56 C. Dieball and A. Godec, *Phys. Rev. Lett.*, 2023, **130**, 087101.
57 R. Cerbino and V. Trappe, *Phys. Rev. Lett.*, 2008, **100**, 188102.
58 M. A. Kamal, M. Brizioli, T. Zinn, T. Narayanan, R. Cerbino, F. Giavazzi and A. Pal, *J. Colloid Interface Sci.*, 2024, **660**, 314–320.
59 F. Giavazzi and R. Cerbino, *J. Opt.*, 2014, **16**, 083001.
60 M. A. Escobedo-Sánchez, J. P. Segovia-Gutiérrez, A. B. Zuccolotto-Bernez, J. Hansen, C. C. Marciniak, K. Sachowsky, F. Platten and S. U. Egelhaaf, *Soft Matter*, 2018, **14**, 7016–7025.
61 S. Redner, *A Guide to First-Passage Processes*, Cambridge University Press, 2001.
62 R. Metzler, G. Oshanin and S. Redner, *First-Passage Phenomena and Their Applications*, World Scientific, 2013.
63 S. Condamin, V. Tejedor, R. Voituriez, O. Bénichou and J. Klafter, *Proc. Natl. Acad. Sci. U. S. A.*, 2008, **105**, 5675.
64 Y. Meroz, I. M. Sokolov and J. Klafter, *Phys. Rev. Lett.*, 2011, **107**, 260601.
65 A. M. Berezhkovskii, G. Hummer and S. M. Bezrukov, *Phys. Rev. Lett.*, 2006, **97**, 020601.
66 R. Satija, A. M. Berezhkovskii and D. E. Makarov, *Proc. Natl. Acad. Sci. U. S. A.*, 2020, **117**, 27116–27123.
67 A. M. Berezhkovskii and D. E. Makarov, *J. Phys. Chem. Lett.*, 2018, **9**, 2190–2195.
68 D. Hartich and A. Godec, *Phys. Rev. X*, 2021, **11**, 041047.
69 P. Reimann, C. Van den Broeck, H. Linke, P. Hänggi, J. M. Rubi and A. Pérez-Madrid, *Phys. Rev. Lett.*, 2001, **87**, 010602.
70 R. F. Capellmann, J. Bewerunge, F. Platten and S. U. Egelhaaf, *Rev. Sci. Instrum.*, 2017, **88**, 056102.
71 D. Blair and E. Dufresne, The Matlab Particle Tracking Code Repository, **https://site.physics.georgetown.edu/matlab/**, visited on 21/01/20.
72 X. Michalet, *Phys. Rev. E: Stat., Nonlinear, Soft Matter Phys.*, 2010, **82**, 041914.
73 C. W. Gardiner, *Handbook of Stochastic Methods for Physics, Chemistry, and the Natural Sciences*, Springer-Verlag, Berlin New York, 2nd edn, 1985.
74 H. Risken, *The Fokker–Planck Equation*, Springer, Berlin Heidelberg, 1989.
75 A. Chowdhury, F. Wood and B. J. Ackerson, *Opt. Commun.*, 1991, **86**, 547–554.
76 J. Bewerunge and S. U. Egelhaaf, *Phys. Rev. Accel. Beams*, 2016, **93**, 013806.
77 P. Hänggi, P. Talkner and M. Borkovec, *Rev. Mod. Phys.*, 1990, **62**, 251–341.
78 A. J. F. Siegert, *Phys. Rev.*, 1951, **81**, 617–623.
79 J. Keilson, *J. Appl. Probab.*, 1965, **2**, 405–428.
80 O. Bénichou, C. Chevalier, J. Klafter, B. Meyer and R. Voituriez, *Nat. Chem.*, 2010, **2**, 472.
81 A. Godec and R. Metzler, *Phys. Rev. X*, 2016, **6**, 041037.
82 A. Godec and D. E. Makarov, *J. Phys. Chem. Lett.*, 2023, **14**, 49–56.
83 J. M. Bello-Rivas and R. Elber, *J. Chem. Phys.*, 2015, **142**, 094102.
84 C. Schütte, F. Noé, J. Lu, M. Sarich and E. Vanden-Eijnden, *J. Chem. Phys.*, 2011, **134**, 204105.
85 D. Hartich and A. Godec, *Phys. Rev. Res.*, 2023, **5**, L032017.
86 K. Blom, K. Song, E. Vouga, A. Godec and D. E. Makarov, *Proc. Natl. Acad. Sci. U. S. A.*, 2024, **121**, e2318333121.
87 A. M. Berezhkovskii and D. E. Makarov, *J. Chem. Phys.*, 2019, **151**, 065102.
88 A. Ryabov, D. Lips and P. Maass, *J. Phys. Chem. C*, 2019, **123**, 5714–5720.

4.3 Colloidal transport in periodic potentials: the role of modulated-crowding

Journal: *Soft Matter*

Reference: Soft Matter, 2025,21, 3868

Impact factor: 2.9

Authors: Ramón Castañeda-Priego, Erick Sarmiento-Gómez, **Yasamin Mohebi Satalsari**, Stefan U. Egelhaaf and Manuel A. Escobedo-Sánchez

Author contributions:

MAES and SUE conducted the conceptualization and administration of the project. SUE provided the resources and acquired the funding. MAES, RCP, ESG and SUE worked on the investigation and validation, and MAES worked on the software. MAES and RCP worked on the computer simulations. ESG performed a preliminary analysis of the data. MAES, ESG, YMS worked on the methodology, data curation, visualization, and formal analysis. ESG wrote the original draft. RCP, ESG, YMS, and MAES, reviewed and edited the final version of the manuscript.

Soft Matter

PAPER

View Article Online
View Journal | View Issue

Cite this: *Soft Matter*, 2025, **21**, 3868

Colloidal transport in periodic potentials: the role of modulated-crowding†

Ramón Castañeda-Priego, ‡[a] Erick Sarmiento-Gómez, [ab] Yasamin Mohebi Satalsari, [b] Stefan U. Egelhaaf [b] and Manuel A. Escobedo-Sánchez ‡*[b]

Received 6th February 2025,
Accepted 4th April 2025

DOI: 10.1039/d5sm00133a

rsc.li/soft-matter-journal

The transport properties of colloids in external potentials are often studied at low concentrations to avoid particle–particle interactions. However, the impact of concentration on colloidal dynamics under external potentials has received limited attention. We examine the effect of concentration on the diffusivity of a quasi-2D colloidal dispersion subjected to a light-induced sinusoidal potential (interference fringes). By measuring particle diffusivity perpendicular to the fringes at various concentrations and laser powers, we find how the particle transport is governed by concentration and the structural organization induced by the external potential. Specifically, we introduce the concept of modulated-crowding for this physical scenario and characterize its influence on the long-time self-diffusion coefficient. These findings are confirmed using Brownian dynamics simulations.

1 Introduction

Soft materials, such as colloidal suspensions, are known to be susceptible to relatively weak external potentials,[1] that is, the potential has a magnitude around the thermal energy,[2] k_BT, with k_B and T being the Boltzmann constant and the absolute temperature, respectively. Understanding the material response to such potentials has been utilized to design tools that allow us to precisely control or manipulate the material constituents. Colloidal manipulation through different types of external potentials has attracted interest during the last two decades due to its potential technological applications.[3,4] Several simulation, theoretical, and experimental studies have found that one simple and effective way to control the properties of a colloidal suspension is to use geometric confinement.[4,5] Walls or boundaries act as external potentials that can modify the thermodynamic properties of the suspension. Furthermore, colloids between two parallel plates,[6] circular cavities,[7] parallel charge colloidal layers[8] and even one-dimensional colloidal systems[9–11] have been extensively investigated because structural and diffusive properties are strongly influenced by confinement.[4,6,12] Thus, confinement has become an important physical mechanism in many different areas of science and technology. Recent reviews highlighting the use and understanding of colloids under confinement can be found in ref. 1, 2, 4, 5 and 13, and references therein.

The confinement of a colloidal dispersion between walls can be treated as Brownian particles interacting with an arbitrarily large external potential placed in the position of the confining walls, effectively hindering the movement of the particles out of a given region.[4,14,15] Decreasing the energy barrier and adding some spatial variation to the external potential produces an energetic landscape that could induce, for example, freezing-like transitions.[6] Furthermore, a directional external field, *i.e.*, gravitational or electric, can produce sedimentation or electrophoretic mobility, leading to interesting non-equilibrium thermodynamic states or transport phenomena not typically seen under homogeneous conditions.[16–18] Moreover, a spatially inhomogeneous external field can also promote modifications in the phase behavior of the colloids, *e.g.*, laser-induced phase transitions.[6,19–21]

The optical force imposed on a dielectric particle by the refraction of light at the particle's interface, known as pressure radiation, is one of the experimental methods to create external potentials to interact with colloidal particles. This mechanism led to the development of optical tweezers.[22] It is a suitable option due to the flexibility to induce different spatially dependent light potentials.[3,5,13] Inspired by the pioneering work of Ashkin,[22] optical tweezers are now a widely used tool in physics and biology.[13] This type of light potential has been used to induce structural changes and explore both the influence of external potentials on the diffusion of individual colloidal

[a] *Departamento de Ingeniería Física, División de Ciencias e Ingenierías, Campus León, Universidad de Guanajuato, Loma del Bosque 103, Lomas del Campestre, 37150 León, Guanajuato, Mexico*
[b] *Condensed Matter Physics Laboratory, Heinrich Heine University, Düsseldorf, Universitätsstraße 1, 40225 Düsseldorf, Germany. E-mail: escobedo@hhu.de*
† This publication is in honor and remembrance of our friend, mentor, and colleague Stefan U. Egelhaaf.
‡ These authors contributed equally to this work.

particles[23,24] and the hydrodynamic correlations between a few-body colloidal system.[25–28] Currently, arbitrary light potentials are created by manipulating the wavefront of the incident laser using a spatial light modulator, even with a temporal evolution, thus opening the opportunity for spatio-temporal manipulating scenarios.[3,5]

Although the phase behavior of colloids under the influence of a periodic potential is currently well understood,[19–21,29–31] it is interesting to note that much less is known about the particle dynamics of colloidal suspensions under the action of modulated potentials. For example, the dependence of the particle transport of highly charged colloids on the strength of the sinusoidal potential was theoretically reported;[23] in that case, the area fraction was fixed ~ 0.153 and an interesting non-monotonic variation of particle diffusion emerged due to the competition between particle–particle and particle–potential interactions.[23] Moreover, the behaviour of weakly charged dilute colloidal suspensions under the influence of periodic potentials has been experimentally reported.[24] In the latter case, the authors focused on how the periodicity and laser power influenced the diffusive properties, specifically the amplitude of the modulated potential and the size of the particles. However, none of the previous contributions dealt with crowding effects. Nevertheless, recent studies have focused on understanding the physical phenomena that arise from the crowding of microparticles suspended in fluids subjected to periodic potentials, see, *e.g.*, ref. 32–40.

In this contribution, we report experimental findings that enhance the understanding of the dynamic behaviour of a confined colloidal dispersion influenced by a periodic energy landscape created by the interference patterns produced by the convergence of two laser beams. Varying the concentration of the sample from very dilute to moderate and adjusting the amplitude of the energetic landscape, we elucidate the impact of concentration on particle transport in periodic light potentials. The periodicity of the external potential was fixed and selected to be greater than the particle size. Specifically, attention has been focused on the effects of concentration (crowding) and amplitude of the modulated periodic potentials on diffusivity. The competition of both mechanisms allows us to introduce the concept of modulated-crowding for this physical scenario. We identify that modulated-crowding effects in the diffusion coefficient can be completely separated into distinct factors. Then, an appropriate external-potential-dependent normalization results in a universal dynamical behavior that is entirely described by the particle concentration and the structure induced by the external light field. This dynamical scenario is accurately described and corroborated by Brownian dynamics simulations.

2 Materials and methods

2.1 Brownian dynamics simulation and external potentials

In Brownian dynamics (BD) simulations, the configuration space of the N particle trajectories is composed of successive displacements $\vec{r}_i(t+\Delta\tau) - \vec{r}_i(t)$, $i = 1,\ldots,N$, generated from the following stochastic equation,[41]

$$\vec{r}_i(t+\Delta\tau) = \vec{r}_i(t) + \beta D_0 \vec{f}_i(t)\Delta\tau + \delta\vec{r}_i(\Delta\tau), \tag{1}$$

where $\beta = 1/k_BT$, and $\delta\vec{r}_i(\Delta\tau)$ a random displacement such that $\langle\delta\vec{r}_i(\Delta\tau)\rangle = 0$ and $\langle\delta\vec{r}_i(\Delta\tau)\delta\vec{r}_j(0)\rangle = 2D_0\delta_{ij}\Delta\tau$, with D_0 being the free-particle diffusion coefficient[26] and δ_{ij} the Kronecker delta. In eqn (1), $\vec{f}_i(t)$ represents the total external force acting on particle i, which includes the particle–particle and particle–potential interactions. The equation does not explicitly include hydrodynamic interactions. The particle–particle interaction is considered a hard-core potential, which is represented by the WCA potential,[42]

$$u_{\mathrm{WCA}}(r) = \begin{cases} A\varepsilon\left[\left(\frac{\sigma}{r}\right)^{\gamma} - \left(\frac{\sigma}{r}\right)^{\gamma-1}\right] + \varepsilon & r < \sigma B \\ 0 & r \geq \sigma B, \end{cases} \tag{2}$$

where

$$A = \gamma\left(\frac{\gamma}{\gamma-1}\right)^{\gamma-1}, B = \left(\frac{\gamma}{\gamma-1}\right). \tag{3}$$

with ε being the energy parameter, which is a measure of the repulsive strength between two colloidal particles. We have chosen $\gamma = 50$, and to reproduce the dynamics of hard disks, the reduced energy parameter is chosen to be $\varepsilon^* \equiv \varepsilon/k_BT = 0.6816$.[42] Using these potential parameters and without external modulation, we successfully reproduced the experimental long-time self-diffusion coefficients of quasi-two-dimensional colloidal hard spheres for area fractions ranging from 0.001 to 0.68, and consistent with previous studies conducted using dynamic Monte Carlo simulations of hard disks.[14] More specifically, in Appendix A we evaluate the precision of the hard-core potential model to replicate the particle dynamics across varying particle concentrations without the influence of an external field.

The particle–potential coupling is considered to be a periodic field, which can be regarded as a potential that generates energy barriers along the x-direction. Particles must overcome these barriers to move along this axis. This potential is mathematically described by[23,24]

$$u^{\mathrm{ext}}(x) = V_0 \cos\left(\frac{2\pi x}{\lambda}\right), \tag{4}$$

where V_0 is the potential amplitude and λ its periodicity. A comprehensive explanation of the connection between eqn (4) and the experimental conditions is introduced in Section 2.4.

The dynamics of the colloidal dispersion is then simulated as follows. We consider a random initial configuration of $N = 1024$ colloidal particles placed in a rectangular box of dimensions $L_x \times L_y$ with $L_y = \frac{\sqrt{3}}{2}L_x$. This condition is required in order to correctly reproduce the density fluctuations of a hard disk suspension.[43] Periodic boundary conditions are applied in each direction, with L_x and L_y being the sides of the simulation

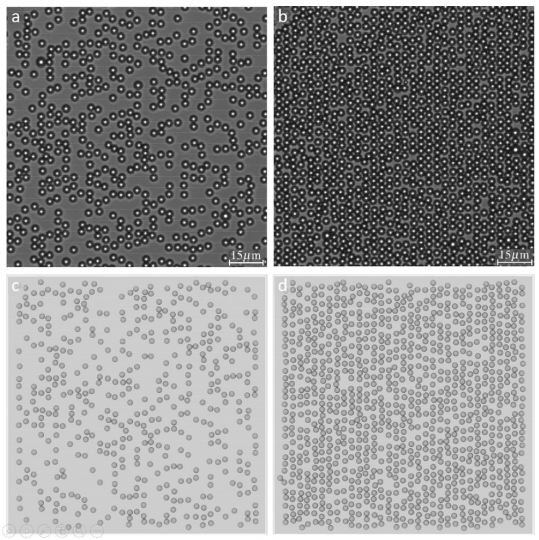

Fig. 1 Panels (a) and (b): regions of interest from experimental realizations of a colloidal suspension at area fractions η = 0.20 and η = 0.45, respectively, subjected to a light-induced sinusoidal potential (interference fringes) at a laser power of 3 W. The horizontal bar indicates a scale of 15 μm. Panels (c) and (d): snapshots of the simulated colloidal dispersion at η = 0.20 and η = 0.45, respectively, subjected to a periodic light field with amplitude $V_0 = 3.96 k_B T$. The box size and particle number in panel (c) (455 particles) were adjusted to match the box length of panel (d) (1024 particles) for enhanced visual comparison.

box along the x and y directions, respectively. We investigated particle concentrations that ranged from extremely low to moderate densities. The number of particles used in the simulations is large enough such that the results are independent of the system size; in most cases reported, every observable is the result of averaging over 5 independent realizations. Then, the particles move according to eqn (1), and the simulated colloidal system evolves from a non-equilibrium state to the equilibrium one.

The time step, $\Delta\tau$, in eqn (1) is chosen not to be too large to ensure that the force acting on the particle is approximately constant throughout its duration, but it must not be too small to ensure that we can use the description given by eqn (1), which is valid in the so-called diffusive regime. To do this, we have used a reduced time step of $\Delta\tau^\star \equiv \Delta\tau D_0/\sigma^2 = 1 \times 10^{-4}$, where σ is the diameter of the particles. The time window used in the BD simulations was set to $\Delta\tau^*_{\max} = 1 \times 10^2$. Fig. 1(c) and (d) shows representative snapshots of the Brownian dynamics computer simulations designed to replicate the experimental conditions.

2.2 Observables

The mean square displacement (MSD) is a key quantity used to characterize particle motion in systems ranging from simple liquids to soft materials and arrested states.[4] The MSD provides a detailed statistical picture of particle motion and bridges the gap between microscopic trajectories and macroscopic transport properties. The trajectories of particles within a periodic potential exhibit pronounced anisotropy. Under such conditions, particles diffuse mainly along the fringes (y-direction) because their movement across (x-direction) them is impeded by potential energy barriers.[5,23,31] In this contribution, we do not present data on the motion of particles parallel to the fringes since the external field does not influence particle displacement along this axis. Instead, our focus is on the particle movement perpendicular to the fringes. Hence, we determine the MSD in the x-direction, through a temporal average over all initial times t_0 and an ensemble average over all particle trajectories (denoted by E) represented by the following expression:

$$\langle \Delta x^2(\tau) \rangle = \langle [x(t_0 + \tau) - x(t_0)]^2 \rangle_{t_0,E}, \quad (5)$$

where $x(t)$ is the position in the x-direction of any particle at time t and τ is a delay time. Due to possible drift effects in the experiments, the contribution corresponding to the center-of-mass motion was removed from the MSD.

Two observables are derived from the MSD. First, the time-dependent diffusivity, $D(\tau)$, which describes how the rate of particle displacement evolves with time, capturing dynamic heterogeneity and complex interactions within the system. Second, the anomalous diffusion exponent, $\alpha(\tau)$, that shows the scaling of MSD with time, quantifying the transitions between normal, sub-, and super-diffusive behavior. Both quantities are obtained using the following expressions:

$$D(\tau) = \frac{1}{2}\frac{\mathrm{d}\langle \Delta x^2(\tau) \rangle}{\mathrm{d}\tau}, \quad (6)$$

$$\alpha(\tau) = \frac{\mathrm{d}\log\langle \Delta x^2(\tau) \rangle}{\mathrm{d}\log\tau}. \quad (7)$$

Therefore, the information obtained from the MSD, time-dependent diffusivity and the anomalous diffusion exponent provides a comprehensive framework for understanding particle transport,[44] including transitions between dynamical regimes and the effects of confinement, crowding, or external potentials in complex systems. Despite this, studying directed self-assembly at finite concentrations and its connection to colloid dynamics is far from trivial. This work focuses on unraveling how crowding affects particle transport in colloids subjected to different amplitudes of an external periodic potential, providing evidence that the structure arising from the interplay between crowding and the potential determines long-time diffusivity.

To quantify the structure arising from the interplay between crowding and the external potential, at least two different types of pair-correlation functions can be calculated:[23,45] (a) the pair correlation function along the y-direction, $g(y)$; it describes the spatial organization along any fringe, (b) the pair correlation function along the x-direction, $g(x)$; it provides information on the spatial correlation of particles in the direction perpendicular to the fringes.

2.3 Sample preparation, experimental setup and particle tracking

The colloidal suspensions were prepared using polystyrene sulfate latex particles with a radius of 1.48 μm and a polydispersity of ≤10% (Invitrogen Molecular Probes, Cat. No. S37222). The particles were suspended in ultra-pure water with a resistivity of 18.2 MΩ cm (Purelabs Flex, Elga). The suspensions were loaded into custom-made capillary cells of thickness ∼160 μm, and sealed with UV curing glue (Norland Optical Adhesive 61, Norland Products Inc.). Due to their size, the particles settled to the bottom of the sample cell, forming a monolayer and creating a quasi-two-dimensional (quasi-2D) colloidal system. The area fractions (η) studied in this work ranged from 0.015 to 0.45. All samples were allowed to equilibrate for one day prior to measurements. At moderate and higher concentrations, particle interactions occasionally led to vertical stacking, which caused the particles to leave the focal plane. However, this effect disappeared when the particles were subjected to the laser light potential, as the optical force pushed them against the bottom glass plate.

The experimental implementation of the periodic external potential is based on the interference of two coherent beams, as detailed in a previous study.[46] In summary, light coming from a laser source (Coherent Verdi V5, wavelength = 532 nm, beam diameter 2.25 mm) is expanded 3 times using a telescope and directed to a Köster's prism, providing two beams of almost equal intensity traveling parallel to the optical axis. These beams are focused onto the focal plane of an inverted microscope using a biconvex lens. The periodicity of the potential, determined by the crossing angle of the two beams and thus independent of the laser power, was set to λ = 3.8 μm. To determine the amplitude of the potential V_0 as a function of the laser power, the interaction between the particles and the potential must be characterized (see Section 2.4).

Bright-field images of colloidal suspensions were captured using an inverted microscope (Nikon, Ecplise Ti2-U) equipped with a 20× objective (Nikon, CFI Plan Fluor, NA 0.5) and a CMOS camera (Mako U-130, Allied Vision) with pixels of 4.8 × 4.8 μm^2. This leads to a pixel pitch of 0.24 μm per px. Images of 1024 × 1024 pixels were acquired at a frequency of 10 Hz. The field of view size was 246 × 246 μm^2. Fig. 1(a) and (b) shows representative regions of interest extracted from the experiments. The effective recording time for each concentration and the laser power was carefully limited to ensure that concentration fluctuations, caused by particles entering or leaving the field of view, remained below 10%. The recording durations ranged between 1200 s and 3600 s. To determine the position of the colloidal particles, a modified MATLAB-based particle tracking routines based on the ones from D. Blair and E. Dufresne[47] was implemented, which combined with the Michalet algorithm[48] led to a localization uncertainty of ±10 nm. The number of extracted trajectories ranged from ∼150 for an area fraction of 0.015 to ∼4000 for an area fraction of 0.45. The trajectories are openly available in Zenodo at **https://doi.org/10.5281/zenodo.14514294**.

2.4 Connection between laser power and potential amplitude

The external potential defined along the x-direction, $u^{\mathrm{ext}}(x)$, experienced by the particles is controlled by adjusting the laser power, LP. Its analytical expression is given by[13,21,49]

$$u^{\mathrm{ext}}(x) = g\alpha \mathrm{LP}\left(1 + 3\frac{j_1(qa)}{qa}\cos(qx)\right)\exp\left(-2x^2\cos^2(\theta/2)/R^2\right), \tag{8}$$

where g is a parameter dependent on the setup, $\alpha = a^3 n_S^2(n^2-1)/(n^2+2)$ is the polarizability of the particles (with a the radius of the particle, $n = n_C/n_S$ the ratio of the refractive indices of the colloid n_C and solvent n_S) and j_1 is the first-order spherical Bessel function. The Gaussian shape of the laser beams gives rise to the factor $\exp(-2x^2\cos^2(\theta/2)/R^2)$, with R being the radius of the beam and θ the cross angle and the wavevector $q = 2\pi/\lambda$. It is possible to define a simplified external potential as,[24]

$$u^{\mathrm{ext}}(x) = V_0\cos(qx) + V_{\mathrm{bg}}, \tag{9}$$

which is basically the one used in the BD simulations; see eqn (4) with amplitude $V_0 \propto$ LP and a potential offset V_{bg} that does not contribute to the force felt by the particle due to the external field (see eqn (1)).

To determine V_0 for a series of laser powers, we have used two dynamical approaches based on the long-time self-diffusion coefficient, D_L. As a first approach, we employed the one proposed by Festa *et al.*,[50] here referred to as Festa's approach, who solved the Smoluchowski equation for a Brownian-like particle in a periodic potential and obtained the following analytical expression,

$$\frac{D_L}{D_0} = \frac{1}{\langle\exp[u^{\mathrm{ext}}(x)/k_BT]\rangle\langle\exp[-\beta u^{\mathrm{ext}}(x)/k_BT]\rangle}, \tag{10}$$

where D_0 is the free diffusion coefficient, and $\langle\cdots\rangle$ denotes an average over a period of the external periodic potential. Then, by solving eqn (10), using eqn (4), one gets[50–53]

$$\frac{D_L}{D_0} = \frac{1}{[I_0(V_0/k_BT)]^2}. \tag{11}$$

where $I_0(x)$ is the modified Bessel function of the first kind. Note that in this context, V_{bg} has no effect on D_L. In the second approach, based on Kramers escape rate theory, Egelhaaf *et al.*[24] derived the following analytical expression for the long-time self-diffusion coefficient, D_L, of a colloid trapped in a sinusoidal potential,

$$\frac{D_L}{D_0} = \pi\left(\frac{2V_0}{k_BT}\right)\exp[-2V_0/k_BT]. \tag{12}$$

Within this approach, a Brownian particle has to overcome an energetic barrier of magnitude $2V_0/k_BT$ to escape from the potential well. Interestingly, eqn (12) can also be derived from eqn (11) considering that $I_0(x) \sim e^x/\sqrt{2\pi x}$ for $x \gg 1$.[54] Therefore, eqn (12), here referred to as Egelhaaf's approach, becomes the exact solution of the Smoluchowski equation for a Brownian-like particle diffusing in a sinusoidal potential in the limit of strong coupling, *i.e.*, $V_0 \gg k_BT$.

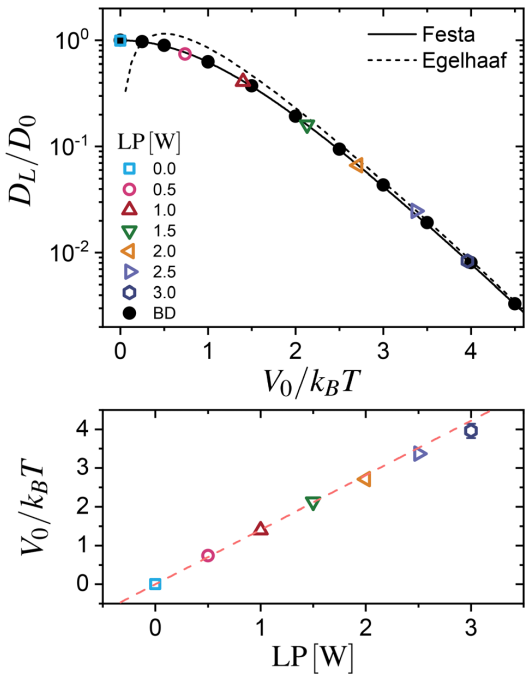

Fig. 2 Top panel: Long-time self-diffusion coefficient, D_L, of a single spherical colloid in a periodic potential as a function of V_0 for several laser powers, LP. Experiments (open symbols), Brownian dynamics simulations (black symbols), Festa's approach eqn (11) (solid line) and Egelhaaf's approach (12) (dashed line); experiments and BD simulations were performed at an area fraction of 0.015. Bottom panel: Dependence of the potential amplitude, V_0, on the laser power, LP. The dashed line was obtained by applying a simple linear regression that allowed us to establish the following relationship $V_0/\mathrm{LP} = (1.41 \pm 0.01)k_BT/\mathrm{W}$.

To validate the BD simulation scheme with an external field, we have calculated, for a given V_0, the normalized long-time self-diffusion coefficient (D_L/D_0), described by the limit $\tau \to \infty$ of eqn (5), represented as a continuous line in the top panel of Fig. 2. In the same figure, the results of the BD simulation (closed symbols) are shown. The excellent agreement found validates our simulation scheme. Additionally, in the top panel of Fig. 2, the dashed line displays the results from the Egelhaaf's approach (eqn (12)), which clearly performs well for external potential barriers of two times the thermal energy of the particles. Then, eqn (12) can be confidently used when $V_0 > 2k_BT$, that is, when $D_L < 0.2D_0$.

From the previous results, a clear connection emerges between the laser power and the amplitude of the potential experienced by the particles. This connection is mediated through D_L/D_0. In summary, determining D_L/D_0 and using Festa's or Egelhaaf's (with its respective limitations) approach, V_0 can be experimentally estimated for a given LP in a specific experimental configuration. In general, this relationship is instrument-dependent and varies with the experimental configuration; such dependence is accounted for by the term g in eqn (8).[24] The previous description represents the calibration protocol that we have used for our setup.

Finally, the open symbols in the top panel of Fig. 2 correspond to the experimental results for an area fraction of η = 0.015 used as calibration for the periodic light field. The calibration was performed for six different laser powers. These results show excellent agreement with the theoretical predictions from eqn (11) and (12). The explicit dependence of V_0 on LP is presented in the bottom panel of Fig. 2. Applying a simple linear regression, we have obtained the following relationship between LP and V_0: $V_0/\mathrm{LP} = (1.41 \pm 0.01)k_BT/\mathrm{W}$.

It is important to note that in the experiments, D_0 is not the bulk diffusion coefficient, as it includes hydrodynamic effects due to particle–wall interactions,[14,55] which could be factorized by replacing D_0 with the short-time self-diffusion coefficient D_s.[15] To simplify the notation and facilitate a direct comparison between the experimental results and the BD simulations, we used the short-time diffusion coefficient D_s instead of D_0 from the calibration experiments. This point will be discussed in more detail in Section 3.2. The good agreement between experiments, simulations, and theory allows us not only to highlight the equivalence between the BD simulations and the analytical solution provided by the Smoluchowski equation, but also to make evident that in the dilute limit, the diffusivity is basically driven by the external modulation.

2.5 Mean squared displacement, time-dependent diffusivity and anomalous diffusion exponent: experiments *vs.* Brownian dynamics simulations

The particle trajectories of a colloidal suspension, with an area fraction of η = 0.015, were analyzed across the fringes (x-direction) to extract the mean squared displacement (MSD, eqn (5)), the time-dependent diffusivity ($D(\tau)$, eqn (6)), and the anomalous diffusion exponent ($\alpha(\tau)$, eqn (7)). The experimental data was acquired for several values of the laser power, LP, and BD simulations were performed for V_0 values calculated with the Festa approach for each LP. In Fig. 3, results from experiments (symbol) and BD simulations (lines) are summarized, showing a very good agreement.

As expected for these experiments, the MSD (Fig. 3, top panel) exhibits diffusive behavior at short and long times that depends on LP. In general, at short-time scales, the MSDs increase linearly with time, reflecting the Brownian motion of the particles in the fringes, before the influence of the potential becomes significant. At intermediate-time scales, the MSDs deviate from linearity as particles interact with the barriers formed by the potential, showing sub-diffusive behavior. Finally, at long-time scales, when the particles can overcome the potential barriers (due to thermal fluctuations), the MSD exhibits again a linear dependence on time but with a reduced effective diffusion coefficient. These coefficients are related to the local slope of the MSD, which can be easily quantified through $D(\tau)$. In the middle panel of Fig. 3, the values of $D(\tau)$ normalized by D_0 are explicitly shown. The reduction in the long-time diffusion coefficient is a clear indication of the effect of the particle jumping between fringes.

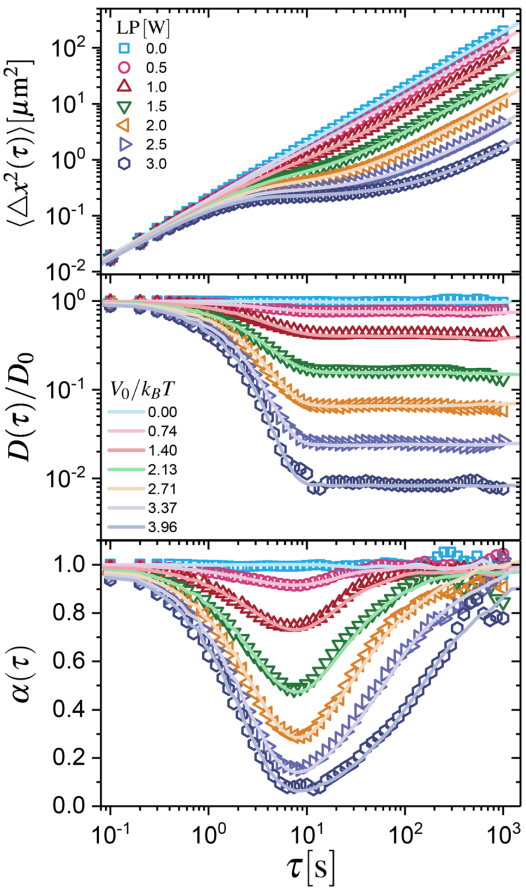

Fig. 3 Top panel: Mean-square displacement, $\langle \Delta x^2(\tau) \rangle$, middle panel: time-dependent diffusivity, $D(\tau)$, and bottom panel: anomalous diffusion exponent, $\alpha(\tau)$, of a colloidal dispersion with an area fraction of η = 0.015 and several values of the laser power, LP, or external potential amplitude, V_0, as indicated. Symbols denote experiments and solid lines Brownian dynamics simulations.

Furthermore, these time-dependent behaviors are related to the time dependence of the MSD, quantified through $\alpha(\tau)$. The results of the analysis of $\alpha(\tau)$ are shown in Fig. 3 (bottom panel), where the full dynamical transition from short-time to long-time diffusion ($\alpha(\tau)$ = 1) can be observed. Similarly, as before, for intermediate times the dynamics of the particles is subdiffusive, *i.e.* $\alpha(\tau) < 1$. The observed downward shift in short-time is partially due (particle–wall effects are discussed in Section 3.2) to the increasing restriction in the movement of the particles in the potential minimum, which becomes more attractive with LP. It should be emphasized that although it is widely accepted that when $\alpha(\tau) = 1$ a long-time diffusion coefficient can be obtained, the diffusivity analysis reveals a flattening behaviour for $D(\tau)$ where $\alpha(\tau) < 1$ without any significant change for more of an order of magnitude in τ. This ensures that simulations and experiments were conducted under comparable temporal conditions.

3 Particle dynamics: coupling with the external field and concentration effects

Understanding particle dynamics in complex systems, such as crowding in periodic potentials, requires a multifaceted analytical approach. The combined analysis of dynamic and static observables provides valuable insights into particle transport phenomena, revealing how particles navigate through different dynamic regimes.

3.1 Pair-correlation-like functions, $g(x)$ and $g(y)$

As stated above, in this contribution, we investigate the effects of crowding on particle dynamics in a quasi-2D colloidal system subjected to a modulated potential. To explicitly characterize modulated-crowding effects, it is essential to understand how the external potential may affect the spatial organization of particles and, consequently, their transport properties. To achieve this, we investigate the arrangement of particles along the *x*- and *y*-axis (with respect to the laboratory frame of reference) at various laser powers. We define pair-correlation-like functions, $g(x)$ and $g(y)$, to analyze spatial particle correlations in directions perpendicular and parallel to the optical fringes, respectively. The pair correlation-like function $g(y)$ was determined for the particles in each potential minima and averaged over all fringes, providing information on the spatial organization of particles within potential wells.

Analyzing $g(x)$ and $g(y)$ reveals how particle density fluctuations affect the spatial particle arrangement within the potential landscape. For illustrative purposes, in Fig. 4 and 5, $g(x)$ and $g(y)$, respectively, are shown for LP = 2.5 W and area fractions ranging from 0.015 (dilute) up to 0.45 (intermediate). Our findings reveal that spatial correlations in the direction perpendicular to the fringes (Fig. 4) make it evident that the particles are, on average, pinned to the fringes. Additionally, one can see that the characteristic distance of the particles in the *x*-direction is determined by the periodicity of the light field (long-dash arrow) and not by the size of the particles σ (short-dash arrow). This is because the periodicity is larger than the diameter of the particles, $\lambda > \sigma$. To facilitate comparison between different area fractions, we have normalized $g(x)$ by

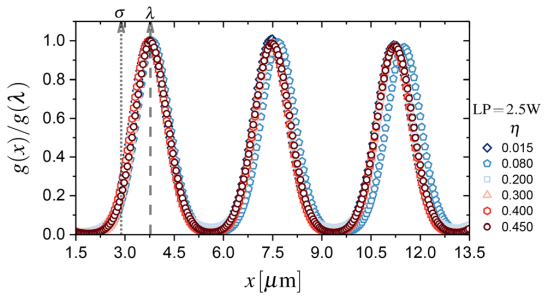

Fig. 4 Pair-correlation-like function, $g(x)$, for a laser power LP = 2.5 W and several values of the area fraction, η, as displayed. Arrows indicate the values at $x = \sigma$ and $x = \lambda$.

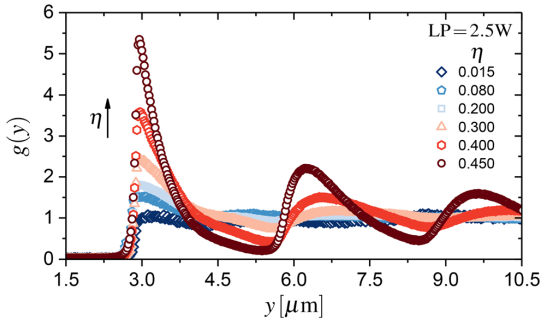

Fig. 5 Pair-correlation-like function, $g(y)$, for a laser power LP = 2.5 W and several values of the area fraction, η, as displayed. Arrow indicates the increase in the particle concentration.

$g(x = \lambda)$. The same phenomenology is also observed for the other laser powers and area fractions (data not shown).

In the direction parallel to the fringes, $g(y)$ illustrates the effect of a structured system; see Fig. 5, which presents density correlation peaks that grow in magnitude with increasing concentration and extend over long ranges, as indicated by the arrow. In particular, the contact value, $g(y = \sigma)$, becomes more pronounced at higher area fractions. A summary of the contact values, $g(y = \sigma)$, for all laser powers and area fractions is presented in Fig. 6. As seen, $g(y = \sigma)$ shows a systematic increase with η for all laser powers, revealing the structural evolution of the particles under the effect of the external potential. At low area fractions ($\eta < 0.2$), $g(y = \sigma)$ shows minimal variation between different laser powers, suggesting that direct particle–particle interactions primarily govern particle correlations. However, as η increases beyond 0.2, we observe a marked differentiation in $g(y = \sigma)$ values across different laser powers. Higher powers (LP $\geq$ 1.5 W) lead to significantly higher contact values, indicating strong spatial correlations and local ordering induced by the combination of particle crowding and the external periodic potential.

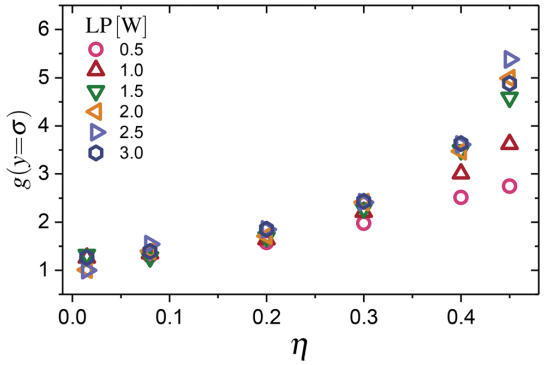

Fig. 6 Contact values, $g(y = \sigma)$, as a function of the area fraction, η, for all laser powers, LP, as indicated.

The nonlinear growth of $g(y = \sigma)$ with increasing η, especially seen at higher laser powers, suggests a combined effect between the external field and particle concentration in promoting local structure formation, fundamentally altering the system's spatial organization compared to the unperturbed case (LP = 0.0 W). In other words, $g(y = \sigma)$ contains both effects that we define here as modulated-crowding, which will be essential to establish a connection between the spatial organization and the particle dynamics, as we discussed further below.

3.2 Long-time self-diffusion coefficient and modulated-crowding effects

The normalized long-time self-diffusion coefficient, D_L/D_0, is directly obtained from the normalized time-dependent self-diffusivity, $D(\tau)/D_0$, for $\tau > 20$ s. As shown in Fig. 7, all functions reach a plateau for $\tau > 20$ s, indicating that the long-time regime has been achieved. In Fig. 7, we present $D(\tau)/D_0$ for laser powers ranging from 0 W to 3 W and three area fractions: 0.08, 0.30, and 0.45, corresponding to panels (a), (b), and (c), respectively. Importantly, BD simulations (solid lines) quantitatively capture the experimental data (symbols). However, minor discrepancies are always present, leading to

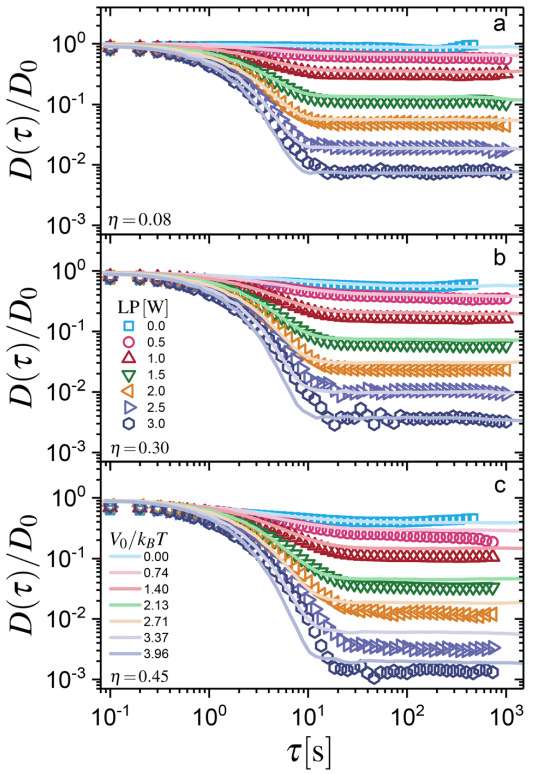

Fig. 7 Time-dependent self-diffusivity, $D(\tau)$, for different laser powers or external field amplitudes, as indicated, and an area fraction of (a) η = 0.08, (b) η = 0.3 and (c) η = 0.45. Symbols represent experiments and solid lines Brownian dynamics simulations.

reasonable deviations between experiments and BD simulations. Possible sources of these small discrepancies include: (1) in the simulations, we employ a model pair potential – a short-range repulsive and continuous potential – which, in principle, reproduces the thermodynamic properties of hard disks.[42] (2) Simulations do not include hydrodynamic interactions, which mainly influence and reduce the short-time self-diffusion coefficient. However, their effects can be effectively factorized and disentangled from particle–particle contributions at long times; see ref. 14 and 55. Despite these minor approximations, the agreement between experiments and BD simulations remains noteworthy.

$D(\tau)$ shows the expected and previously reported dynamical behaviour, which can be explained as follows: for short times, the particle moves freely, sampling short distances around a potential minimum with a short-time diffusion coefficient D_s. This is found to be 35% lower than the bulk value (D_0) due to the hydrodynamic interaction of the particle with the wall.[15] In the dilute case, the short-time diffusion coefficient shows slight variations with laser power. An increase in laser power results in a more pronounced force effect on the particles, pushing them closer to the wall and slowing their dynamics due to the wall–particle hydrodynamic interactions. Therefore, to factor in these effects and establish a connection with the BD simulations,[55] D_0 is considered to be D_s for each corresponding LP in $\eta = 0.015$, with the same values used for the dilute case applied to higher concentrations. For higher concentrations, D_s also includes contributions from particle–particle interactions. At intermediate times, the particles become localized due to their interaction with the laser field. This localization resembles the well-known caging effect, where $D(\tau)$ decays faster as the laser power increases. However, at long times, normal diffusion is recovered, *i.e.*, $D(\tau)$ reaches a plateau, but with a self-diffusion coefficient, D_L, smaller than D_0 (*i.e.*, $D_L < D_0$), which clearly depends on both laser power and particle concentration. Interestingly, the time at which the particles reach the plateau—transitioning from localization to delocalization—is essentially the same in all cases, with $\tau_{trans} \sim 20$ s (see also Fig. 3). This regime is related to particle hopping across minima, as discussed in other works,[23,24,31] resembling a random walk and thus leading to a diffusive regime once again.

The long-time self-diffusivity behavior reveals a complex interplay between laser power (LP) and area fraction (η). Our analysis of $D(\tau)/D_0$ at long-time demonstrates that increasing the laser power from 0.0 W to 3.0 W systematically reduces the long-time diffusion coefficient, with the most dramatic effects observed at higher area fractions. At $\eta = 0.45$, the normalized long-time diffusivity decreases by three orders of magnitude when exposed to the maximum laser power (3.0 W), indicating strong particle localization within the periodic potential wells. This effect is less pronounced at lower area fractions ($\eta = 0.08$), where reduced particle–particle interactions allow greater mobility even under strong field conditions. The relationship between laser power and long-time diffusivity follows a nonlinear trend, with a critical threshold around 1.5 W where significant mobility reduction begins to manifest. Notably, the area fraction acts as a mobility-limiting factor, enhancing the confinement effect of the laser-induced potential landscape. This combined interaction between laser power and area fraction suggests that particle crowding amplifies the effectiveness of the external field in restricting long-time particle diffusion, providing a tunable mechanism for controlling colloidal dynamics in confined geometries.

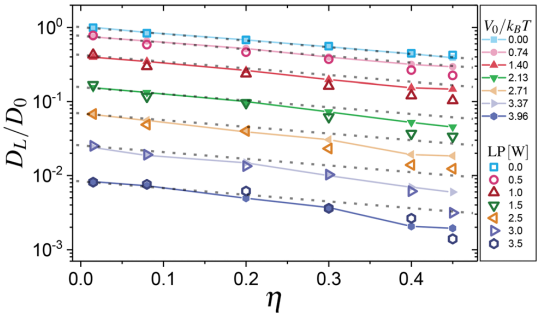

Fig. 8 Long-time self-diffusion coefficient, D_L/D_0 as a function of the area fraction, η, obtained from experiments (open symbols) and Brownian dynamics simulations (closed symbols with solid lines) for several values of the laser power, LP, or external potential amplitude, V_0, as indicated. The dotted lines are parallel to the particle–potential-free case (LP = 0.0 W).

To quantify the effect of both particle–particle and particle–field interactions on particle transport, we extracted the ratio D_L/D_0 for all laser powers. In Fig. 8 we summarized the experimental results (open symbols) for D_L/D_0 as a function of area fraction (η) for several laser powers (LP) of the applied periodic potentials. BD simulations for the corresponding amplitude of the potential are shown as closed symbols with solid lines. Again, BD simulations demonstrate excellent agreement with experimental results. The data reveal two key physical mechanisms: first, a systematic decrease in particle mobility with increasing area fraction for all laser powers, evidencing the role of crowding effects; second, a marked reduction in diffusion as the laser power increases from 0 to 3.5 W (corresponding to V_0/k_BT from 0 to 3.96), demonstrating the enhanced confinement of particles within the optical potential wells.

Notably, at the highest laser power (LP = 3.5 W), the diffusion coefficient drops by two orders of magnitude compared to the particle–potential-free case (LP = 0.0 W), while the impact of crowding becomes more pronounced as evidenced by the steeper decline in D_L/D_0 with increasing η.

The variation in the data trend is now discussed. As seen in Fig. 9, D_L/D_0 exhibits a notable deviation from the reference case (particle–potential-free, LP = 0.0 W) as both the area fraction (η) and the laser power increase. This behavior is evidenced by the deviation of the experimental data and the BD simulation results, which are parallel to the particle–potential-free case. It reveals a nontrivial coupling between particle concentration and the periodic potential landscape. At low laser powers ($\leq$1.0 W), the system maintains a trend similar to the particle–potential-free case, where crowding effects dominate the reduction of the particle mobility. However, as the laser power increases ($>$1.5 W), we observe a pronounced deviation

from this trend, particularly at higher area fractions ($\eta > 0.3$), where the diffusion coefficient drops more steeply than predicted by simple crowding effects. Furthermore, these variations appear to be similar across all cases, indicating a consistent trend regardless of the specific conditions, much like the behavior of the contact value of $g(y)$ (Fig. 6). This enhanced reduction in particle mobility suggests a combined, synergistic effect between particle–particle (entropy-driven) and particle–potential (energy-driven) interactions, where crowding amplifies the localizing effect of the periodic potential. Brownian dynamics simulations corroborate these experimental findings, accurately capturing the transition from a crowding-dominated regime to one where the interplay between spatial confinement and particle interactions results in a more dramatic dropping of the long-time diffusion. This behavior indicates that the presence of neighboring particles enhances the trapping efficiency of the potential wells, resulting in a nonlinear response to increasing area fraction that becomes more pronounced at higher potential amplitudes.

The results presented in Fig. 8 reveal a remarkable finding in the behavior of the long-time self-diffusion coefficient of colloidal particles confined in a quasi-2D geometry under the combined influence of many-body interactions (crowding) and an external modulated potential; a physical scenario that we refer to as "modulated-crowding." To analyze the concentration effects in this context, we introduce the normalized long-time self-diffusion coefficient, $D_L/D_L^{V_0}$, where $D_L^{V_0}$ represents the long-time diffusion coefficient of a dilute suspension under the influence of the modulated potential (eqn (11)). This quantity is presented as a function of the area fraction, η, for different amplitudes of the periodic potential, V_0, and is mathematically expressed as:

$$\frac{D_L}{D_L^{V_0}} = \frac{D_L^{\eta}}{D_0}, \tag{13}$$

This kind of factorization has been useful for separating or estimating the effects of the direct interactions, *i.e.*, particle–particle interactions, from the indirect ones, *i.e.*, hydrodynamic interactions (see ref. 14, 15 and 55–57).

In Fig. 9, the ratio $D_L/D_L^{V_0}$ as a function of the area fraction for all the considered laser powers (open symbols) is displayed. In this representation, the deviation of the data from the LP = 0.0 W case (blue open squares), discussed in the previous section, is evident. As mentioned above, this deviation results from the competition between particle–particle and particle–potential interactions, which *a priori* cannot be considered decoupled. However, this competition must, in some way, be related to the structure, which should incorporate concentration effects and a contribution from the periodic potential. The latter disrupts the homogeneity of the material distribution, as we have quantified and demonstrated in Section 3.1.

Interestingly, we found that an excellent approximation for quantifying the effects of local structure on diffusivity is the one proposed by Brady,[57] which provides a simple relationship between the long-time self-diffusion coefficient, D_L, the

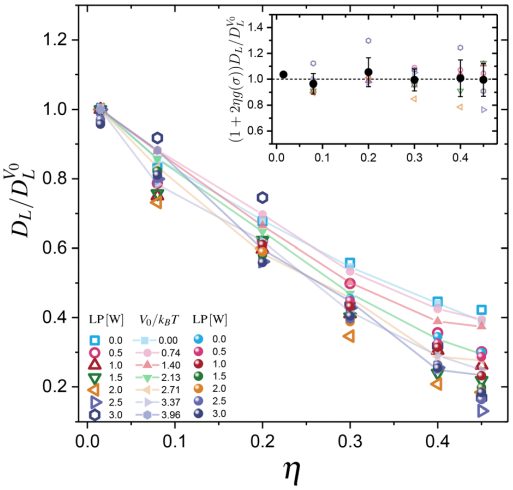

Fig. 9 Ratio $D_L/D_L^{V_0}$ as a function of the area fraction for all the considered laser powers, as indicated. Open symbols are the results from the experiments, closed symbols are the results from Brownian dynamics simulations, and spheres are determined using eqn (14). Inset shows the product $\frac{D_L}{D_L^{V_0}}(1+2\eta g(\sigma)) \sim 1$ as a function of the particle concentration for $V_0 \neq 0$.

short-time self-diffusion coefficient, D_0, the local structure, $g(y)$, and the concentration, η. It has the following mathematical form:

$$\frac{D_L^{\eta}}{D_0} = (1+2\eta g(\sigma))^{-1}, \tag{14}$$

where $g(\sigma)$ is the contact value of $g(y)$. Again, it is important to emphasize that $g(y)$ incorporates both the effects of concentration, η, and the periodic field (see Fig. 5 and 6), which means that $g(\sigma)$ quantifies the mechanism defined as modulated-crowding. Thus, as we will see later, the factor $2\eta g(\sigma)$ carries the physical information of both crowding effects and the periodic field.

We then determined D_L^{η}/D_0 for all measurements using eqn (14). The results (spheres) are plotted in Fig. 9. Surprisingly, despite the quasi-2D nature of the colloidal system, eqn (14) reproduces the experimental data (open symbols) with remarkable accuracy, which was originally derived for three-dimensional systems. This agreement is particularly significant given that the colloidal system is strongly confined and subject to a periodic external potential. Our physical interpretation of this unexpected behavior is that by imposing spatially periodic energy barriers, the laser potential effectively restricts the configuration space accessible to the particles. This constraint reduces the effective dimensionality of the transport problem by preferentially confining the particles within the potential minima. It is important to note that when the measurements of D_L for $V_0 = 0.00k_BT$ are compared directly with those using eqn (14), do not quantitatively reproduce

the experimental data. This aspect was previously noted and reported by Thorneywork *et al.*[14]

The inset of Fig. 9 highlights the fact that in the presence of a sinusoidal potential, the product $\frac{D_L}{D_L^{V_0}}(1+2\eta g(\sigma)) \sim 1$ for all particle concentrations confirms our description. The black closed symbols correspond to the average of all LP values for the same area fraction, with an error bar representing the standard deviation, indicating variations of less than 10 percent. These observations have important implications for understanding and controlling particle dynamics in confined systems, confirming that the imposition of periodic external potentials can be used as a tool to systematically modify transport properties in quasi-2D colloidal dispersions.

By replacing eqn (14) in eqn (13), the expression becomes,

$$\frac{D_L}{D_L^{V_0}} = [1+2\eta g(\sigma)]^{-1}. \quad (15)$$

The preceding equation accurately describes the diffusivity in the direction perpendicular to the fringes of a colloidal dispersion subjected to a periodic field, allowing us to identify the underlying physical mechanism, called modulated crowding. However, it remains important to clarify the limits of applicability of eqn (15). To address it and motivated by the strong agreement between Brownian dynamics (BD) simulations and experimental data, we conducted an extensive analysis using BD simulations (see Appendix B). Our analysis confirms that eqn (15) quantitatively describes particle dynamics up to an area fraction of approximately $\eta \sim 0.50$. Furthermore, a closer examination of certain limiting cases (also discussed in Appendix B) reveals that at low concentrations (up to $\eta \sim 0.20$), eqn (15) reduces to: $\frac{D_L}{D_L^{V_0}} \sim 1-2\eta$, indicating that, in this dilute regime, diffusivity is essentially determined by the modulation introduced by the periodic potential, as described by eqn (11).

4 Concluding remarks and perspectives

In this work, we have provided experimental and theoretical evidence on the role of crowding in the diffusivity of confined colloids subjected to a light-induced sinusoidal potential with fixed periodicity and variable amplitude. We have also reported and explicitly discussed the dynamical properties along the perpendicular direction of the fringes as a function of the particle concentration and laser power, having introduced the concept of modulated-crowding for this physical scenario.

In particular, we focused on the long-time particle dynamics. Our results indicate that, after an appropriate renormalization, the long-time self-diffusion coefficient, crowding effects on particle transport can be fully explained in terms of two main contributions: particle concentration and the structural correlations imposed by the external modulation. This finding highlights that the effects of modulated-crowding on the long-time self-diffusion coefficient of colloids interacting *via* short-range repulsive forces can be entirely disentangled from the contributions of the external field. A particularly significant aspect of our findings is that, due to particle trapping induced by the periodic potential at any concentration, the Brady relation, originally developed for three-dimensional systems and particularly effective in concentrated regimes, accurately reproduced the experimental results even in low-concentration conditions. This suggests that the underlying dynamics in the presence of modulated-crowding closely resemble those of highly concentrated three-dimensional systems, offering a new perspective on the role of spatial structuring in the diffusion of confined colloidal systems.

Last but not least, we should stress that exploring other types of external potentials, *i.e.* periodic with other symmetries or nonperiodic potentials, will allow us to better understand the relationship between the static properties and the transport of colloids in well-controlled heterogeneous environments.

Author contributions

MAES and SUE conducted the conceptualization and administration of the project. SUE provided the resources and acquired the funding. MAES, RCP, ESG and SUE worked on the investigation and validation, and MAES worked on the software. MAES and RCP worked on the computer simulations. ESG performed a preliminary analysis of the data. MAES, ESG, YMS worked on the methodology, data curation, visualization, and formal analysis. ESG wrote the original draft. RCP, ESG, YMS, and MAES, reviewed and edited the final version of the manuscript.

Data availability

Data for this article, including all particle trajectories analyzed in the manuscript, are available at Zenodo URL: **https://doi.org/10.5281/zenodo.14514294**.

Conflicts of interest

There are no conflicts to declare.

Appendices

A Appendix: comparison between dynamic Monte Carlo and Brownian dynamics simulation schemes

To assess the validity of the hard-core potential (eqn (2)),[42] we have chosen $\gamma = 50$, and $\varepsilon^* \equiv \varepsilon/k_BT = 0.6816$ to reproduce the dynamics of hard disks. The Brownian Dynamics simulations were performed as described in Section 2.1. In Fig. 10, we compare the normalized long-time self-diffusion coefficients of quasi-two-dimensional colloidal hard spheres for area fractions ranging from 0.001 up to 0.68 with previous studies conducted using dynamic Monte Carlo simulations of hard disks.[14] The long-time diffusion coefficient was determined following the procedure described in Section 3.2 of the main text. As seen in Fig. 10, excellent agreement between both methods is obtained.

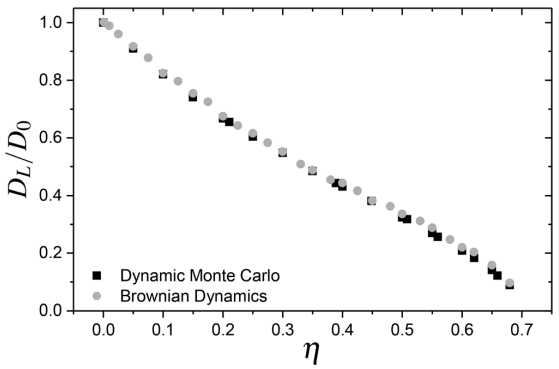

Fig. 10 Comparison of the normalized long-time self-diffusion coefficients for area fractions ranging from 0.001 up to 0.68 for Brownian dynamics simulations based on the hard-core potential and dynamic Monte Carlo simulations of hard disks.[14]

B Analysis of the modulated-crowding approach: testing the limits of Brady's diffusivity formula

As discussed in Section 3, eqn (15) quantitatively describes the long-time diffusion behaviour (along the perpendicular direction of the fringes) of colloids subjected to a light-induced sinusoidal potential up to an area fraction of $\eta \sim 0.5$. To gain a deeper understanding of the physical mechanisms driving this transport behaviour, one should analyze certain intriguing limiting cases of the eqn (15).

Let us consider the case where $2\eta g(\sigma) \ll 1$. In that limit, eqn (15) simply reduces to,

$$\frac{D_{\mathrm{L}}}{D_{\mathrm{L}}^{V_0}} \sim 1 - 2\eta g(\sigma), \tag{16}$$

which results from neglecting all terms of the order $\mathcal{O}(\eta 2)$ and higher. In that limit, η is very low, so $g(\sigma)$ is expected to be close to unity because it does not depend strongly on either η nor V_0. Hence, eqn (15) reduces to $D_{\mathrm{L}}/D_{\mathrm{L}}^{V_0} \sim 1 - 2\eta$. By explicitly comparing with Brownian dynamics simulations, we conclude that the previous equation is a good estimate up to $\eta < 0.2$ and $V_0 < 4k_{\mathrm{B}}T$. This means that particle dynamics is given at low concentrations by modulation of the periodic potential, eqn (11), as expected.

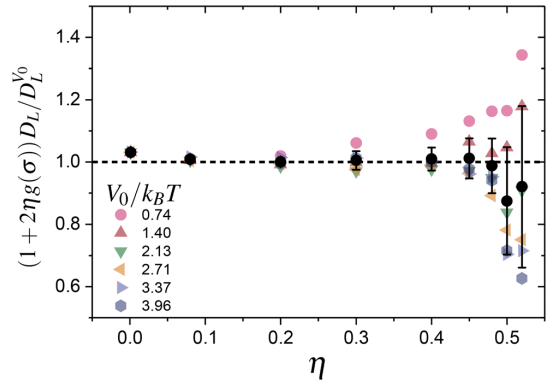

Fig. 11 Assessment of the validity of eqn (15) tested by Brownian dynamics simulations. For area fractions (η) exceeding 0.50, deviations from eqn (15) become apparent, indicating its breakdown. Different symbols correspond to different potential barrier heights ($V_0/k_{\mathrm{B}}T$), as indicated.

By means of Brownian dynamics simulations (under the same conditions as previously written), we investigated the limits of validity of eqn (15). Fig. 11 clearly illustrates that for area fractions exceeding 0.50, eqn (15) ceases to be valid. This threshold area fraction ensures sufficient spacing between the fringes, allowing the particles to jump from one fringe to another.

Acknowledgements

Authors thank CONAHCYT-Mexico (Grants No. A1-S-9098, Ciencia de Frontera 102986, CBF2023-2024-3350) and the Deutsche Forschungsgemeinschaft (DFG) – Project number 459399860 for financial support. R. C. P. also acknowledges financial support provided by the Alexander von Humboldt Foundation. MAES and YMS appreciate valuable comments and discussions from Dr Angel B. Zuccolotto-Bernez.

Notes and references

1 H. Löwen, *J. Phys.: Condens. Matter*, 2008, **20**, 404201.
2 R. Castañeda-Priego, *Rev. Mex. Fis.*, 2021, **67**, 050101.
3 D. Grier, *Nature*, 2003, **424**, 810–816.
4 C. O. Solano-Cabrera, P. Castro-Villarreal, R. E. Moctezuma, F. Donado, J. Conrad and R. Castañeda-Priego, *Annu. Rev. Condens. Matter Phys.*, 2025, **16**, 41–59.
5 F. Evers, R. D. L. Hanes, C. Zunke, R. F. Capellmann, J. Bewerunge, C. Dalle-Ferrier, M. C. Jenkins, I. Ladadwa, A. Heuer, R. Castañeda Priego and S. U. Egelhaaf, *Eur. Phys. J.-Spec. Top.*, 2013, **222**, 2995.
6 H. Löwen, *J. Phys.: Condens. Matter*, 2009, **21**, 474203.
7 K. Mangold, J. Birk, P. Leiderer and C. Bechinger, *Phys. Chem. Chem. Phys.*, 2004, **6**, 1623–1626.
8 C. Contreras-Aburto, J. Mendez-Alcaraz and R. Castañeda-Priego, *J. Chem. Phys.*, 2010, **132**, 174111.
9 S. Herrera Velarde, A. Zamudio-Ojeda and R. Castaneda-Priego, *J. Chem. Phys.*, 2010, **133**, 114902.
10 A. Taloni, O. Flomenbom, R. Castañeda-Priego and F. Marchesoni, *Soft Matter*, 2017, **13**, 1096–1106.
11 A. Villada-Balbuena, A. Ortiz-Ambriz, P. Castro-Villarreal, P. Tierno, R. Castañeda Priego and J. M. Méndez-Alcaraz, *Phys. Rev. Res.*, 2021, **3**, 033246.
12 U. Gasser, *J. Phys.: Condens. Matter*, 2009, **21**, 203101.
13 M. C. Jenkins and S. U. Egelhaaf, *J. Phys.: Condens. Matter*, 2008, **20**, 404220.
14 A. L. Thorneywork, R. E. Rozas, R. P. A. Dullens and J. Horbach, *Phys. Rev. Lett.*, 2015, **115**, 268301.

15 E. Sarmiento-Gómez, J. R. Villanueva-Valencia, S. Herrera-Velarde, J. A. Ruiz-Santoyo, J. Santana-Solano, J. L. Arauz-Lara and R. Castañeda Priego, *Phys. Rev. E*, 2016, **94**, 012608.
16 J. A. S. Gallegos, J. Martínez-Rivera, N. E. Valadez-Pérez and R. Castañeda-Priego, *J. Chem. Phys.*, 2023, **158**, 114907.
17 V. Lobaskin, B. Dünweg, M. Medebach, T. Palberg and C. Holm, *Phys. Rev. Lett.*, 2007, **98**, 176105.
18 J. M. Kim, J. Fang, A. P. R. Eberle, R. Castañeda Priego and N. J. Wagner, *Phys. Rev. Lett.*, 2013, **110**, 208302.
19 A. Chowdhury, B. J. Ackerson and N. A. Clark, *Phys. Rev. Lett.*, 1985, **55**, 833–836.
20 Q.-H. Wei, C. Bechinger, D. Rudhardt and P. Leiderer, *Phys. Rev. Lett.*, 1998, **81**, 2606–2609.
21 C. Bechinger, Q. H. Wei and P. Leiderer, *J. Phys.: Condens. Matter*, 2000, **12**, A425–A430.
22 A. Ashkin, *Phys. Rev. Lett.*, 1970, **24**, 156–159.
23 S. Herrera-Velarde and R. Castañeda Priego, *Phys. Rev. E:Stat., Nonlinear, Soft Matter Phys.*, 2009, **79**, 041407.
24 C. Dalle-Ferrier, M. Krüger, R. D. L. Hanes, S. Walta, M. C. Jenkins and S. U. Egelhaaf, *Soft Matter*, 2011, **7**, 2064–2075.
25 C. Lutz, M. Reichert, H. Stark and C. Bechinger, *Europhys. Lett.*, 2006, **74**, 719.
26 S. Herrera-Velarde, E. C. Euan-Díaz, F. Córdoba-Valdés and R. Castañeda-Priego, *J. Phys.: Condens. Matter*, 2013, **25**, 325102.
27 E. Cereceda-López, D. Lips, A. Ortiz-Ambriz, A. Ryabov, P. Maass and P. Tierno, *Phys. Rev. Lett.*, 2021, **127**, 214501.
28 D. Lips, E. Cereceda-López, A. Ortiz-Ambriz, P. Tierno, A. Ryabov and P. Maass, *Soft Matter*, 2022, **18**, 8983–8994.
29 S. Bleil, H. H. von Grünberg, J. Dobnikar, R. Castañeda-Priego and C. Bechinger, *Europhys. Lett.*, 2005, **73**, 450.
30 R. F. Capellmann, A. Khisameeva, F. Platten and S. U. Egelhaaf, *J. Chem. Phys.*, 2018, **148**, 114903.
31 D. Pérez-Guerrero, J. L. Arauz-Lara, E. Sarmiento-Gómez and G. I. Guerrero-García, *Front. Phys.*, 2021, **9**, 635269.
32 D. Lips, A. Ryabov and P. Maass, *Phys. Rev. Lett.*, 2018, **121**, 160601.
33 D. Lips, A. Ryabov and P. Maass, *Phys. Rev. E*, 2019, **100**, 052121.
34 D. Lips, R. L. Stoop, P. Maass and P. Tierno, *Commun. Phys.*, 2021, **4**, 224.
35 A. Ryabov, D. Lips and P. Maass, *J. Phys. Chem. C*, 2019, **123**, 5714–5720.
36 A. P. Antonov, A. Ryabov and P. Maass, *J. Chem. Phys.*, 2021, **155**, 184102.
37 A. P. Antonov, A. Ryabov and P. Maass, *Phys. Rev. Lett.*, 2022, **129**, 080601.
38 A. P. Antonov, D. Voráč, A. Ryabov and P. Maass, *New J. Phys.*, 2022, **24**, 093020.
39 E. Cereceda-Lopez, A. P. Antonov, A. Ryabov, P. Maass and P. Tierno, *Nat. Commun.*, 2023, **14**, 6448.
40 D. Voráč, P. Maass and A. Ryabov, *J. Chem. Phys.*, 2023, **159**, 114114.
41 D. L. Ermak and J. A. McCammon, *J. Chem. Phys.*, 1978, **69**, 1352.
42 C. A. Báez, A. Torres-Carbajal, R. Castañeda-Priego, A. Villada-Balbuena, J. M. Méndez-Alcaraz and S. Herrera-Velarde, *J. Chem. Phys.*, 2018, **149**, 164907.
43 B. Li, Y. Nishikawa, P. Höllmer, L. Carillo, A. C. Maggs and W. Krauth, *J. Chem. Phys.*, 2022, **157**, 234111.
44 R. Metzler, J.-H. Jeon, A. G. Cherstvy and E. Barkai, *Phys. Chem. Chem. Phys.*, 2014, **16**, 24128–24164.
45 S. Herrera-Velarde and R. Castañeda Priego, *Phys. Rev. E:Stat., Nonlinear, Soft Matter Phys.*, 2008, **77**, 041407.
46 R. F. Capellmann, J. Bewerunge, F. Platten and S. U. Egelhaaf, *Rev. Sci. Instrum.*, 2017, **88**(5), 056102.
47 D. Blair and E. Dufresne, *The Matlab Particle Tracking Code Repository*, **https://site.physics.georgetown.edu/matlab/**, visited on 21/01/20.
48 X. Michalet, *Phys. Rev. E:Stat., Nonlinear, Soft Matter Phys.*, 2010, **82**, 041914.
49 K. Loudiyi and B. J. Ackerson, *Phys. A*, 1992, **184**, 1–25.
50 R. Festa and E. d'Agliano, *Phys. A*, 1978, **90**, 229–244.
51 P. Reimann, C. Van den Broeck, H. Linke, P. Hänggi, J. M. Rubi and A. Pérez-Madrid, *Phys. Rev. E:Stat., Nonlinear, Soft Matter Phys.*, 2002, **65**, 031104.
52 J. Spiechowicz, I. G. Marchenko, P. Hänggi and J. Łuczka, *Entropy*, 2023, **25**, e25010042.
53 A. V. Straube and F. Höfling, *J. Phys. A: Math. Theor.*, 2024, **57**, 295003.
54 B. Geelen, *Adv. Eng. Software*, 1995, **23**, 105–109.
55 J. R. Villanueva-Valencia, J. Santana-Solano, E. Sarmiento-Gómez, S. Herrera-Velarde, J. L. Arauz-Lara and R. Castañeda Priego, *Phys. Rev. E*, 2018, **98**, 062605.
56 M. Medina-Noyola, *Phys. Rev. Lett.*, 1988, **60**, 2705–2708.
57 J. F. Brady, *J. Fluid Mech.*, 1994, **272**, 109–134.

Chapter 5

Conclusions

In this thesis, we have explored the dynamics of colloidal particles subjected to spatially periodic light fields by combining precise experiments, theoretical modeling, and numerical simulations. In our experimental system, particles were confined in 2D geometries and subjected to well controlled cosine optical potentials generated by laser interference patterns.

As part of this work, the periodic light field was calibrated to enable systematic studies of particle dynamics in periodic light fields. For calibration, we employed four independent approaches. First, direct imaging of the fringe pattern provides the periodicity of the potential from the intensity profile of the fringes. Second, analysis of the Boltzmann equilibrium distribution yields both the periodicity and the amplitude from the particle probability density in equilibrium. Third, long-time diffusion analysis following the Festa and Egelhaaf approaches determines the amplitude from the normalized long-time diffusion coefficient. Finally, the ISF-based calibration represents a novel approach, offering an additional method to extract the potential amplitude from equilibrium correlation properties in the long-time regime.

We systematically studied how the potential amplitude V_0 depends on the geometric ratio σ/L, where σ is the particle diameter and L is the periodicity of the optical potential. We observed that V_0 is not determined only by the laser intensity but is also influenced by this ratio, reflecting how the relative size of the particles to the spatial period affects the effective amplitude of the potential. Variations in σ/L therefore lead to measurable differences in the effective amplitude at the same laser power.

Furthermore, we studied the dynamics of particles driven at external velocities using a nanopositioning stage. By varying the stage velocity, we tuned the Péclet number (Pe) and thereby controlled the balance between driven transport and periodic potential. At low Pe, the particle motion is strongly modulated by the periodic potential, with clear signs of localization near potential minima, while at

high Pe, the potential's influence diminishes and enhanced transport dominates.

Overall, this work establishes a consistent and quantitative framework for studying colloidal dynamics in periodic optical potentials. It provides robust experimental calibration protocols, clarifies the interplay between geometry and effective potential amplitude, and examines how external driving influences the particle motion in the presence of the light field.

The following section presents three collaborative publications that constitute the core of this work.

Intermediate scattering function of colloids in a periodic laser field [9]

In this study, we applied the generalized intermediate scattering function (ISF) to investigate colloidal dynamics in periodic optical potentials. The generalized ISF, obtained from experimental trajectories, captures the full dynamical behavior of the particles. We determined the mean squared displacement (MSD), time-dependent diffusivity $D(\tau)$, and non-Gaussian parameter (NGP) from experimental data and compared them with theoretical results from a perturbative expansion of the generalized ISF, finding consistent agreement. Together, these results establish the generalized ISF as a sensitive and reliable framework for probing particle dynamics in periodic optical potentials.

Precisely controlled colloids: a playground for path-wise non-equilibrium physics [10]

In this work, both equilibrium and driven experiments with colloidal particles were performed, providing trajectory data with sufficient resolution to access path-wise observables such as first-passage and transition-path times. These experimental results, together with theoretical analysis, confirmed key predictions of stochastic thermodynamics by demonstrating how nonequilibrium driving modifies trajectory statistics.

Colloidal transport in periodic potentials: the role of modulated-crowding [11]

In this study, we investigated how increasing the concentration of particles and varying the amplitude of the optical potential influence the colloidal dynamics. We showed that these two factors jointly modify the long-time diffusivity, as both interparticle interactions and external potential play a role in determining the transport behavior of the particles. In addition, we studied our system within the framework of the Brady relation. Our results show that the Brady relation provides an accurate description of the quasi-two-dimensional system, remaining valid even at low concentrations, where trapping by the optical potential becomes relevant.

Bibliography

[1] M. Doi, *Soft matter physics*. oxford university press, 2013.

[2] H. Kawamoto, "The history of liquid-crystal displays," *Proceedings of the IEEE*, vol. 90, no. 4, pp. 460–500, 2002.

[3] W. C. Poon and D. Andelman, *Soft condensed matter physics in molecular and cell biology*. CRC Press, 2006.

[4] R. Castañeda-Priego, "Colloidal soft matter physics," *Revista Mexicana de Física*, vol. 67, p. 050101, 2021.

[5] W. Poon, P. Pusey, and H. Lekkerkerker, "Colloids in suspense," *Physics World*, vol. 9, p. 27, apr 1996.

[6] M. D. Haw, "Colloidal suspensions, brownian motion, molecular reality: a short history," *Journal of physics: condensed matter*, vol. 14, no. 33, p. 7769, 2002.

[7] C. Bechinger, M. Brunner, and P. Leiderer, "Phase behavior of two-dimensional colloidal systems in the presence of periodic light fields," *Physical review letters*, vol. 86, no. 5, p. 930, 2001.

[8] R. Capellmann, J. Bewerunge, F. Platten, and S. Egelhaaf, "Note: using a kösters prism to create a fringe pattern," *Review of Scientific Instruments*, vol. 88, no. 5, 2017.

[9] R. Rusch, Y. Mohebi Satalsari, A. B. Zuccolotto-Bernez, M. A. Escobedo-Sánchez, and T. Franosch, "Intermediate scattering function of colloids in a periodic laser field," *Soft Matter*, vol. 21, pp. 4908–4924, 2025.

[10] C. Dieball, Y. M. Satalsari, A. B. Zuccolotto-Bernez, S. U. Egelhaaf, M. A. Escobedo-Sánchez, and A. Godec, "Precisely controlled colloids: a playground for path-wise non-equilibrium physics," *Soft Matter*, vol. 21, no. 11, pp. 2170–2181, 2025.

[11] R. Castañeda-Priego, E. Sarmiento-Gómez, Y. M. Satalsari, S. U. Egelhaaf, and M. A. Escobedo-Sánchez, "Colloidal transport in periodic potentials: the role of modulated-crowding," *Soft Matter*, vol. 21, pp. 3868–3879, 2025.

[12] A. Yethiraj and A. van Blaaderen, "A colloidal model system with an interaction tunable from hard sphere to soft and dipolar," *nature*, vol. 421, no. 6922, pp. 513–517, 2003.

[13] C. A. Murray and D. G. Grier, "Video microscopy of monodisperse colloidal systems," *Annual Review of Physical Chemistry*, vol. 47, no. 1, pp. 421–462, 1996.

[14] P. N. Pusey and W. Van Megen, "Phase behaviour of concentrated suspensions of nearly hard colloidal spheres," *Nature*, vol. 320, no. 6060, pp. 340–342, 1986.

[15] D. G. Grier, "A revolution in optical manipulation," *nature*, vol. 424, no. 6950, pp. 810–816, 2003.

[16] M. Pelton, K. Ladavac, and D. G. Grier, "Transport and fractionation in periodic potential-energy landscapes," *Phys. Rev. E*, vol. 70, p. 031108, Sep 2004.

[17] M. C. Jenkins and S. U. Egelhaaf, "Colloidal suspensions in modulated light fields," *Journal of Physics: Condensed Matter*, vol. 20, no. 40, p. 404220, 2008.

[18] R. Capellmann, A. Khisameeva, F. Platten, and S. Egelhaaf, "Dense colloidal mixtures in an external sinusoidal potential," *The Journal of Chemical Physics*, vol. 148, no. 11, 2018.

[19] J. K. Dhont, *An introduction to dynamics of colloids*. Elsevier, 1996.

[20] C. A. Báez, A. Torres-Carbajal, R. Castañeda-Priego, A. Villada-Balbuena, J. M. Méndez-Alcaraz, and S. Herrera-Velarde, "Using the second virial coefficient as physical criterion to map the hard-sphere potential onto a continuous potential," *The Journal of Chemical Physics*, vol. 149, no. 16, p. 164907, 2018.

[21] K. Loudiyi and B. J. Ackerson, "Direct observation of laser induced freezing," *Physica A: Statistical Mechanics and its Applications*, vol. 184, no. 1-2, pp. 1–25, 1992.

[22] R. Brown, "Microscopical observations on the particles contained in the pollen of plants," *Edinburgh New Philosophical Journal*, vol. 5, pp. 358–371, 1828.

[23] A. Einstein, "Über die von der molekularkinetischen theorie der wärme geforderte bewegung von in ruhenden flüssigkeiten suspendierten teilchen," *Annalen der Physik*, vol. 322, pp. 549–560, 1905.

[24] J. Perrin, "Mouvement brownien et réalité moléculaire," 1909.

[25] D. S. Lemons and A. Gythiel, "Paul Langevin's 1908 paper "On the Theory of Brownian Motion" ["Sur la théorie du mouvement brownien," C. R. Acad. Sci. (Paris) 146, 530-533 (1908)]," *American Journal of Physics*, vol. 65, no. 11, pp. 1079–1081, 1997.

[26] M. von Smoluchowski, "Zur kinetischen theorie der brownschen molekularbewegung und der suspensionen," *Annalen der Physik*, vol. 326, no. 14, pp. 756–780, 1906.

[27] J. Crank, *The Mathematics of Diffusion*. Clarendon Press, 1979.

[28] H. C. Berg, *Random Walks in Biology: New and Expanded Edition*. rev - revised ed., 1993.

[29] W. Sutherland, "Lxxv. a dynamical theory of diffusion for non-electrolytes and the molecular mass of albumin," *The London, Edinburgh, and Dublin Philosophical Magazine and Journal of Science*, vol. 9, no. 54, pp. 781–785, 1905.

[30] X. Bian, C. Kim, and G. E. Karniadakis, "111 years of brownian motion," *Soft Matter*, vol. 12, pp. 6331–6346, 2016.

[31] A. Goldman, R. G. Cox, and H. Brenner, "Slow viscous motion of a sphere parallel to a plane wall—ii couette flow," *Chemical engineering science*, vol. 22, no. 4, pp. 653–660, 1967.

[32] P. Huang, J. S. Guasto, and K. S. Breuer, "Direct measurement of slip velocities using three-dimensional total internal reflection velocimetry," *Journal of fluid mechanics*, vol. 566, pp. 447–464, 2006.

[33] B. Lin, J. Yu, and S. A. Rice, "Direct measurements of constrained brownian motion of an isolated sphere between two walls," *Phys. Rev. E*, vol. 62, pp. 3909–3919, Sep 2000.

[34] R. Metzler, J.-H. Jeon, A. G. Cherstvy, and E. Barkai, "Anomalous diffusion models and their properties: non-stationarity, non-ergodicity, and ageing at the centenary of single particle tracking," *Phys. Chem. Chem. Phys.*, vol. 16, pp. 24128–24164, 2014.

[35] A. Rahman, "Correlations in the motion of atoms in liquid argon," *Phys. Rev.*, vol. 136, pp. A405–A411, Oct 1964.

[36] M. E. Sanchez, *Digital Fourier Microscopy and its Application to Soft Matter Systems*. PhD thesis, Universitäts-und Landesbibliothek der Heinrich-Heine-Universität Düsseldorf, 2023.

[37] M. P. Allen and D. J. Tildesley, *Computer simulation of liquids*. Oxford university press, 2017.

[38] H. Risken and H. Risken, *Fokker-planck equation*. Springer, 1996.

[39] N. G. Van Kampen, *Stochastic processes in physics and chemistry*, vol. 1. Elsevier, 1992.

[40] P. W. Atkins, J. De Paula, and J. Keeler, *Atkins' physical chemistry*. Oxford university press, 2023.

[41] C. Dalle-Ferrier, M. Krüger, R. D. L. Hanes, S. Walta, M. C. Jenkins, and S. U. Egelhaaf, "Dynamics of dilute colloidal suspensions in modulated potentials," *Soft Matter*, vol. 7, pp. 2064–2075, 2011.

[42] R. Festa and E. d'Agliano, "Diffusion coefficient for a brownian particle in a periodic field of force: I. large friction limit," *Physica A: Statistical Mechanics and its Applications*, vol. 90, no. 2, pp. 229–244, 1978.